Title

Seawater strontium responses to short-timescale carbon cycle changes

Permalink

https://escholarship.org/uc/item/1b27g388

Author

Wood, Madison M

Publication Date

2024

UNIVERSITY OF CALIFORNIA

SANTA CRUZ

SEAWATER STRONTIUM RESPONSES TO SHORT-TIMESCALE CARBON CYCLE CHANGES

A dissertation submitted in partial satisfaction of the

requirements for the degree of

DOCTOR OF PHILOSOPHY

in

EARTH SCIENCES

by

Madison M. Wood

September 2024

The Dissertation of Madison M. Wood
is approved:

Professor Adina Paytan, Chair

Professor Mathis Hain

Professor James Zachos

Peter Biehl
Vice Provost and Dean of Graduate Studies

Table of Contents

List of Figures

List of Tables

Abstract

Seawater strontium responses to short-timescale carbon cycle changes

by

Madison M. Wood

The stable isotope composition of strontium dissolved in the ocean offers a new and relatively unexplored tracer of carbon cycle processes fundamental to the regulation of Earth's climate system. Seawater stable strontium isotope ratios ($\delta^{88/86}$Sr) vary over million-year timescales in response to changes in continental weathering and the marine carbonate sink. Reconstructing $\delta^{88/86}$Sr variations through time consequently provides insight to long-term carbon cycle processes and, most critically, their positive or negative feedbacks on climate. The canonical view of conservative elements in the ocean suggests that seawater $\delta^{88/86}$Sr should not respond to shorter-term carbon cycle changes, but mounting evidence suggests that the ocean Sr budget may have been imbalanced over the glacial/interglacial cycles of the Pleistocene. This dissertation addresses the outstanding question of whether the ocean Sr budget was sensitive to perturbation by changing carbonate burial and weathering fluxes on relatively short timescales during major climate transitions.

In Chapter 2, I reviewed our current quantitative understanding of carbonate burial in the ocean over the past 2.5 million years and concluded that the shallow carbonate sink, past and present, remains vastly underconstrained. My review introduced $\delta^{88/86}$Sr as a potential proxy for past changes in carbonate burial during the Quaternary ices ages if the isotope ratio is shown to be sensitive to carbonate fluxes on these timescales. In Chapters 3 and 4 I investigated two different archives of paleo seawater chemistry – pore fluids preserved in a Maldives carbonate platform and marine barite accumulated in deep sea sediments – to determine whether seawater $\delta^{88/86}$Sr varied over glacial/interglacial cycles. Both archives revealed measurable fluctuations in seawater $\delta^{88/86}$Sr over the past 250 kyr. These observations were combined with model simulations to explore the potential links between glacial/interglacial sea level, marine carbonate burial and weathering, and Sr cycling. Finally, I looked at another period of glaciation in Earth

history, the Eocene/Oligocene Transition, in Chapter 5 and found that seawater $\delta^{88/86}$Sr was not sensitive to the major carbon cycle perturbation during this time. Together, these chapters provide the first geochemical records of seawater $\delta^{88/86}$Sr during abrupt climate events and inform our evolving understanding of how carbon cycle changes have impacted elements in seawater.

Acknowledgments

I am immensely grateful to my advisor, Adina Paytan, who is my staunch advocate and dedicated mentor. Adina, thank you for shaping my growth as scientist, educator, and human in such a meaningful way.

Many thanks to my committee members Mathis Hain, for helping me think through unanticipated research findings, sharing his carbon cycle enthusiasm, and fostering a positive learning community for the biogeochemistry grads; and Jim Zachos, for thoughtfully engaging with my research and teaching me about climates before the Quaternary.

This research would not have been possible without the support of Toni Eisenhauer and Ana Kolevica, who hosted me at GEOMAR and allowed me to analyze samples in their lab. Special thanks to Ana for her kindness and patient training on the TIMS.

Countless individuals have supported me throughout this endeavor. I want to express my thanks to everyone who has been part of my graduate experience, especially:

To the labmates, collaborators, and colleagues who have provided scientific input, lab assistance, mentorship, and moral support – Paytan Lab members (past and present), my fellow biogeochemistry grads, Tamara Pico, Sam Kodama, Lucas Ognibene, Clara Blättler, Heather Houlton, Michael Tatzel, and Brian Dreyer;

To the (geo)chemists who mentored me, inspired me, and let me learn in their laboratories as an undergraduate – Andy Jacobson, Julie Bryce, Ruth Varner, Rose Came, Angela Gallego-Sala, and Nan Yi. Without their encouragement I wouldn't be in an Earth Science PhD program;

To my friends, from California to Vermont, for inexpressibly enriching life;

To my trail running community, for encouraging me in big scary goals;

To my family, for wholeheartedly supporting me in my pursuits;

And most of all, to Ben, for everything.

Contributions to this work: Adina Paytan and Mathis Hain supervised the research that forms the basis for this dissertation. The text of this dissertation includes a reprint of the following previously published material:

> Wood, M., Hayes, C.T., Paytan, A. 2023. Global Quaternary Carbonate Burial: Proxy- and Model-Based Reconstructions and Persisting Uncertainties. *Annual Review of Marine Science 15:1*, 277-302.

This published work includes a contribution from Christopher T. Hayes, who compiled the deep-sea carbonate flux data presented in Chapter 2.5.2.

Anton Eisenhauer and Ana Kolevica provided analytical support for Chapters 3–5. Clara Blättler supplied the pore fluid and sediments samples analyzed in Chapter 3 and assisted with interpretations and manuscript preparation. Tamara Pico and Sam Kodama performed the GIA modeling for the relative sea level reconstructions used in Chapter 4. Tamara Pico also advised the development of the continental shelf model presented in Chapter 4. Lucas Ognibene assisted with sample preparation and laboratory analyses for Chapter 4.

Chapter 1

Introduction

Geochemical records of elements and isotopes in seawater inform our understanding of carbon cycle processes in the past and the links between the ocean and climate. Strontium (Sr) is a conservative and uniformly distributed element in seawater, sourced from continental rocks and submarine hydrothermal systems and incorporated into calcium carbonate due to chemical affinities very similar to those of calcium (Broecker & Peng, 1982; Veizer, 1989). Radiogenic Sr isotope ratios ($^{87}\mathrm{Sr}/^{86}\mathrm{Sr}$) have long served as a tracer of continental weathering processes and hydrothermal activity (McArthur et al., 2012; Veizer, 1989). More recently, the non-traditional stable Sr isotope ratio ($\delta^{88/86}\mathrm{Sr}$) has been shown to vary through time due to changes in the shallow marine carbonate sink (Paytan et al., 2021). When paired with complementary records of the traditional $^{87}\mathrm{Sr}/^{86}\mathrm{Sr}$ ratios and deep-sea carbonate burial, seawater $\delta^{88/86}\mathrm{Sr}$ reconstructions can potentially constrain the full global carbonate budget (Paytan et al., 2021). This new proxy for shallow carbonate burial is exciting in light of the persisting challenges associated with quantifying carbonate accumulation in shallow marine environments in the modern ocean and, especially, back in time.

Paleoceanographic reconstructions of seawater $\delta^{88/86}\mathrm{Sr}$ (Paytan et al., 2021; Vollstädt et al., 2014; Wang et al., 2023) have to date focused secular variations due to changes in climate and tectonics on million-year timescales because the residence time of Sr in the ocean is long, about two million years. The prevailing view of conservative elements in seawater is that the concentration and isotopic composition will not change significantly on timescales shorter than the residence time (Broecker & Peng, 1982). However, there has been growing recognition that the ocean Sr budget may have been dynamic on short timescales, particularly during glacial/interglacial cycles in the Quaternary (Krabbenhöft et al., 2010; Mokadem et al., 2015; Paytan et al., 2021; Pearce et al., 2015; Stoll & Schrag, 1998; Stoll et al., 1999; Vance et al., 2009). A combination of two mechanisms has been proposed to explain the apparent disequilibrium of Sr in the modern ocean: non-steady-state variations in continental weathering due to glacial processes (Mokadem et al., 2015; Vance et al., 2009) and changes in net carbonate burial in the shallow ocean due to sea level fluctuations (Berger, 1982; Krabbenhöft et al., 2010; Opdyke & Walker, 1992; Stoll & Schrag, 1998). While the weathering flux is constrained by ^{87}Sr/^{86}Sr records (Mokadem et al., 2015; Vance et al., 2009), the accumulation of shallow marine carbonate remains vastly underconstrained (Iglesias-Rodriguez et al., 2002; Milliman & Droxler, 1996; Milliman, 1993; O'Mara & Dunne, 2019). I hypothesized that seawater $\delta^{88/86}$Sr varied on timescales shorter than a million years in response to abrupt changes in the shallow carbonate sink, thereby offering quantitative constraints on shallow carbonate burial and the feedbacks between sea level, atmospheric CO_2, and climate.

The overarching aim of this dissertation is to establish whether seawater $\delta^{88/86}$Sr varied over short timescales (less than one million years).

I begin by introducing the importance of quantifying rates of marine carbonate burial through geologic time, focusing on the Quaternary when sea level fluctuations likely impacted the global carbonate budget and atmospheric CO_2 (Berger, 1982; Opdyke & Walker, 1992) (**Chapter 2**). I demonstrate that the our quantitative grasp of glacial/interglacial carbonate burial remains limited and propose $\delta^{88/86}$Sr as a new proxy for Quaternary shallow carbonate burial.

My first study uses a unique archive of glacial seawater preserved in carbonate platform pore fluids in the Maldives Inner Sea to test whether seawater $\delta^{88/86}$Sr was different during the Last Glacial Maximum compared to today (**Chapter 3**). My analyses of pore fluid $\delta^{88/86}$Sr reveal that glacial seawater Sr concentrations and $\delta^{88/86}$Sr were respectively higher and lower than modern values. This is also the first study to investigate the effect of early marine diagenesis on pore fluid and carbonate $\delta^{88/86}$Sr in a shallow marine environment.

Chapter 4 builds on the findings of the previous chapter to document variations in seawater $\delta^{88/86}$Sr over full glacial/interglacial cycles. Using marine barite in deep sea sediment cores I establish a 250-kyr record of seawater $\delta^{88/86}$Sr, which shows significant variability independent of changes in ^{87}Sr/^{86}Sr and weathering. I interpret these $\delta^{88/86}$Sr variations in the context of glacial/interglacial sea level change and coral reef development.

Finally, I delve deeper in time to a major climate transition similar to the Quaternary glacial/interglacial cycles; the Eocene-Oligocene Transition serves as another test of whether seawater $\delta^{88/86}$Sr responded to short-term carbon cycle perturbation (**Chapter 5**). Contrary to my hypothesis, I find that the ocean Sr budget maintained steady state during the Eocene-Oligocene Transition, suggesting that seawater $\delta^{88/86}$Sr only became a useful proxy of shallow carbonate burial changes over the Late Cenozoic.

This body of work advances our understanding of the short-term evolution of seawater chemistry and the links between climate, sea level, and the cycling of elements in the ocean. The geochemical records presented in this dissertation are the first to document seawater $\delta^{88/86}$Sr on sub-million year timescales and can be used in combination with other proxy records and biogeochemical models to constrain key Earth system processes.

Chapter 2

Global Quaternary carbonate burial: proxy- and model-based reconstructions and persisting uncertainties

This chapter is a reproduction of an article published in *Annual Review of Marine Science*: Wood, M., Hayes, C.T., Paytan, A. 2023. Global Quaternary Carbonate Burial: Proxy- and Model-Based Reconstructions and Persisting Uncertainties. *Annual Review of Marine Science* 15:1, 277-302. Supplemental data can be accessed at doi.org/10.1146/annurev-marine-031122-031137.

2.1 Abstract

Constraining rates of marine carbonate burial through geologic time is critical for interpreting reconstructed changes in ocean chemistry and understanding feedbacks and interactions between Earth's carbon cycle and climate. The Quaternary Period (the past 2.6 million years) is of particular interest due to dramatic variations in sea level that periodically exposed and flooded areas of carbonate accumulation on the continental shelf, likely impacting the global carbonate budget and atmospheric carbon dioxide.

These important effects remain poorly quantified. Here, we summarize the importance of carbonate burial in the ocean–climate system, review methods for quantifying carbonate burial across depositional environments, discuss advances in reconstructing Quaternary carbonate burial over the past three decades, and identify gaps and challenges in reconciling the existing records. Emerging paleoceanographic proxies such as the stable strontium and calcium isotope systems, as well as innovative modeling approaches, are highlighted as new opportunities to produce continuous records of global carbonate burial.

2.2 Introduction

Marine carbonate burial is an important component of the global carbon cycle, with large quantities of carbonate stored in ocean sediments (∼5 × 103 Gt C) and the lithosphere (∼7 × 107 Gt C) (Zeebe, 2012). The carbonate flux influences atmospheric and oceanic inventories of carbon on 1,000- to 100,000-year timescales, playing a potentially important role in glacial/interglacial climate transitions during the Quaternary Period (the past 2.6 My) (Zeebe, 2012). Indeed, carbonate deposition has often been invoked to explain changes in Quaternary ocean chemistry and atmospheric carbon dioxide (CO_2) concentrations (Berger, 1982; Brovkin et al., 2007; Kerr et al., 2017; Kohfeld & Ridgwell, 2009; Opdyke & Walker, 1992; Rickaby et al., 2010; Ridgwell et al., 2003; Vecsei & Berger, 2004; Walker & Opdyke, 1995). However, robust quantitative constraints on global Quaternary carbonate burial remain elusive.

The last comprehensive review of carbonate production and accumulation over the past ∼20 ky (Milliman, 1993) provided flux estimates across neritic environments (coral reefs, banks, bays, and continental shelves) and pelagic environments (slopes, enclosed basins, and the deep sea above the carbonate compensation depth (CCD)) (Table 2.1). Many of these estimates had uncertainties of ≥100% (Iglesias-Rodriguez et al., 2002; Milliman & Droxler, 1996) due to the scarcity of deep-sea (pelagic) records and lack of knowledge about carbonate accumulation and preservation in shallow (neritic) marine settings. These gaps motivated further study of Quaternary carbonate fluxes over the following decades.

This review incorporates updated proxy- and model-based estimates of global Quaternary carbonate burial and summarizes progress since the review by Milliman (1993). In the following sections, we summarize the importance of carbonate burial in the modern and Quaternary ocean (Sections 2.2.2-2.2.5) and review the methods commonly used to reconstruct past carbonate burial fluxes in pelagic (Section 2.3) and neritic (Section 2.4) environments. We then evaluate new estimates of global carbonate burial over the Quaternary (Section 2.5) and suggest areas for further work that may address ongoing challenges (Section 2.6).

2.2.1 Definitions

Calcium carbonate saturation state: the product of [Ca^{2+}] and [CO_3^{2-}] in seawater divided by the solubility product for aragonite or calcite; the saturation state determines the solubility of carbonate in seawater.

Carbonate accumulation: vertical export of carbonate to the seafloor plus reef production and imported sediment, less dissolution and lateral transport; also referred to as carbonate burial.

Carbonate compensation depth (CCD): the depth at which carbonate export from the surface ocean is equal to carbonate dissolution, such that no carbonate is preserved below this depth.

Carbonate export: the flux of biogenic carbonate from the surface ocean to the deep sea or seafloor.

Carbonate preservation: the difference between carbonate export and dissolution in the water column or sediments, which ultimately determines how much carbonate is buried.

Carbonate production: precipitation of biogenic carbonate by shallow marine and pelagic calcifiers (e.g., corals, coccolithophores, and foraminifera).

Lysocline: the depth at which carbonate dissolution rapidly increases as a function of the carbonate ion concentration in seawater.

Neritic carbonate: carbonate produced in coastal or shallow marine environments above the continental shelf break (<200 m depth).

Pelagic carbonate: carbonate produced in the open ocean away from the coast (oceanic zone, $>$200 m depth); also known as deep-sea carbonate.

2.2.2 The long-term carbon cycle

Carbonate burial is a key flux in the global carbon cycle (Figure 2.1), which has been described in several books, reviews, and publications (e.g., Archer, 2010; Berner, 2003, 2004; Isson et al., 2020; Sundquist & Visser, 2003; Wallmann & Aloisi, 2012). Here, we provide a brief carbonate-centered summary (Andersson, 2014; Broecker, 2003, 2009).

Dissolved calcium (Ca^{2+}) and bicarbonate (HCO_3^-) in seawater are supplied by continental weathering and utilized by organisms (e.g., foraminifera, coccolithophores, and corals) to form calcium carbonate ($CaCO_3$) shells and skeletons. The three most abundant carbonate minerals in marine sediments are (in order of increasing solubility) calcite, aragonite, and high-magnesium calcite (Andersson, 2014). In general, $CaCO_3$ solubility increases with depth, and dissolution becomes thermodynamically favorable at the saturation horizon, below which lies the lysocline (the depth at which dissolution increases dramatically). The CCD defines the depth where $CaCO_3$ supply is balanced by dissolution and below which no $CaCO_3$ is preserved (Figure 2.1). Where the seafloor lies above the CCD, a fraction of the $CaCO_3$ produced in the ocean is preserved in sediments. Over millions of years, the sequestered carbon is returned to the atmosphere via subduction and volcanism (Figure 2.1).

2.2.3 Effect of carbonate burial on ocean carbonate chemistry and atmospheric CO_2

The effects of carbonate burial on ocean chemistry and atmospheric CO_2 have been thoroughly discussed by Ridgwell and Zeebe (2005) and Zeebe (2012) and briefly summarized here.

Carbonate burial is linked to atmospheric CO_2 by the equilibria of ocean carbonate chemistry (Figure 2.1). In seawater, gaseous CO_2 reacts with water to form carbonic acid (H_2CO_3), which subsequently dissociates into bicarbonate (HCO_3^-) and carbonate (CO_3^{2-}) ions. The sum of these dissolved species is called dissolved inorganic carbon

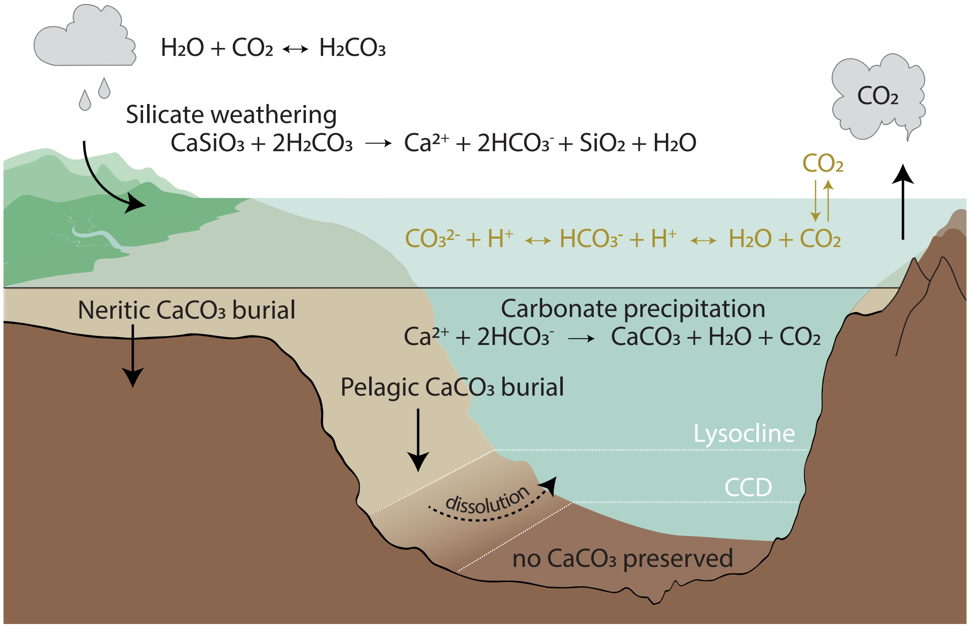

Figure 2.1: The long-term carbon cycle and ocean carbonate chemistry. Silicate weathering and the sequestration of carbon in carbonate sediments balance volcanic release of CO_2 to the atmosphere on million-year timescales (black arrows). Carbonate equilibria between species of dissolved inorganic carbon in seawater (yellow arrows) regulate seawater pH, the precipitation and dissolution of $CaCO_3$,and atmospheric CO_2.

(DIC) (equal to $[HCO_3^-] + [CO_3^{2-}] + [CO_2]$). Total alkalinity (TA) describes the excess of proton acceptors (which provide buffering capacity against acidification) over proton donors in seawater, often expressed as carbonate alkalinity or $[HCO_3^-] + 2[CO_3^{2-}]$, although the strict definition of TA includes additional proton acceptors $[B(OH)_4^-, OH^-, H_3SiO_4^-$, etc.]. The precipitation of $CaCO_3$ lowers DIC and TA by consuming HCO_3^-, counterintuitively increasing pCO_2. The dissolution of $CaCO_3$ in the deep ocean increases DIC and TA. Carbonate compensation maintains a balance between the input of TA from continental weathering and removal of TA by carbonate burial, so that an increase (decrease) in weathering inputs is balanced by a deepening (shoaling) of the CCD and increase (decrease) in carbonate burial (Broecker & Peng, 1982, 1987; Zeebe & Westbroek, 2003). On glacial/interglacial timescales, temporary imbalances caused by reduced carbonate accumulation in the shallow ocean due to sea level regression potentially contributed to changing atmospheric $p\mathrm{CO}_2$ (Berger, 1982; Opdyke & Walker, 1992; Ridgwell et al., 2003; Walker & Opdyke, 1995).

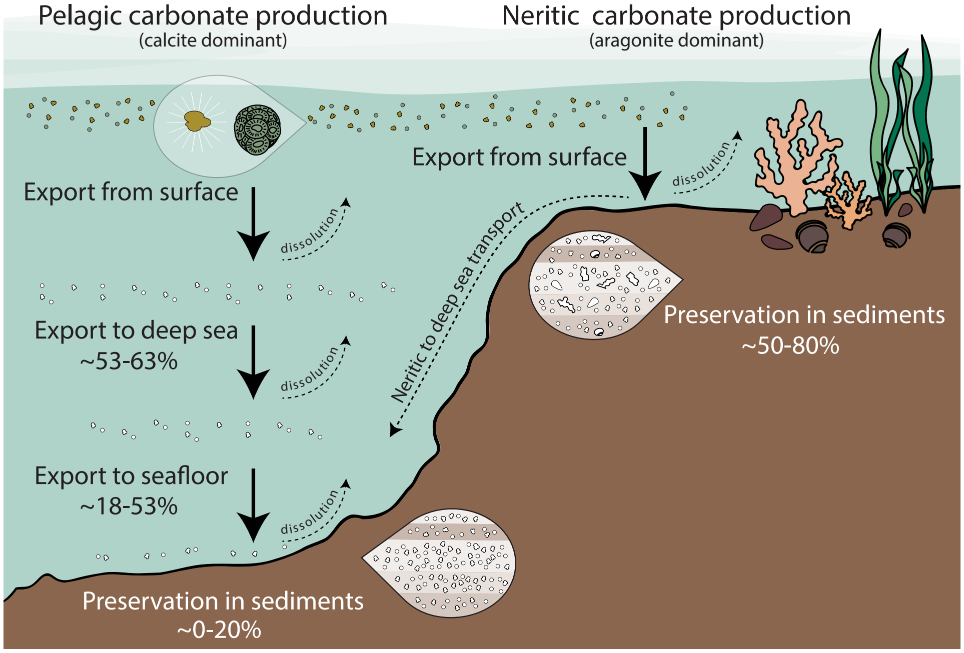

Figure 2.2: Marine carbonate fluxes in neritic (shallow ocean) and pelagic (open ocean) environments. Pelagic carbonate is produced in the surface ocean and exported down through the water column, where ∼47–82% is dissolved before reaching the sediments (Battaglia et al., 2016; Sulpis et al., 2021). An estimated 37–47% of the surface export flux dissolves in the upper water column (<1,500 m depth) (Battaglia et al., 2016; Sulpis et al., 2021), with up to ∼44% dissolution below 1,500 m (Battaglia et al., 2016). Approximately 18–53% of the surface flux makes it to the seafloor, where further dissolution reduces the proportion of buried carbonate to ∼0–20%. Carbonate preservation is higher in neritic environments, where ∼50–80% of the carbonate accumulated by benthic organisms and exported from surfaces waters is preserved (Milliman, 1993; Smith & Mackenzie, 2016). A substantial fraction of neritic carbonate may be transported from shelves and platforms to the deep sea by nepheloid plumes and gravity flows (e.g., Jorry et al., 2020).

2.2.4 Overview of modern carbonate production and burial

Carbonate accumulation depends on production by benthic and planktonic organisms, export from the surface ocean to depth, and preservation on the seafloor (Figure 2.2).

Relatively more aragonite and high-magnesium calcite are produced in neritic environments by organisms such as corals, algae, and echinoderms compared with the deep ocean, where calcite is the dominant phase (Andersson, 2014). In the modern ocean, pelagic carbonate accumulation varies by region and seafloor depth, with higher rates in the Atlantic, eastern equatorial Pacific, and Indian Oceans, where the CCD is deeper, and very little accumulation in the North Pacific and Southern Oceans (Dunne et al., 2012; Hayes et al., 2021) (Figure 2.3B). Key regions of shallow carbonate accumulation are the western Pacific Ocean, eastern Indian Ocean, and Caribbean Sea (O'Mara & Dunne, 2019).

Present-day global carbonate accumulation has been quantified by various approaches, including sediment trap data, core-top measurements, and numerical modeling (e.g., Catubig et al., 1998; Iglesias-Rodriguez et al., 2002; Kleypas, 1997; Milliman, 1993). Global estimates typically rely on site-specific measurements that are interpolated under a set of assumptions (e.g., average production rates across regions, spatial extent of deposition environments, and degree of preservation). Consequently, these global estimates have large uncertainties, particularly in shallow marine environments, where we have little information about export and preservation. Transport of neritic sediments to the deep sea has been well documented, particularly for sea level highstands (Schlager et al., 1994), but quantitative models are necessary to account for this flux in global carbonate budgets. A recent study of an isolated carbonate platform in the Indian Ocean suggested that approximately half of the Holocene $CaCO_3$ production on the platform was transported downslope to the deep basin (Jorry et al., 2020). Further investigation of other regions and neritic settings will be useful for refining this first estimate.

Pelagic carbonate accumulation is well constrained and constitutes approximately half of the carbonate budget (Table 2.1). Though pelagic carbonate production is significantly lower than shallow-water production, the pelagic area ($\sim$300 × 106 km^2) is much larger than other depositional areas (Milliman, 1993). Hayes et al. (2021) recently calculated a Holocene pelagic burial flux of 1.13 ± 0.28 Gt $CaCO_3$ y^{-1}, leveraging a new database of ^{230}Th-normalized sediment fluxes (Costa et al., 2020) with existing sediment composition data. This estimate agrees with the previously estimated range of 0.83–1.25 Gt $CaCO_3$ y^{-1} (Cartapanis et al., 2018).

Table 2.1: Updated global estimates of modern $CaCO_3$ production and accumulation rates across depositional environments. [a]Explicitly includes visible and submerged reef areas. [b]Reef accumulation plus contribution from Halimeda bioherms for 8–0 ka. [c]Total shelf production and accumulation, including tropical and extratropical shelves. [d]Includes imported carbonate flux.[e]Flux at approximately 1,000 m water depth.

Environment	**$CaCO_3$ Production (Gt yr^{-1})**	**$CaCO_3$ Accumulation (Gt yr^{-1})**	**Reference**
Coral reefs	0.9	0.7	Milliman (1993)
	0.9–1.68	NA	Kleypas (1997)
	1.3	NA	Ryan et al. (2001)
	0.9	0.7	Iglesias-Rodriguez et al. (2002)
	0.65–0.83	NA	Vecsei (2004)
	1.6[a]	1.3[a]	Smith & Mackenzie (2016)
	NA	0.7	O'Mara & Dunne (2019)
	NA	1.1[b]	Hinestrosa et al. (2022)
Banks/bays	0.4	0.2	Milliman (1993)
	0.4	0.2	Iglesias-Rodriguez et al. (2002)
	0.2	0.1	Smith & Mackenzie (2016)
	NA	0.36	O'Mara & Dunne (2019)
Carbonate shelves	0.75	0.45	Milliman (1993)
	0.37-1.17	0.47	Iglesias-Rodriguez et al. (2002)
	2.4[c]	0.7[c]	Smith & Mackenzie (2016)
	NA	0.31	O'Mara & Dunne (2019)
Non-carbonate shelves	0.4	0.1	Milliman (1993)
	0.4	0.1	Iglesias-Rodriguez et al. (2002)
	na	0.002	O'Mara & Dunne (2019)
Slopes[d]	0.83	0.58	Milliman (1993)
	0.85	0.6	Milliman & Droxler (1996)
	0.83	0.57	Iglesias-Rodriguez et al. (2002)
Basins	0.03	0.1	Milliman (1993)
Deep sea	2.4[e]	1.1	Milliman (1993)
	NA	0.86	Catubig et al. (1998)
	NA	1.08	Dunne et al. (2012)
	13.3	1.1	Smith & Mackenzie (2016)
	NA	1.14	Cartapanis et al. (2018) sed. data
	NA	1.05	Cartapanis et al. (2018) model
	NA	1.13	Hayes et al. (2021)

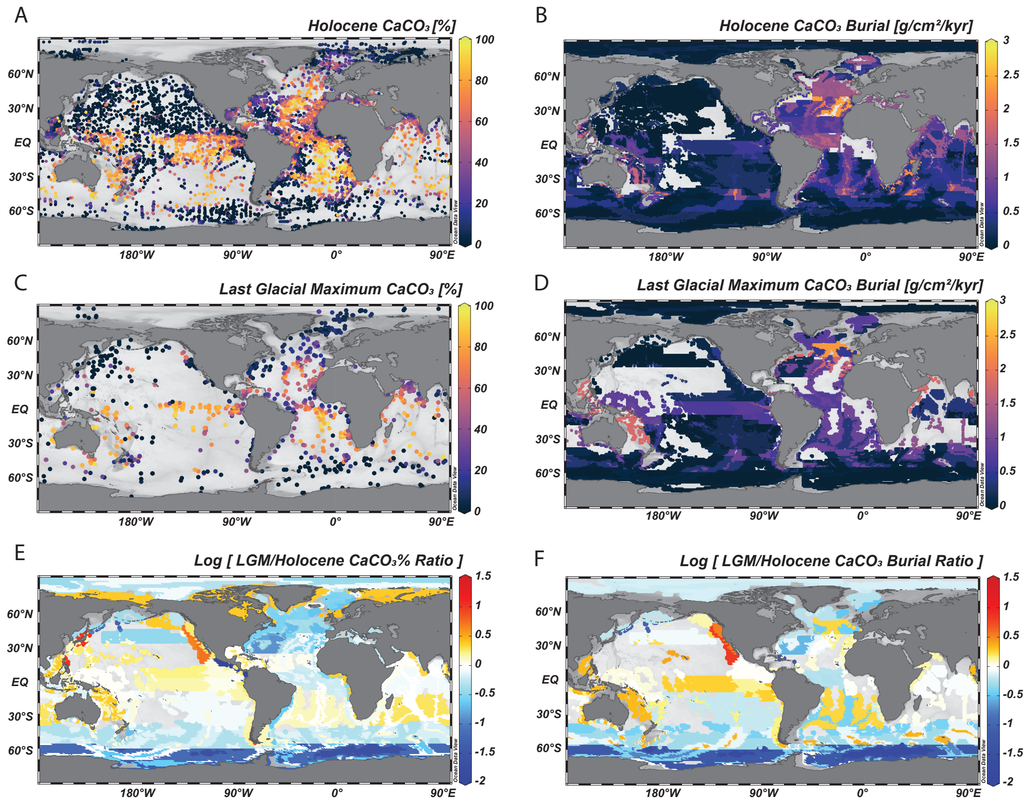

Figure 2.3: (*Top*) (**A**) Holocene (0–10 ka) marine sediment $CaCO_3$ content and (**B**) burial flux. The Holocene $CaCO_3$ content is a compilation of approximately 7,800 direct observations. The burial estimates are made only for water depths greater than 1 km and are based on ^{230}Th-normalized flux observations (Costa et al., 2020) combined with the sediment composition data. Burial fluxes are interpolated within 254 zones based on Longhurst biogeochemical provinces and water depth. Gray zones indicate areas where no data are available. (*Middle*) (**C**) LGM (18.5–23.5 ka) distribution of marine sediment $CaCO_3$ content and (**D**) burial flux interpolated across biogeochemical province and depth zones as described by Hayes et al. (2021) using an LGM compilation of ^{230}Th-normalized fluxes (Costa et al., 2020) and an updated $CaCO_3$ content database for the LGM presented here. (*Bottom*) (**E**) The logarithmic ratios of the LGM $CaCO_3$ content and (**F**) burial flux compared with those of the Holocene (**A** and **B**; (Hayes et al., 2021)). Abbreviation: LGM, Last Glacial Maximum. Panels **A** and **B** adapted with permission from Hayes et al. (2021) (CC BY-NC 4.0).

Sparse observations and poorly constrained preservation and export rates have limited estimates of carbonate accumulation in shallow marine environments (Iglesias-Rodriguez et al., 2002; O'Mara & Dunne, 2019). The latest estimates utilize new data, including bathymetric maps and $CaCO_3$ fluxes derived from satellite data, with improved mapping of neritic community types (O'Mara & Dunne, 2019). Uncertainties associated with burial on carbonate-rich shelves (±39%) and bays (±46%) (O'Mara & Dunne, 2019) were substantially lower than those previously reported (>100% for carbonate-rich shelves, ±100% for bays) (Iglesias-Rodriguez et al., 2002). The uncertainty for carbonate-poor shelf burial (±178%) remains high (O'Mara & Dunne, 2019).

2.2.5 Overview of Quaternary carbonate burial

Quaternary carbonate burial varied over glacial/interglacial cycles due to differences in biological production, ocean circulation, deep-sea sequestration of respired CO_2, and sea level fluctuations (deMenocal et al., 1997; Hain et al., 2014; Jaccard et al., 2009; Kleypas, 1997) (Figure 2.4). The dominant location of carbonate deposition likely shifted from shallow- to deep-water environments during glacial stages due to a reduction in the submerged area of continental shelves, carbonate platforms, and atolls (Berger, 1982; Opdyke & Walker, 1992). Models and observations suggest that while modern carbonate burial rates in neritic and pelagic environments are approximately equal (Milliman, 1993), neritic burial rates would have been lower due to reduced glacial shelf area (Kleypas, 1997).

The coral reef hypothesis (Berger, 1982; Opdyke & Walker, 1992; Ridgwell et al., 2003; Vecsei & Berger, 2004; Walker & Opdyke, 1995) proposed that sea level–driven changes in neritic carbonate burial impacted atmospheric CO_2 concentrations ($p\mathrm{CO}_2$) over the Quaternary. Assuming constant alkalinity input from continental weathering, reduced neritic carbonate burial during glacial periods would increase whole-ocean alkalinity and consequently reduce $p\mathrm{CO}_2$. For the carbonate budget to maintain steady state, increased deep-sea burial must restore the alkalinity balance and stabilize $p\mathrm{CO}_2$ (Sigman & Boyle, 2000). Counterarguments to the coral reef hypothesis have cited lack of evidence for a glacial increase in global deep-sea burial (Archer & Maier-Reimer, 1994; Sigman & Boyle, 2000; Zeebe & Marchitto, 2010). However, the Quaternary carbonate budget may have operated in a nonsteady state imposed by sea level fluctuations (Milliman & Droxler, 1996). Similarly, on short timescales, the assumption of constant alkalinity input may not be maintained due to changes in weathering regimes and weatherability following glacial retreats (Vance et al., 2009). The question of steady state versus non-

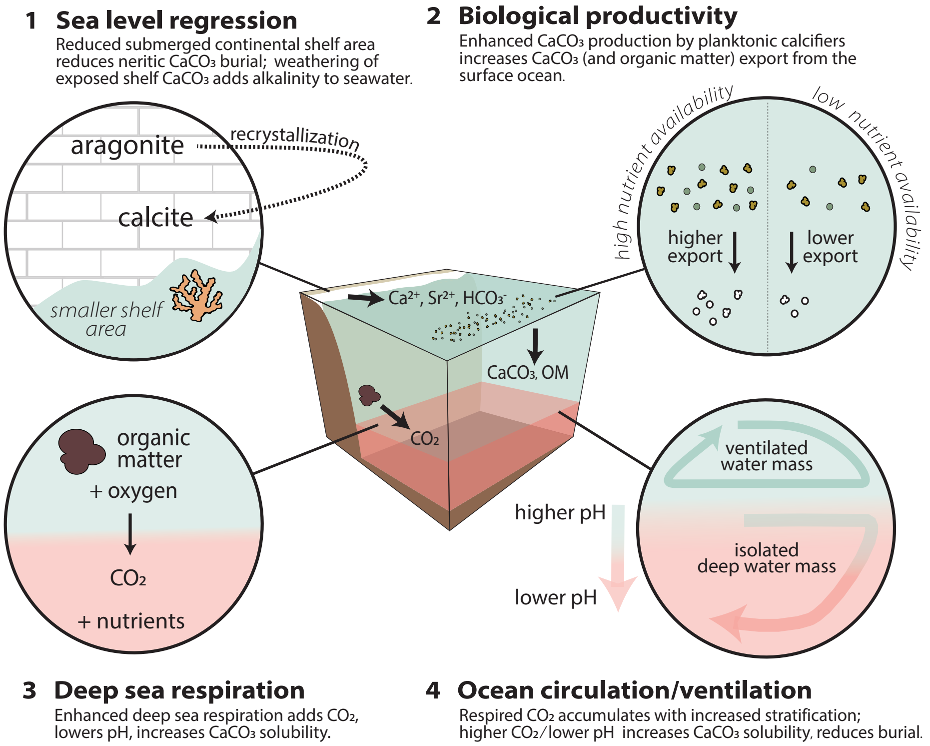

Figure 2.4: Processes hypothesized to alter carbonate burial rates over glacial/interglacial cycles, by changing the carbonate equilibria of the ocean (via inputs of alkalinity or dissolved inorganic carbon), production of biogenic carbonate in the surface ocean, and/or physical area available for carbonate burial (on continental shelves and above the carbonate compensation depth). These processes do not necessarily act in isolation; rather, feedbacks between processes may enhance or balance the effect of others. For example, ocean circulation changes may isolate the deep ocean from the surface, causing the accumulation of respired carbon and limiting mixing of nutrients back to the surface ocean for utilization by calcifiers.

steady state is unanswered but may be resolved as global carbonate burial estimates for glacial/interglacial cycles improve. In Section 2.5, we discuss significant advances toward continuous records of Quaternary carbonate burial, including efforts to model variations in reef productivity since 1,500 ka (Husson et al., 2018) and updated compilations of deep-sea sedimentary records that constrain global pelagic burial during the Holocene, the Last Glacial Maximum (LGM), and continuously over the last 150 ky (Cartapanis et al., 2018; Hayes et al., 2021, this review)

2.3 Methods for reconstructing deep-sea carbonate burial

The marine sedimentary record provides information about pelagic carbonate burial, which varies in space and time due to depth (solubility), regional productivity, lateral transport, CCD position, and dissolution in sediments (Dunne et al., 2012). While past changes in carbonate burial were observed early on in pelagic sediments in the Pacific, Atlantic, and Indian Oceans (e.g., Archer, 1991; Arrhenius, 1952; Balsam & McCoy, 1987; Biscaye et al., 1976; Milliman, 1993), initial reconstructions of pelagic carbonate burial were limited by poor core chronology and sparse observations (Van Andel et al., 1975). Furthermore, while carbonate accumulation records can be obtained from deep-sea sediment cores with relative ease, drilling on slopes is technically difficult, and few $CaCO_3$ accumulation records exist for these environments. Methods for obtaining globally integrated estimates of the pelagic carbonate burial flux from deep-sea sediment cores are summarized below.

2.3.1 Calcium carbonate weight percent

$CaCO_3$ content in sediment cores is widely used to infer changes in carbonate burial through time. $CaCO_3$ wt% is measured using a variety of analytical methods, most commonly coulometry and loss on ignition (Fu et al., 2020; Kastens et al., 1987; Mörth & Backman, 2011). High-resolution scans of physical properties (e.g., bulk density and reflectance spectra) have also been used to determine sediment carbonate content (Vanden Berg & Jarrard, 2002, 2006, and references therein). Despite the relative ease of measuring sediment carbonate content, $CaCO_3$ wt% alone cannot be used to determine accumulation or burial rates because it is a proportional unit and depends on the content of other sedimentary fractions. For the same flux of carbonate delivered to the seafloor, $CaCO_3$ wt% can vary significantly due to dilution by noncarbonate minerals and/or postdepositional dissolution. Comparison of carbonate content between regions is also complicated by spatial variability in dilution and dissolution that may bias $CaCO_3$ wt% values. Consequently, $CaCO_3$ wt% should be converted to a mass flux using a bulk sedimentation rate.

2.3.2 Carbonate mass accumulation rates

Records of $\mathrm{CaCO_3}$ wt% are converted to carbonate mass accumulation rates (MARs; g cm^{-2} ky^{-1}) by:

$$MAR = \frac{\mathrm{CaCO_3}wt\%}{100} * \rho_{dry} * S \tag{2.1}$$

where ρ_{dry} is the dry bulk density (g cm^{-3}) and S is the linear or instantaneous sedimentation rate (cm ky^{-1}). Age model–derived (linear) sedimentation rates have traditionally been used but may be biased by redistribution of sediments on the seafloor (Costa et al., 2020; Francois et al., 2004). Constant flux proxies such as excess ^{230}Th and ^{3}He are now used to derive instantaneous sedimentation rates and can correct for sediment redistribution (e.g.,^{230}Th normalization) (Costa et al., 2020; Francois et al., 2004; McGee et al., 2010). Age model–derived sedimentation rates capture average vertical sedimentation and lateral advection between sampling horizons; instantaneous sedimentation rates reflect only vertical sedimentation (McGee et al., 2010). In most regions of the ocean, constant flux proxies are the preferred method for calculating carbonate (and other sedimentary component) MARs (Costa et al., 2020).

Milliman (1993) reviewed studies of carbonate MARs made possible by age models based on oxygen isotopes and radiocarbon dating that were published before 1993. In the years since 1993, carbonate MARs have been reported in numerous studies and locations in the ocean, some derived from constant flux proxies (Section 2.5.1). Global estimates of deep-sea carbonate burial from MARs require nontrivial compilations of globally extensive MAR records and interpolation between site-specific records to resolve spatial variability (Cartapanis et al., 2018; Catubig et al., 1998; Hayes et al., 2021).

2.3.3 Carbonate compensation depth

Reconstructions of the CCD, which reflects the ocean calcium carbonate saturation state (Ridgwell & Zeebe, 2005), are also used to constrain pelagic carbonate burial. The CCD is operationally defined by the depth of a specific sedimentary $\mathrm{CaCO_3}$ wt% (e.g., Van Andel, 1975) or the depth at which carbonate accumulation rates approach zero (Lyle, 2003). Although the position of the CCD is relatively easy to identify with sediment cores, linking changes in the CCD to carbonate burial can be challenging due to potential decoupling between carbonate burial and the CCD response. The recent approach of Boudreau and Luo (2017), who modeled global pelagic carbonate burial based on the Cenozoic CCD, is relevant only to secular timescales (>0.5 Ma, not applicable to glacial/interglacial cycles). In general, extrapolating CCD reconstructions from a particular ocean basin to a global CCD record is complicated by ocean circulation, which could shift the CCD regionally (Greene et al., 2019). Furthermore, burial of excess $CaCO_3$ above the CCD could cause a decoupling of the CCD and global carbonate burial (Greene et al., 2019) such that changes in ocean alkalinity are accommodated by increased burial above a relatively stable CCD.

During the Quaternary, the Pacific CCD appears to have remained relatively stable despite large sea level fluctuations (Farrell & Prell, 1989; Lyle, 2003; Lyle et al., 2008; Pälike et al., 2012). The lack of significant CCD change during glacial/interglacial cycles may be explained by reduced sensitivity of the Cenozoic CCD to shifts in shelf carbonate burial following the CCD deepening and reduction of shelf carbonate globally at the Eocene–Oligocene transition (∼34 Ma) (Armstrong McKay, 2015). In this case, shifts in shelf–basin partitioning of carbonate burial in response to glacial/interglacial sea level change (or other mechanisms of alkalinity transfer) may not be evident in Quaternary CCD records but rather reflected in changes in the carbonate accumulation between the lysocline and the CCD, which is much harder to assess. Regional shifts in the lysocline can be inferred from observed carbonate dissolution cycles on glacial/interglacial timescales. Anticorrelated Pacific–Atlantic preservation cycles are well documented for the Pleistocene (e.g., Farrell & Prell, 1989), and carbonate dissolution cycles similar to those in the Pacific have been observed throughout the Indian Ocean (Bassinot et al., 1994). In general, preservation of carbonate in the Pacific and Indian Oceans is enhanced during glacial periods, while sediments in the Atlantic experience increased dissolution; the reverse is true during interglacial periods. Though carbonate preservation and dissolution are clearly linked to glacial/interglacial cycles, the challenge is to determine whether opposing changes in different ocean basins maintained a relatively constant global pelagic $CaCO_3$ accumulation rate or were imbalanced such that a net change in global carbonate burial occurred.

2.4 Methods for reconstructing neritic carbonate burial

The heterogeneous nature of carbonate production across neritic environments is a significant challenge to global reconstructions because they require extrapolation of locally reconstructed production (or burial) rates. Furthermore, since carbonate production in these environments is especially sensitive to sea level fluctuations, nutrient levels, temperature, and salinity, production (and burial) rates may vary through time depending on environmental conditions. Variable preservation, erosion, and transport of neritic sediments further complicate carbonate burial estimates in this zone. Below, we highlight approaches that have been used to investigate changes in neritic carbonate burial through time as well as their limitations.

2.4.1 Fossil coral reefs

Coral reefs constitute a substantial fraction of global carbonate production and accumulation, yet quantifying this contribution remains challenging because observation-based estimates are often region or reef specific. Methods for observing reef production include hydrochemistry, census data, accumulated sediments, and numerical modeling; Vecsei (2004a) provided a detailed review of these methods and previous estimates, including modeling by Kleypas (1997). These approaches often suffer from insufficient data and large uncertainties that are magnified when scaling local and regional studies to global estimates. Current reef production estimates for the Holocene range from 0.65 to 1.68 Gt $CaCO_3$ y^{-1} and, as Vecsei (2004a, p. 12) succinctly noted, are "fraught with substantial, unquantified uncertainties." Several reef accumulation estimates agree with Milliman's (1993) early estimate of 0.7 Gt $CaCO_3$ y^{-1}, with uncertainty in the range of 100% (Table 2.1). Importantly, estimates typically exclude carbonate mounds formed by cold-water corals, which have been documented throughout the ocean and may contribute significantly to carbonate budgets but whose accumulation rates are even more poorly quantified than those of tropical reefs (e.g., Hebbeln et al., 2019; Lindberg & Mienert, 2005; Titschack et al., 2015, 2016).

Constraining reef production, preservation, and geographic extent becomes increasingly difficult the further back one goes in geologic history. Coral reef accumulation is not constant through time or space and varies with changing sea level. Direct measurements of reef accretion rates through time can be made by radiometric dating of growth stages (Camoin et al., 2001, e.g.,), but current observations are sparse and limited by diagenesis, lack of dateable material required for U/Th chronology, and absence of lowstand reef units (Camoin & Webster, 2015). Without widespread observations, we require an alternative approach for estimating Quaternary reef carbonate burial prior to the LGM. In Section 2.5.3, we discuss recent studies that have turned to numerical modeling to simulate reef production and predict global accumulation rates (Husson et al., 2018; Jones et al., 2015).

2.4.2 Other carbonate burial sinks

Besides corals, the shallow ocean hosts an array of habitats and communities of calcifiers that contribute to the global carbonate budget but are currently underestimated, due largely to spatial heterogeneity. Carbonate production can be locally monitored in the water column (using sediment traps) or on benthic substrates (for example, colonization experiments with calcification accretion units), though these measurements can be biased by horizontal transport of material and may differ from actual burial rates due to postdepositional dissolution in sediments. Extrapolating local studies to global rates requires that the habitat preferences and distributions of species be well estimated, which remains a challenge at present. For example, *Halimeda* algae are thought to be important contributors to carbonate production in the tropics, but the geographic extent of *Halimeda* accumulation is uncertain and very likely underestimated (McNeil et al., 2016, 2020; Rees et al., 2006). Hinestrosa et al. (2022) recently estimated that at least 590 Gt $CaCO_3$ accumulation by *Halimeda* must be added to global Holocene carbonate budgets (compared with Holocene and drowned reef deposits of ~8,100 Gt and ~1,500 Gt $CaCO_3$, respectively) based on their regional study of the Great Barrier Reef. Other benthic calcifiers, such as echinoderms, are probably also underestimated (e.g., Lebrato et al., 2010). A combination of habitat-specific carbonate production or accumulation rates and global surveys of habitat extent is needed to compile accurate neritic carbonate budgets.

2.5 Quaternary carbonate burial reconstructions

2.5.1 Deep-sea carbonate burial

A primary goal for reconstructing pelagic carbonate burial over the Quaternary is to test whether pelagic burial increased during glacial periods. This hypothesis is based on the expectation that neritic carbonate burial was reduced during glacial periods relative to interglacials, when lower sea level reduced the area available for neritic carbonate accumulation (Kleypas, 1997) (Figure 2.4). To maintain a steady-state carbonate budget during a glacial period, carbonate compensation would deepen the CCD and increase deep-sea carbonate burial. Thus, LGM pelagic carbonate burial was predicted to exceed the modern rate by up to two times in a steady-state ocean (Catubig et al., 1998).

To test this expectation, Catubig et al. (1998) used a compilation of records mainly from the Pacific and Atlantic Oceans to compare global Holocene and LGM carbonate burial. Their compilation suggested that deep-sea LGM burial rates were higher than those of the Holocene in the Pacific and North Atlantic but lower in the South Atlantic, Indian, and Southern Oceans. Notably, the South Pacific had a higher $CaCO_3$ wt% during the LGM but was excluded from their analyses for lack of MAR data. The study found no significant difference in global deep-sea carbonate burial between the Holocene (0.86 Gt y^{-1}) and LGM (0.92 Gt y^{-1}), challenging the premise that increased pelagic carbonate burial compensated for lower neritic burial during glacial periods and the assumption of a steady-state carbonate budget on these timescales.

As chronostratigraphy improved and drilling programs expanded over the next two decades, carbonate MAR records became more reliable and more numerous (Anderson et al., 2008; Campbell et al., 2018; Lyle, 2003; Lyle et al., 2005, 2019; Pälike et al., 2012; Vanden Berg & Jarrard, 2004). The first continuous reconstruction of global deep-sea carbonate burial over the last glacial cycle, by Cartapanis et al. (2018), used a compilation of 637 sediment records (Figure 2.5). To account for the spatial variability of carbonate accumulation, this study identified biogeochemical provinces based on modern carbonate MARs (Dunne et al., 2012) and reconstructed carbonate accumulation in each province over the past 150 ky from available MARs. The global reconstruction showed that carbonate accumulation was similar during the present-day interglacial and marine isotope stage (MIS) 5e, with lower burial during MIS 4 (78% ± 9% of the Holocene value) and MIS 2 (85% ± 7% of the Holocene value); the absolute magnitude of these changes depended on the province map used.

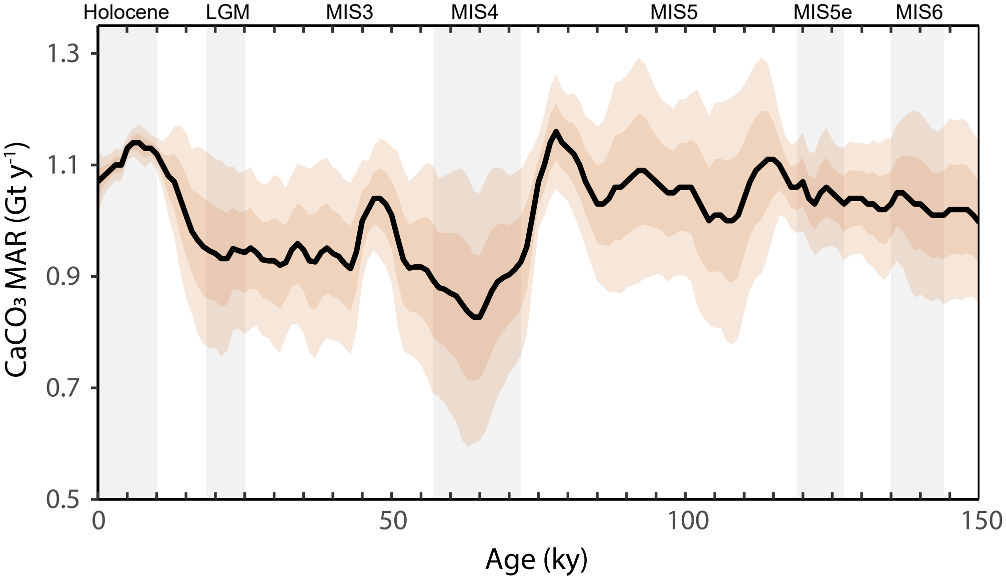

Figure 2.5: Global deep-sea carbonate mass accumulation rate over the last glacial cycle, as reconstructed by Cartapanis et al. (2018). The black curve shows the mean of 20 scenarios using different biogeochemical province maps, with shaded regions indicating $\pm 1\sigma$ and $\pm 2\sigma$. Gray vertical bars delineate glacial (LGM, MIS 4, MIS 6) and interglacial (Holocene, MIS 5e) periods. Abbreviations: LGM, Last Glacial Maximum; MIS, marine isotope stage. Figure adapted from Cartapanis et al. (2018) (CC BY 4.0).

Despite being unable to entirely resolve the challenges of spatial heterogeneity, this reconstruction represented a major step forward, providing a continuous record over an entire glacial cycle and revealing minima during glaciation that could not be resolved by the two-end-member study by Catubig et al. (1998). While both Cartapanis et al. (2018) and Catubig et al. (1998) observed glacial $CaCO_3$ concentrations greater than Holocene values in the Pacific, consistent with the findings of Farrell and Prell (1989), Cartapanis et al. (2018) found that the glacial increase in the Pacific was not sufficient to balance the decrease in the Atlantic. Neither reconstruction supports increased global pelagic carbonate burial during glacial periods; rather, they suggest that pelagic burial did not compensate for the expected decrease in neritic burial.

2.5.2 Updated ^{230}Th-normalized Last Glacial Maximum deep-sea carbonate burial fluxes

A new database of ^{230}Th-normalized sediment fluxes by Costa et al. (2020) provides an opportunity to revise these estimates for the LGM. As Hayes et al. (2021) did for the Holocene (Figure 2.3A,B), here we newly compile published $CaCO_3$ wt% data for the LGM (Figure 2.3C,D) and combine these composition data with the LGM sediment fluxes (Costa et al., 2020). This allows us to estimate ^{230}Th-normalized $CaCO_3$ burial fluxes for the deep sea at the LGM (defined here as 18.5–23.5 ka) and compare them with those of the Holocene (Figure 2.3E,F).

For the LGM $CaCO_3$ wt% distribution, we utilized previous compilations (Cartapanis et al., 2018; Catubig et al., 1998) and added 95 new observations, for a total database of 898 observations (see online Supplemental Material at doi.org/10.1146/annurev-marine-031122-031137). Reduced $CaCO_3$ content during the LGM compared with the Holocene is seen clearly throughout most of the Atlantic, Southern, and Arctic Oceans. Increased LGM $CaCO_3$ content is seen in the equatorial Pacific and Indian Oceans as well as the Australian, Indonesian, and Arctic shelf seas. However, as mentioned above, these changes in $CaCO_3$ content may not be reflective of actual changes in burial due to variable dilution from other phases and/or changes in the total sedimentation rate.

Our new estimates of LGM carbonate burial are restrained to deep-sea sites (deeper than 1 km), where the assumptions of the ^{230}Th-normalization method are valid (Costa et al., 2020). Additionally, the distribution of ^{230}Th-normalized flux observations for the LGM is sparser than that for the Holocene, resulting in a larger proportion of ocean provinces that cannot currently be characterized. For instance, the Holocene map of ^{230}Th-normalized fluxes covered 87% of the deep-sea area (Hayes et al., 2021), while the areal coverage for the LGM is 49.5%. Nonetheless, sufficient coverage of key regions in the ocean produces results that can help determine LGM carbonate burial changes. With more geographic detail than previously available, we find clear evidence for increased LGM carbonate burial compared with the Holocene in the equatorial Pacific and decreased carbonate burial in most of the North Atlantic and Southern Oceans (Figure 2.3F). These observations are consistent with the hypothesis that glacial/interglacial carbonate burial variations result mainly from changes in carbonate preservation in the deep ocean, associated with a major change in deep-sea CO2 storage (e.g., Anderson et al., 2008; Yu et al., 2020). Nonetheless, recent work on modern $CaCO_3$ export fluxes in the water column is revealing previously unrecognized biological production influences on $CaCO_3$ sedimentation, such as the influence of aragonite on calcite preservation (Sulpis et al., 2021, 2022), and there is still much to be discovered about how the LGM calcifier ecosystem was different from today's.

While our interpolated LGM $CaCO_3$ burial map can be used to derive a deep-sea LGM $CaCO_3$ burial sink, some notes on its uncertainty must be mentioned due to its geographic sparseness. We assessed the accuracy of our interpolated LGM $CaCO_3$ burial estimates by comparing predicted $CaCO_3$ burial values with those from the 103 sites where ^{230}Th-normalized $CaCO_3$ fluxes have been observed directly. This analysis results in a root mean square error of 29% of the observed burial flux range. We use this relative root mean square error as our assumed uncertainty in deriving a global LGM $CaCO_3$ burial flux. Furthermore, there is some geographic bias in the areas for which no fluxes can currently be derived, with the lowest coverage in the Indian Ocean (Figure 2.3D). We therefore used a basin-specific scaling factor to correct for the relative amounts of seafloor missing from the interpolated estimates, aimed at matching the same areal distribution in our Holocene interpolation (Figure 2.3B) for better comparison.

This process results in a deep-sea LGM burial of 1.3 ± 0.4 Gt $CaCO_3$ y^{-1}, within the error of our Holocene estimate (1.1 ± 0.3 Gt $CaCO_3$ y^{-1}). This analysis adds to the evidence that total deep-sea $CaCO_3$ burial did not change over glacial cycles but makes clear that there were basinwide fractionations in $CaCO_3$ burial. For instance, the Holocene balance of $CaCO_3$ burial between basins is 40% Atlantic, 22% Pacific, 20% Indian, 17% Southern, and 0.4% Arctic (Hayes et al. 2021; note that in this scheme the Southern Ocean is defined as south of 40°S). By contrast, in our LGM $CaCO_3$ burial reconstruction the balance is 33% Atlantic, 41% Pacific, 17% Indian, 10% Southern, and $<$0.1% Arctic. This suggests that the increased glacial $CaCO_3$ burial in the Pacific was balanced by reduced carbonate burial in all other basins, rather than only in the Atlantic, as had first been theorized (Balsam, 1983; Crowley, 1985; Farrell & Prell, 1989). More estimates of glacial period ^{230}Th-normalized fluxes from the key gap regions highlighted in Figure 2.3D will be necessary to investigate this possibility further.

2.5.3 Quaternary coral reef accumulation

Fossil coral reefs are important archives of Quaternary sea level change and reef accumulation (see reviews by Dullo (2005) and Camoin and Webster (2015). Notable reef sequences used to characterize the last deglaciation include those obtained from Barbados (e.g., Fairbanks, 1989), Tahiti (e.g., Camoin et al., 2012), and the Great Barrier Reef (e.g., Webster et al., 2018; Yokoyama et al., 2018), while drilling efforts in regions such as New Caledonia have yielded records extending through earlier glacial stages (e.g., Cabioch et al., 2008; Montaggioni et al., 2011). An exceptional example is the 300-ky record obtained by Camoin et al. (2001), which contains both sea level high- and lowstand reef units, an uncommon achievement in coral reef drilling (Camoin & Webster, 2015). More recently, the 30-ky record from the Great Barrier Reef documented reef accretion rates and the presence of shelf-edge reefs during the LGM (Webster et al., 2018; Yokoyama et al., 2018). Such direct observations constrain reef establishment and productivity only for specific locations, so global estimates of reef productivity rely on a limited number of records to be representative of reefs globally (e.g., Hinestrosa et al., 2022; Ryan et al., 2001; Vecsei & Berger, 2004).

Based on the recent data from the Great Barrier Reef (Webster et al., 2018; Yokoyama et al., 2018), Hinestrosa et al. (2022) attempted a global estimate of postglacial reef accumulation that accounted for both Holocene reef accumulation and drowned reefs (established on the shelf edge during the LGM). They reported global estimates of ∼1 GtCaCO$_3$ y^{-1} for Holocene reefs (80 ka) and 0.2 Gt CaCO$_3$ y^{-1} for drowned reefs (19–10 ka), noting that the extrapolation from Great Barrier Reef estimates to global estimates strongly depends on the value used for global reef area. In any case, the finding that drowned reefs may equal ∼16–40% of the Holocene reef deposits at the Great Barrier Reef suggests an important role for drowned reefs in the global carbonate budget, and the calculated rate of accumulation for drowned reefs prior to 8 ka is similar to a previous estimate by Vecsei and Berger (2004).

Vecsei and Berger (2004) estimated global reef accumulation since the LGM by combining fossil records from tropical and subtropical reefs and using sea level records and reef depth distributions to identify patterns of reef production. They concluded that reef production during the LGM and initial deglaciation (∼21–14 ka) was low (we note that accretion during the 19-ka meltwater pulse (Clark et al., 2004) may have contributed but is not quantified here), while the late deglaciation (∼10–6 ka) saw the highest production with slowing sea level rise (Vecsei & Berger, 2004). Based on an estimate of 80% preservation for reef carbonate from Milliman (1993) and the extrapolation of modern reef area to past reefs, reef accumulation for 0–6 ka, 6–8 ka, and 8–14 ka was estimated to be 0.23, 0.41, and 0.12 Gt $CaCO_3 y^{-1}$, respectively. Though limited by a range of uncertainties (e.g., past reef area, global extrapolation of production rates and preservation, contribution from fore reefs and temperate shelves, and intermittent productivity), these estimates are conservative and imply at least a threefold increase in reef accumulation from the LGM (<0.12 Gt $CaCO_3$ y^{-1}) to peak deglacial accumulation (0.41 Gt $CaCO_3$ y^{-1}). The cumulative reef accumulation since 14 ka (∼2,900 Gt $CaCO_3$) was estimated to account for 211 Gt of carbon emissions over the same period; adding conservative estimates for accumulation on isolated banks and platforms (∼250 Gt $CaCO_3$) raised the emissions estimate to 225 Gt of carbon released as CO2 (Vecsei, 2004a; Vecsei & Berger, 2004). The effect on atmospheric $p\mathrm{CO}_2$ ultimately depended on the emission rate and uptake by the deep ocean or terrestrial biosphere. These findings were broadly supportive of the coral reef hypothesis (Berger, 1982; Opdyke & Walker, 1992), with increased coral growth (and CO_2 emissions) coinciding with rising sea level and flooding of continental shelves, where reef habitat is prevalent.

The approach of Vecsei and Berger (2004) cannot reliably be applied to periods earlier than the LGM due to the scarcity of preserved reef records. To assess coral reef accumulation over the Pleistocene, continuous accumulation records extending over multiple glacial cycles are needed. Obtaining such records from direct observations is currently out of reach, yet numerical modeling offers an alternative approach for global reef accumulation reconstructions. Coral calcification rates have been modeled as a function of environmental factors (e.g., water temperature, light, and carbonate saturation state) to predict reef responses to environmental change (Jones et al., 2015; Kleypas, 1997; Kleypas et al., 2011; Lough, 2008; Silverman et al., 2007, 2009). While these models are geared toward understanding how future environmental change will impact reefs, they also provide a means of estimating reef production for given environmental conditions. For instance, O'Mara and Dunne (2019) utilized the coral productivity models of Kleypas (1997), Lough (2008), and Silverman et al. (2007) in their estimation of modern neritic carbonate burial (Section 2.2.4).

Over long timescales, reef productivity also depends on sea level oscillations, uplift, subsidence, substrate morphology, and coastal erosion (Husson et al., 2018). Husson et al. (2018) assumed that the physicochemical factors important for local reef production (e.g., temperature, light, and carbonate saturation state) cancel out on a global scale, so that external factors such as uplift, subsidence, and erosion are the primary drivers of global reef productivity during the Quaternary. Their numerical model simulated reef productivity in response to sea level change, uplift, subsidence, and erosion over 1,500 ky, advancing beyond the modeling of individual reef systems (reviewed in Camoin & Webster, 2015) by extrapolating globally (Husson et al., 2018). Taking the last glacial period as representative, the model predicted near-zero reef productivity during sea level regression, a gradual increase during deglaciation to peak Early Holocene productivity (∼1.9 Gt $CaCO_3$ y^{-1} around 10 ka), and a slight decrease to the Late Holocene. The timing of the late deglacial production peak aligns with prior observations (Vecsei & Berger, 2004), and the predicted Late Holocene production rate (∼0.8 Gt $CaCO_3$ y^{-1}) agrees well with observation-based modern estimates (Table 2.1). Across the entire simulation, peak production occurred ∼5 ky prior to sea level maxima and lasted several thousand years, with typical values from 2.5 to 4.5 Gt $CaCO_3$ y^{-1} for most late deglacial periods and maxima calculated at MIS 11 and MIS 31 (>10 Gt $CaCO_3$ y^{-1}) (Husson et al., 2018). Lowstands were characterized by negligible production rates.

Global reef accumulation rates were not reported by Husson et al. (2018); accurate conversion of production rates to accumulation rates will require better knowledge of the preservation of reef carbonate over the past 1,500 ky. Approximating 80% preservation (Milliman, 1993) yields peak deglacial accumulation rates of 1.5 Gt $CaCO_3$ y^{-1} for the Holocene (more than three times greater than the peak estimate of Vecsei and Berger (2004)) and 2.0–3.6 Gt $CaCO_3$ y^{-1} for most deglaciations, with negligible accumulation during the LGM and other glacial lowstands. Based on their productivity estimates, Husson et al. (2018) predicted ∼1,400 Gt of carbon released as CO2 during the last deglaciation (20–7 ka).

2.5.4 Quaternary carbonate burial on banks, shelves, and slopes

Past carbonate burial on banks, continental shelves, and slopes has remained difficult to estimate for a variety of reasons, particularly the significant spatial and temporal heterogeneity in carbonate production and accumulation (Section 2.4.2). Current observations are insufficient for compiling a globally representative record of Quaternary carbonate burial in these environments, but localized studies offer some insight into their role in the global carbonate budget. For example, Vecsei (2004b) evaluated carbonate production on isolated carbonate banks (0 to ∼70 m depth) from 0 to 20 ka and concluded that carbonate production was low during rapid sea level rise from the LGM to ∼14 ka, with episodically increasing production after 14 ka and peak production after 6 ka as sea level rise slowed. The study included only banks at low latitudes since the geographic and depth distributions of high-latitude banks are poorly known; this limitation may be addressed in the future with numerical modeling. Recent work by Laugié et al. (2019) extended the modeling of coral reefs discussed in Section 2.5.3 by developing a model of shallow marine carbonate factories in the modern ocean as a function of sea surface temperature and salinity, depth, and primary productivity. Their modeling framework demonstrates the potential for deriving geographic distributions of shallow marine carbonates from oceanographic parameters, which could meet the ongoing need for better spatial characterization in the modern and past ocean.

Continental shelf carbonate burial fluxes are highly location specific due to numerous factors that influence production, transport, and preservation (e.g., upwelling nutrients, riverine fluxes, terrigenous sediment accumulation, presence of *Halimeda* algae, latitude, and seasonality). Consequently, local studies provide depositional models only for certain biogeochemical and oceanographic conditions. For instance, a study of Late Quaternary sediments on the Ross Sea shelf provided insight into carbonate accumulation in a high-energy, glaciation, polar shelf environment (Frank et al., 2014). The scarcity and complexity of these local observations hinder our ability to improve upon the approximation of the global continental shelf carbonate flux made by Milliman (1993), which relied on broad assumptions about the geographic area and average composition of shelf sediments.

Where observations are insufficient, modeling can provide some constraints on shallow burial fluxes. van der Ploeg et al. (2019) used an alkalinity mass balance model to estimate Cenozoic global carbonate burial along continental margins. Though the contributions of each shallow marine setting cannot be distinguished by this approach, the model yields global neritic carbonate burial estimates that integrate the contributions of each environment. This modeling approach could potentially be applied over shorter timescales (e.g., glacial/interglacial cycles) to resolve changes in neritic carbonate burial. Importantly, the alkalinity input from weathering and the pelagic burial flux must be well constrained over the time interval of interest to solve for the neritic carbonate burial flux using the alkalinity mass balance model. Moreover, this modeling approach assumes steady state (mass balance) in alkalinity input and output on the relevant timescales, which may not hold for the short timescales of glacial/interglacial sea level fluctuations.

2.5.5 Summary

The available Quaternary reconstructions of pelagic carbonate burial do not indicate that global carbonate burial in the deep sea increased during glacial periods, as would be expected if steady state were maintained over glacial cycles. Our updated compilation of ^{230}Th-normalized LGM carbonate burial fluxes provides further evidence that LGM burial rates were the same as those during the Holocene (within error). The MAR-based reconstruction by Cartapanis et al. (2018) suggested burial minima during glacial periods, which would exacerbate the buildup of ocean alkalinity from the dissolution of exposed shelf carbonates. Records derived from fossil coral reefs generally confirm that reef accumulation accelerated during the transition from the LGM to interglacial conditions, yet only a few global estimates based on observations and modeling are available for the Quaternary. The bank, shelf, and slope carbonate sinks are still poorly constrained, but recent efforts have demonstrated the potential for modeling of neritic carbonate burial to fill the observational gaps.

2.6 Ongoing challenges and opportunities

Despite the advances described in the preceding sections, our quantitative grasp of global glacial/interglacial carbonate burial remains limited. Significant uncertainties persist even for estimates of modern export, dissolution, and burial fluxes (e.g., Battaglia et al., 2016; Sulpis et al., 2021, 2022). A robust quantitative understanding of present-day carbonate burial is necessary if we expect to accurately estimate burial fluxes in the past and compare across glacial/interglacial cycles. We require greater attention to carbonate production, export, and preservation in marginal environments, where our observations are sparse, yet we expect sea level–driven variations in burial over the glacial/interglacial cycles. On a global scale, proxies that are incorporated into carbonate and recorded in marine sediments, such as strontium and calcium isotopes, provide new opportunities to generate continuous records reflecting carbonate burial through time.

2.6.1 Heterogeneous neritic carbonate sinks

As noted throughout this review, the complex mosaic of habitats on carbonate shelves, platforms, and reefs is a primary complication in estimating total carbonate production and sedimentation. In addition to corals, shallow marine organisms such as echinoderms (Lebrato et al., 2010), *Halimeda* algae (Drew, 1983), and calcifiers living in seagrass ecosystems (Mazarrasa et al., 2015) produce significant amounts of neritic carbonate sediment, but their inclusion in global carbonate budgets has been limited. To better represent the contributions of these groups, we need new methods for characterizing their distribution and abundance. Since carbonate sedimentation by these calcifying organisms varies by species and habitat (e.g., Castro-Sanguino et al., 2020; de Macêdo Carneiro & de Morais, 2016; de Macêdo Carneiro et al., 2018; Mazarrasa et al., 2015; Perry et al., 2017, 2019), the coverage of habitat type must be known in addition to within-habitat species abundance and sedimentation rates. Provided that there are adequate field-based estimates of the latter, satellite imagery might be leveraged to define habitat coverage (e.g., Perry et al., 2019; Utami et al., 2018) to scale localized studies to regional carbonate budgets for the modern shallow ocean.

2.6.2 *Halimeda* bioherms

Recent studies of the *Halimeda* bioherms of the Great Barrier Reef demonstrated that this component of the Holocene neritic carbonate budget has been vastly underestimated. The biohermsmounds of accumulated *Halimeda* skeletal fragments—record accumulation of *Halimeda* carbonate in some regions (for detailed descriptions of *Halimeda* bioherms, see Davies (2011) and (McNeil et al., 2020)). New mapping with airborne lidar and multibeam bathymetry revealed that the Great Barrier Reef bioherms covered three times the previously estimated area (McNeil et al., 2016). With carbonate volumes equal to or greater than the adjacent coral reefs (Rees et al., 2006), these bioherms contributed significantly more to the shelf carbonate budget than has been accounted for (Iglesias-Rodriguez et al., 2002; Milliman, 1993). Comparable volumes of carbonate were mapped on a carbonate platform off northwestern India (Rao et al., 2018). Globally extrapolating Great Barrier Reef *Halimeda* accumulation yields an estimated increase of ∼4–8% in the Holocene carbonate budget (Hinestrosa et al., 2022).

Other identified (but inadequately mapped) regions of Holocene bioherms include Kalukalukuang Bank in the eastern Java Sea, the Nicaraguan Rise in the southwest Caribbean, and the Big Bank Shoals in the Timor Sea (McNeil et al., 2020). Older fossil bioherms have been found on the Fifty Fathom Flat, India (Late Quaternary); Funafuti, Tuvalu (Pleistocene); the Solomon Islands (Pleistocene); and Vanuatu (Pliocene to Pleistocene) and have been studied little since their discoveries (McNeil et al., 2020). Estimates of the carbonate inventories of these bioherms, which will require updated mapping and analyses of carbonate content, can improve our estimates of how much carbonate was buried on shelves and platforms when these were flooded during interglacial periods.

2.6.3 Geochemical proxies

Given the challenges of estimating global carbonate burial from direct observations, we can turn to geochemical proxies that reflect a global signal of the integrated carbonate fluxes. The precipitation of carbonate incorporates not only calcium (Ca^{2+}) but also trace amounts of magnesium (Mg^{2+}) and strontium (Sr^{2+}) into the crystal structure. The effect of carbonate burial on the global ocean inventories of these elements and their isotopes, which in some cases are fractionated between seawater and precipitating carbonate, is recorded in the elemental ratios and isotopic composition of marine sediments. While magnesium isotope records indicate that carbonate deposition is not a primary control on seawater magnesium over the Cenozoic (Gothmann et al., 2017; Higgins & Schrag, 2015), seawater Sr/Ca ratios (Stoll & Schrag, 1998), strontium isotopes (Paytan et al., 2021), and calcium isotopes (Fantle, 2010; Griffith & Fantle, 2020) may be sensitive to glacial/interglacial variations in carbonate burial and thus serve as useful global proxies.

Strontium/calcium ratio

Strontium is added to the ocean by continental weathering and hydrothermal activity and removed by the precipitation of both neritic aragonite (strontium rich) and pelagic calcite (strontium poor). Due to the enrichment of strontium in aragonite (DSr $\approx$ 1 for aragonite, compared with DSr $\approx$ 0.1 for calcite), the ocean strontium inventory is strongly influenced by the burial of shelf aragonite, with a smaller effect from the partitioning of carbonate burial between the shallow and deep ocean (Graham et al., 1982; Schlanger, 1988; Stoll & Schrag, 1998). During glacial periods, sea level regression exposed continental shelves where metastable aragonite recrystallized to calcite and released large amounts of strontium to the ocean that were only partially reprecipitated in calcite. Such a change in seawater strontium concentrations would theoretically be reflected in the Sr/Ca ratio of seawater, as calcium is conserved during aragonite recrystallization, though concurrent variation in calcium fluxes could mute the change in the strontium/calcium ratio (Stoll & Schrag, 1998).

Stoll and Schrag (1998) modeled a 1–3% change in seawater Sr/Ca over glacial/interglacial cycles, but direct reconstructions using planktic and benthic foraminifera yielded differing records with greater variability (Martin et al., 1999; Stoll et al., 1999). Reconstructing seawater Sr/Ca is an ongoing challenge, as illustrated by conflicting records of Cenozoic seawater Sr/Ca derived from gastropods, $CaCO_3$ veins, benthic foraminifera, fish teeth, corals, and belemnites/rudists (Balter et al., 2011; Coggon et al., 2010; Ivany et al., 2004; Lear et al., 2003; Sosdian et al., 2012; Steuber & Veizer, 2002; Tripati et al., 2009). Such reconstructions are complicated by secondary effects such as growth rate, selective dissolution, and carbonate ion saturation, which influence carbonate Sr/Ca ratios to varying degrees depending on species (Elderfield et al., 2000; Stoll et al., 1999; Tripati et al., 2009; Yu, Elderfield, et al., 2014). Furthermore, Lebrato et al. (2020) demonstrated significant global variability in modern seawater Sr/Ca ratios and suggested that regional environmental effects contributed to the differences among paleo seawater Sr/Ca records. Marine barite has been proposed as an alternative archive of seawater Sr/Ca (Averyt & Paytan, 2003), as barite is not subject to the same biological effects as biogenic carbonate, but the potential influence of other factors (e.g., water depth) on barite strontium content has not been fully explored (Griffith & Paytan, 2012). Despite these limitations, records of seawater strontium concentrations should not be discounted as a means of inferring carbonate burial rates. Among the next steps is further investigation of archives such as marine barite that may passively record seawater chemistry without biological or preservation effects.

Stable strontium isotopes

The stable strontium isotopic composition of seawater ($\delta^{88/86}$Sr) provides a new constraint on the ocean strontium budget (in addition to the traditional radiogenic strontium isotope ratio, ^{87}Sr/^{86}Sr) (Krabbenhöft et al., 2010; Paytan et al., 2021; Pearce et al., 2015; Vollstädt et al., 2014). Due to the fractionation of stable strontium isotopes between seawater and carbonate (-0.18‰) and the enrichment of strontium in aragonite, seawater $\delta^{88/86}$Sr is sensitive to neritic carbonate burial and recrystallization. Paytan et al. (2021) published a seawater $\delta^{88/86}$Sr record derived from marine barite over the past 35 My, demonstrating that $\delta^{88/86}$Sr can be used to estimate variations in the ocean strontium inventory and infer changes in neritic carbonate burial. Significant variability in Quaternary seawater $\delta^{88/86}$Sr values suggests that the effect of glacial/interglacial shifts in shallow marine carbonate burial may be resolved with a high-resolution record (Paytan et al., 2021).

Stable calcium isotopes

Calcium isotopes also provide new insight, though their application to reconstructing past carbonate burial is not straightforward. Weathering is the primary input of calcium to the ocean, while $CaCO_3$ sedimentation removes calcium with a large fractionation of δ^{44}Ca (approximately -1.3‰) between seawater and $CaCO_3$ (Griffith & Fantle, 2020). Though imbalances between the weathering and carbonate burial fluxes would theoretically be reflected by changes in seawater δ^{44}Ca, there is uncertainty around the assumption of a constant seawater-carbonate fractionation factor through time and the fidelity of calcium isotope archives (for an in-depth review of calcium isotopes and their application to the global calcium cycle, see Griffith and Fantle (2020)). As future work resolves these issues, reconstructions of seawater calcium isotopes may prove useful for inferring carbonate burial changes.

Non-steady-state modeling

The potentially dynamic cycles of strontium and calcium in the ocean (e.g., Griffith et al., 2008; Paytan et al., 2021; Vance et al., 2009) can be modeled using the additional budget constraints provided by the geochemical proxies discussed above. Despite the long residence times of calcium (∼1 My) and strontium (∼2.5 My), extreme changes in weathering or carbonate sedimentation can drive budget imbalances over shorter timescales (e.g., glacial/interglacial cycles). There is little evidence that the decrease in neritic carbonate burial during glacial periods was compensated for by an increase in deep-sea burial. Deglacial changes in weathering regimes and weatherability are also possible (Vance et al., 2009). If we relax the assumption that the ocean strontium and calcium cycles were at steady state over the Quaternary, changes in the $\delta^{88/86}$Sr and δ^{44}Ca of seawater may reflect transient imbalances in the weathering and carbonate burial fluxes (e.g., De La Rocha & DePaolo, 2000; Griffith et al., 2008; Krabbenhöft et al., 2010; Paytan et al., 2021; Vollstädt et al., 2014). Though using these isotopic records to obtain continuous records of past global carbonate burial will require robust constraints on input fluxes and isotopic composition, this is a promising approach for quantifying Quaternary carbonate burial.

2.7 Conclusions

Significant advances in quantifying present-day and Quaternary carbonate burial have been made over the last few decades. Compilations of deep-sea carbonate accumulation records yielded improved global flux estimates for the Holocene and LGM. Various modeling approaches have been used to better quantify burial fluxes in shallow marine environments. Increasing recognition of underestimated components of the neritic carbonate budget has prompted investigations of carbonate accumulation by *Halimeda* algae, echinoderms, and other shallow-ocean dwellers that must be incorporated into future carbonate budgets.

Nevertheless, accurate reconstruction of global carbonate burial over glacial/interglacial timescales remains challenging, largely due to the difficulty of obtaining a continuous global record from discrete observations. Continued exploration of glacial-age carbonate fluxes throughout the deep sea will help evaluate hypotheses related to the geographic variations in carbonate burial. Emerging paleoceanographic proxies such as the stable strontium and calcium isotope systems can also help fill these gaps.

The links between marine carbonate burial and atmospheric $p\mathrm{CO}_2$ via the ocean carbonate system prompted the idea that sea level–driven shifts in carbonate burial had an impact on Quaternary climate, potentially accounting for ∼6–20 ppm of the observed ∼90 ppm $p\mathrm{CO}_2$ rise recorded in ice cores from the LGM to Holocene (Kohfeld & Ridgwell, 2009; Ridgwell et al., 2003). The magnitude and consequences of this mechanism may only be fully explored when we have confidently quantified the global carbonate burial fluxes in the shallow and deep ocean over glacial/interglacial cycles.

2.8 Acknowledgements

Insightful and constructive comments from J. Zachos and an anonymous reviewer for *Annual Review of Marine Science* greatly improved this review, as did rigorous editing of the manuscript by Production Editor J. Duncan.

Chapter 3

Stable and radiogenic strontium isotopes trace the composition and diagenetic alteration of remnant glacial seawater

This chapter has been submitted to *Geochimica et Cosmochimica Acta*: Wood, M.M., Blättler, C.L., Kolevica, A., Eisenhauer, A., Paytan, A. Stable and radiogenic strontium isotopes trace the composition and diagenetic alteration of remnant glacial seawater. Data can be accessed via the Mendeley Data Repository at doi.org/10.17632/xs738ckr2m.1.

3.1 Abstract

A remnant of glacial seawater preserved in the pore fluids of sediment cores from the Maldives Inner Sea provided an opportunity to investigate the stable strontium isotopic composition ($\delta^{88/86}$Sr) of the ocean during the Last Glacial Maximum and explore the usefulness of $\delta^{88/86}$Sr as a tracer of early marine diagenesis. We used paired measurements of $\delta^{88/86}$Sr and radiogenic Sr isotope ratios (^{87}Sr/^{86}Sr) in pore fluids and surrounding carbonate sediments to constrain the diagenetic history of the preserved glacial water mass at IODP Sites U1466 and U1468. These pore fluid profiles document variability in $\delta^{88/86}$Sr in a shallow marine setting, revealing distinct diagenetic processes dominating within different depth intervals. We find evidence for isotope fractionation during secondary calcite precipitation at intermediate depths and observe that in aragonite-dominated settings, fractionation during recrystallization may be obscured by the dissolution of aragonite in the uppermost sediments. Correcting for the effect of carbonate recrystallization on pore fluid Sr concentration ([Sr]) and isotopic composition, we estimate that glacial seawater [Sr] was higher (∼98 μM) and $\delta^{88/86}$Sr lower (∼0.32‰) compared to the modern ocean, consistent with hypotheses attributing the present-day disequilibrium of the ocean Sr budget to glacial/interglacial changes in shelf carbonate weathering and burial. Our results provide evidence that the ocean Sr inventory and $\delta^{88/86}$Sr are sensitive to carbon cycle changes on timescales much shorter than its residence time (∼2 Myr) and demonstrate that pore fluid $\delta^{88/86}$Sr measurements are a useful addition to multi-tracer studies of diagenesis in complex marine systems.

3.2 Introduction

Efforts to reconstruct glacial seawater chemistry predominantly rely on indirect proxy evidence in sediments or fossils that can be translated to the elemental and isotopic composition of the past ocean. Such reconstructions are inherently subject to uncertainties stemming from, for example, imperfect preservation of the sediment archives, biological or temperature effects, or assumptions of constant isotope fractionation through time. The discovery of a preserved remnant of Last Glacial Maximum (LGM) seawater in the interstitial fluids of a carbonate platform in the Maldives Inner Sea yielded a new archive from which geochemical properties of glacial seawater may be more directly derived (Blättler et al., 2019). The glacial-age pore fluids recovered by International Ocean Discovery Program Expedition 359 record increases in chloride concentrations, oxygen isotope ratios (δ^{18}O) and deuterium isotope ratios (δD) of 25 mM (4.5% change in chloride), 1.2‰, and 9‰, respectively, consistent with an LGM origin. Analyses of reactive geochemical tracers (strontium concentrations and calcium isotope ratios) revealed complex reactive histories for the water masses at these sites but suggest that the shallowest glacial pore fluids have been only minimally altered by reactions with the carbonate sediments (Figures 3.1 and 3.2) (Blättler et al., 2019). These minimally-altered pore fluids offer a unique archive for investigating the chemical composition of seawater during the LGM.

The stable strontium isotopic composition ($\delta^{88/86}$Sr) of glacial seawater is of particular interest, as several studies have converged on the idea that non-steady-state processes operating over glacial/interglacial cycles drove imbalances in the strontium (Sr) budget and fluctuations in seawater $\delta^{88/86}$Sr (Krabbenhöft et al., 2010; Mokadem et al., 2015; Paytan et al., 2021; Pearce et al., 2015; Vance et al., 2009). The ocean Sr budget is presently not in equilibrium (Davis et al., 2003; Krabbenhöft et al., 2010; Pearce et al., 2015; Vance et al., 2009). The rate of change in seawater radiogenic Sr isotope ratios (^{87}Sr/^{86}Sr) calculated based on modern fluxes is ~8 times faster than the observed rate over the past few million years, suggesting high modern weathering rates relative to the long-term rate (Vance et al., 2009). However, a post-glacial increase in continental weathering cannot alone explain the modern isotopic disequilibrium of seawater $\delta^{88/86}$Sr; isotopic mass balance requires an additional source of isotopically light Sr, which may have been supplied by weathering and recrystallization of exposed shallow marine carbonate (aragonite) during the last glacial period (Krabbenhöft et al., 2010). The predicted equilibrium of the glacial Sr budget is thought to have been perturbed by sea level rise during deglaciation that cut off the carbonate weathering flux from the exposed continental shelf and increased the flooded shelf area available for shallow marine carbonate burial. Neritic aragonite deposits are rich in Sr with low $\delta^{88/86}$Sr relative to seawater due to isotope fractionation during carbonate precipitation, so changes in shallow carbonate weathering and burial can influence both the ocean Sr inventory and $\delta^{88/86}$Sr (Krabbenhöft et al., 2010; Pearce et al., 2015). In contrast, seawater ^{87}Sr/^{86}Sr is not sensitive to mass-dependent fractionation in carbonates and has been shown to be constant within analytical error over the last 40 kyr, limiting possible changes in continental weathering to less than 12% (Henderson et al., 1994; Mokadem et al., 2015). Combined constraints on glacial seawater ^{87}Sr/^{86}Sr and $\delta^{88/86}$Sr could more fully characterize the glacial Sr budget and provide a new test of predicted glacial/interglacial changes in the shelf carbonate fluxes.

Previous work relying on numerical models predicted an increase in glacial seawater Sr concentration ([Sr]) due to the shelf recrystallization mechanism (Stoll & Schrag, 1998; Stoll et al., 1999), which holds important implications for the carbonate chemistry of the ocean and related changes in atmospheric carbon dioxide over glacial/interglacial cycles (Berger, 1982; Opdyke & Walker, 1992; Walker & Opdyke, 1995). The addition of Sr to the glacial ocean from recrystallizing shelf carbonates would also be expected to lower seawater $\delta^{88/86}$Sr relative to the modern value if the flux was large enough to affect the ocean Sr inventory. Limited data exist to constrain the possible glacial increase in [Sr] (modeled by Stoll and Schrag (1998) as only a ~2% increase in Sr/Ca). The only published data for Pleistocene seawater $\delta^{88/86}$Sr, reconstructed using marine barite, indeed suggest that the average Late Quaternary seawater $\delta^{88/86}$Sr was ~0.04‰ lower than today, with the range in $\delta^{88/86}$Sr corresponding to a calculated ≤25% increase in [Sr] (Paytan et al., 2021). The Maldives pore fluid archive that is the focus of this study suggests the possibility that glacial seawater [Sr] could have been higher than today. The remnant LGM seawater [Sr] (~120 to 150 μM) is elevated compared to the modern concentration (88 μM). These higher concentrations could reflect some degree of carbonate recrystallization (Blättler et al., 2019) and possibly a higher Sr inventory in the glacial ocean associated with the shelf recrystallization hypothesis (Berger, 1982; Stoll & Schrag, 1998).

In order to utilize the Maldives pore fluids as an archive of glacial seawater chemistry, it is critical to correct for any alteration of the remnant LGM water mass through sediment-fluid reactions. The diagenesis of carbonate in contact with marine pore fluids can impart changes in pore fluid geochemistry, including [Sr] and the isotopes of Sr, calcium, and magnesium among other tracers (Fantle et al., 2010; Fantle & DePaolo, 2007; Fantle & Higgins, 2014; Geske et al., 2015; Higgins & Schrag, 2012; Higgins et al., 2018; Riechelmann et al., 2016). The effect of carbonate recrystallization on pore fluid $\delta^{88/86}$Sr in shallow marine sediments has not been studied, with only one previous study documenting these processes within deep-sea sediments (Voigt et al., 2015), but it is expected that the effect may be more substantial in shallow marine environments given the prevalence of Sr-rich aragonite, the much higher concentration of Sr in aragonite compared to pore fluids, and the fractionation of ^{88}Sr/^{86}Sr between carbonate and seawater (Fietzke & Eisenhauer, 2006; Krabbenhöft et al., 2010). At the Maldives sites, Blättler et al. (2019) used both pore fluid [Sr] and calcium isotope ratios ($\delta^{44/40}$Ca) to identify depth intervals where the LGM water mass had been only minimally altered by carbonate recrystallization. These intervals (referred to hereafter as the "best-preserved glacial" intervals) are the main target for our investigation of

$\delta^{88/86}$Sr. However, we note that even a small degree of carbonate recrystallization can alter the pore fluid $\delta^{88/86}$Sr composition and must be accounted for. Pore fluid ^{87}Sr/^{86}Sr, which is often used as a tracer of carbonate recrystallization (Fantle et al., 2010; Fantle & DePaolo, 2006; Richter & DePaolo, 1987, 1988), constrains the extent of carbonate recrystallization at these sites and aids our interpretation of the pore fluid $\delta^{88/86}$Sr profiles. Our combined measurements of ^{87}Sr/^{86}Sr and $\delta^{88/86}$Sr provide new insight to the alteration of the best-preserved glacial water at Sites U1466 and U1468 and the effect of early marine diagenesis on pore fluid and carbonate $\delta^{88/86}$Sr.

We show that the best-preserved glacial seawater at the Maldives sites has been more extensively altered than previously inferred and that the contribution of carbonate recrystallization to the measured pore fluid Sr chemistry can be constrained using ^{87}Sr/^{86}Sr and [Sr], providing a means of estimating glacial seawater $\delta^{88/86}$Sr. These measurements of pore fluid $\delta^{88/86}$Sr in a shallow carbonate platform setting reveal distinct diagenetic processes dominating at different depth intervals and demonstrate the usefulness of pore fluid $\delta^{88/86}$Sr in multiple-tracer studies of complex carbonate systems.

3.3 Materials and Methods

3.3.1 Site description and background

International Ocean Discovery Program Expedition 359 recovered sediment cores at eight sites including Site U1466 (4°55.99'N, 73°1.69'E, 518 m water depth) and Site U1468 (4°55.98'N, 73°4.28'E, 521 m water depth) in the Maldives Inner Sea, drilling into a drowned carbonate platform and overlying drift deposits of Miocene to Pleistocene age (Betzler et al., 2017). Measurements of conservative tracers (δ^{18}O, δD, chloride concentrations) and reactive tracers for carbonate recrystallization ([Sr], $\delta^{44/40}$Ca) in pore fluids extracted from these cores were used to identify the origin of advected water masses in the carbonate platform and their diagenetic histories (Blättler et al., 2019). The conservative tracer profiles were interpreted as reflecting distinct water masses of different ages: an interglacial (likely Holocene) water mass with $\delta^{18}\text{O} \approx 0.3‰$, $\delta\text{D} \approx 3‰$, and chloride $\approx$ 559 µM (0 to ∼60 mbsf) and a glacial water mass with $\delta^{18}\text{O} \approx 1.5‰$, $\delta\text{D} \approx 12‰$, and chloride $\approx$ 584 µM (∼70 to ∼400 mbsf) (Blättler et al., 2019). Below 400 mbsf, the conservative tracers return to the interglacial seawater values. The profiles of [Sr] and $\delta^{44/40}$Ca generally reflect variable degrees of carbonate recrystallization (aragonite-to-calcite neomorphism and calcite-to-calcite recrystallization) at different depths and along the upstream advective paths of the fluids (Blättler et al., 2019). The conversion of Sr-rich aragonite to Sr-poor calcite releases Sr to pore fluids, while pore fluid $\delta^{44/40}$Ca decreases toward equilibrium with the sediments (which have lower $\delta^{44/40}$Ca than seawater due to the $\sim$-1.0–1.5‰ average fractionation between precipitating carbonate and seawater) (Fantle & DePaolo, 2007; Fantle & Tipper, 2014; Turchyn & DePaolo, 2011). The reactive tracers shed light on the diagenetic histories of the water masses distinguished by the conservative tracers: the Holocene water mass remains largely unaltered by exchange with the sediments (0 to 60 mbsf), the uppermost glacial water mass (the best-preserved glacial interval) was interpreted as having minimal input of recrystallized carbonate ($\sim$70 to $\sim$110 mbsf at Site U1466, $\sim$70 to $\sim$170 mbsf at Site U1468), and the deeper glacial water mass has undergone extensive reaction with carbonate sediments ($>$110 mbsf at Site U1466, $>$170 mbsf at Site U1468) (Blättler et al., 2019) (Figures 3.1 and 3.2).

3.3.2 Sample selection

We analyzed ^{87}Sr/^{86}Sr and $\delta^{88/86}$Sr in pore fluids sampling the distinct Holocene and glacial water masses identified by Blättler et al. (2019) at Sites U1466 and U1468 (Table 3.1). We sampled coarsely throughout the depth intervals of pore fluid recovery (maximum recovery depths of 309 mbsf and 838 mbsf at Site U1466 and Site U1468, respectively). Selected samples from Site U1466 span depths of 0 to 261 mbsf while samples from Site U1468 reach up to 799 mbsf, though we focused mainly in the upper 300 m. Pore fluid recovery was limited by lithification at greater depths. The pore fluids in the sampled intervals are primarily within Miocene carbonate sediments, with Pleistocene/Pliocene drift deposits in the upper 50 to 70 m (Betzler et al., 2018). Five carbonate samples from Site U1468 spanning 30 to 680 mbsf were also analyzed to characterize the Sr isotopic composition of the sediments in contact with the pore fluids (Table 3.2).

Table 3.1: Pore fluid Sr isotope measurements at Site U1466 and Site U1468 with internal precision given by $2\sigma_{mean}$. Asterisks indicate preparation replicate samples.

Site	**Hole**	**Core**	**Type**	**Sect**	**Depth (mbsf)**	$\delta^{88/86}$**Sr**	$2\sigma_{mean}$	**n**	^{87}**Sr**/^{86}**Sr**	$2\sigma_{mean}$
U1466	A	1	H	1	0	0.391	0.009	4	0.709167	0.000006
U1466	A	1	H	2	2.96	0.350	0.009	4	0.709164	0.000010
U1466	A	2	H	4	10.96	0.335	0.002	4	0.709153	0.000008
U1466	A	3	H	4	20.45	0.333	0.003	4	0.709155	0.000001
U1466	A	4	H	4	29.74	0.350	0.003	2	0.709135	0.000003
U1466	A	5	H	4	39.4	0.325	0.000	2	0.709129	0.000004
U1466	A	5	H	4	39.4*	0.330	0.004	4	0.709154	0.000010
U1466	A	6	H	4	48.9	0.324	0.008	2	0.709129	0.000009
U1466	A	8	H	4	67.9	0.272	0.006	2	0.709098	0.000014
U1466	A	9	H	4	76.9	0.285	0.006	4	0.709081	0.000007
U1466	A	11	H	4	92.6	0.287	0.009	4	0.709085	0.000004
U1466	A	11	H	4	92.6*	0.291	0.004	4	0.709083	0.000008
U1466	A	13	H	4	106.4	0.247	0.005	4	0.709031	0.000001
U1466	A	15	H	4	125.4	0.186	0.002	4	0.709014	0.000001
U1466	A	19	F	2	148.5	0.156	0.002	4	0.708944	0.000001
U1466	A	21	H	4	159.68	0.138	0.006	4	0.708937	0.000004
U1466	A	28	F	2	195.81	0.159	0.006	2	0.708902	0.000003
U1466	A	40	F	2	261	0.193	0.004	4	0.708901	0.000002
U1468	A	1	H	1	0	0.364	0.009	4	0.709182	0.000005
U1468	A	2	H	3	7.4	0.354	0.005	2	0.709149	0.000004
U1468	A	4	H	4	27.85	0.362	0.005	4	0.709162	0.000009
U1468	A	4	H	4	27.85*	0.342	0.014	4	0.709146	0.000001
U1468	A	6	H	4	47.35	0.348	0.009	4	0.709118	0.000002
U1468	A	8	H	4	66.3	0.358	0.003	4	0.709115	0.000001
U1468	A	10	H	4	85.3	0.338	0.003	4	0.709114	0.000004
U1468	A	12	H	4	102.65	0.335	0.003	2	0.709104	0.000005
U1468	A	12	H	4	102.65*	0.337	0.009	4	0.709107	0.000002
U1468	A	14	F	2	115.5	0.336	0.001	2	0.709107	0.000001
U1468	A	20	F	2	137.7	0.302	0.006	4	0.709106	0.000002
U1468	A	22	F	2	148.2	0.275	0.006	4	0.709095	0.000007
U1468	A	30	F	2	190.6	0.077	0.005	4	0.708895	0.000004
U1468	A	37	F	1	217.6	0.172	0.001	4	0.708867	0.000001
U1468	A	48	F	1	302.1	0.264	0.003	4	0.708867	0.000006
U1468	A	53	X	2	327.35	0.281	0.002	4	0.708879	0.000006
U1468	A	53	X	2	327.35*	0.289	0.001	4	0.708881	0.000005
U1468	A	61	X	4	385.1	0.285	0.025	4	0.708915	0.000002
U1468	A	61	X	4	385.1*	0.286	0.006	4	0.708898	0.000010
U1468	A	74	X	3	509.91	0.315	0.009	4	0.708844	0.000006
U1468	A	74	X	3	509.91*	0.332	0.001	4	0.708829	0.000001
U1468	A	74	X	3	509.91*	0.324	0.008	4	0.708844	0.000002
U1468	A	89	X	2	653.42	0.483	0.006	4	0.708765	0.000008
U1468	A	104	X	2	799.41	0.514	0.001	4	0.708630	0.000004

Table 3.2: Carbonate Sr isotope measurements at Site U1468 with internal precision given by $2\sigma_{mean}$. Asterisks indicate preparation replicate samples.

Site	**Hole**	**Core**	**Type**	**Sect**	**Depth (mbsf)**	$\delta^{88/86}$**Sr**	$2\sigma_{mean}$	**n**	^{87}**Sr**/^{86}**Sr**	$2\sigma_{mean}$
U1468	A	4	H	4	27.9	0.170	0.018	4	0.709097	0.000006
U1468	A	4	H	4	27.9*	0.190	0.016	4	0.709059	0.000002
U1468	A	14	F	2	115.6	0.230	0.011	4	0.708857	0.000010
U1468	A	30	F	2	190.7	0.310	0.007	4	0.708888	0.000007
U1468	A	30	F	2	190.7*	0.330	0.004	4	0.708850	0.000001
U1468	A	63	X	2	401.6	0.290	0.007	4	0.708839	0.000006
U1468	A	92	X	1	680.79	0.290	0.005	4	0.708471	0.000001

3.3.3 Sample preparation

Pore fluids were extracted shipboard by standard methods as reported in Blättler et al. (2019). We processed carbonate samples from squeeze cake bulk sediments according to a carbonate leaching method where approximately 100 mg of powdered sample was weighed into acid washed 50 mL centrifuge tubes. Samples were rinsed three times with ultrapure water to remove non-bound Sr, shaken and centrifuged, and the supernatant was decanted. The carbonate was dissolved using triple-distilled 0.75N HCl which was briefly reacted with the sample, centrifuged, and decanted. Pore fluids and dissolved carbonates were measured for elemental composition by inductively coupled plasma optical emission spectrometry and the resulting [Sr] of each sample was used to determine the amount of ^{87}Sr/^{84}Sr spike to be added to a volume containing 600 ng Sr. Strontium from both spiked and un-spiked (used to measure ^{87}Sr/^{86}Sr) aliquots was purified using Eichrom's Sr-Spec stick/non-stick resin on 1 mL Bio-Rad columns (Krabbenhöft et al., 2010; Krabbenhöft et al., 2009). Following cleaning and conditioning steps, the sample was loaded onto the column and washed with 5 mL of triple-distilled 8N HNO_3 before Sr was eluted with 7 mL of triple-distilled 0.05N HNO_3. Procedural Sr blanks for the carbonate leaching and column procedures were <1.5 ng and <0.5 ng, respectively, which are sufficiently low for the sample size prepared (<0.3%).

3.3.4 Strontium isotope analyses

Radiogenic and stable Sr isotope analyses were carried out at GEOMAR-Helmholtz Center for Ocean Research Kiel (Germany) using the double-spike thermal ionization mass spectrometry (DS-TIMS) method detailed by Krabbenhöft et al. (2009). In short, approximately 600 ng Sr was loaded onto degassed rhenium filaments with a tantalum activator, dried, and heated briefly at 2 A before loading on the TIMS. A single measurement requires separate analyses of an ^{87}Sr/^{84}Sr-spiked sample and an unspiked sample, from which the ^{88}Sr/^{86}Sr ratios were calculated by the double spike correction algorithm and reported in delta notation as $\delta^{88/86}$Sr (‰) = (^{88}Sr/^{86}Sr$_{sample}$/ ^{88}Sr/^{86}Sr$_{SRM987}$ - 1) * 1000. We report the traditional radiogenic Sr isotope value ^{87}Sr/^{86}Sr normalized to a ^{88}Sr/^{86}Sr ratio of 8.375209. The typical internal precision for an individual measurement is <0.00001 for ^{87}Sr/^{86}Sr and <0.01 for ^{88}Sr/^{86}Sr (shown in Tables 3.1 and 3.2). The external reproducibility, which fully captures the variability introduced by the chemical preparation, was determined by repeated measurements of the JCp-1 coral standard ($\delta^{88/86}$Sr =0.19±0.01‰, ^{87}Sr/^{86}Sr,=0.70918±0.00002, n=9), the IAPSO seawater standard ($\delta^{88/86}$Sr =0.39±0.01‰, ^{87}Sr/^{86}Sr,=0.709174±0.000007, n=10), and NIST® SRM® 987 ($\delta^{88/86}$Sr =0.00±0.02‰, ^{87}Sr/^{86}Sr,=0.71026±0.00002, n=6) separately processed by Sr-Spec chromatography.

3.4 Results

3.4.1 Pore fluid $\delta^{88/86}$Sr and ^{87}Sr/^{86}Sr

At Site U1466, pore fluid [Sr] in the upper 10 meters of the core is similar to modern seawater (88 μM), increasing to ∼150 μM between 10 and 30 mbsf (Figure 3.1). Below 110 meters depth, [Sr] rapidly increases to greater than ∼400 μM. The $\delta^{88/86}$Sr profile shows opposing shifts to [Sr] with depth, decreasing from 0.4‰ at the core top to 0.33‰ over the upper 20 meters and maintaining this value until about 50 meters depth. Between 100 and 160 mbsf, $\delta^{88/86}$Sr rapidly decreases to a minimum value of 0.14‰ as [Sr] increases. Below 160 mbsf, $\delta^{88/86}$Sr increases back to 0.19‰ in the deepest sample. Radiogenic Sr decreases with depth from 0.709167 to 0.708901, with the greatest shift in ^{87}Sr/^{86}Sr occurring between 70 and 160 meters depth (0.709081 to 0.708937).

Site U1468 pore fluids exhibit similar trends but differ significantly from the Site U1466 profiles within the best-preserved glacial interval (70–170 mbsf) and extend to greater depths (Figure 3.2). Strontium concentrations increase from 87 μM to 130 μM in the upper 30 meters and plateau until below 150 mbsf. Between 150 and 500 mbsf, [Sr] reaches 450 μM before decreasing from 400μM to ∼220 μM between 500 and 800 mbsf.

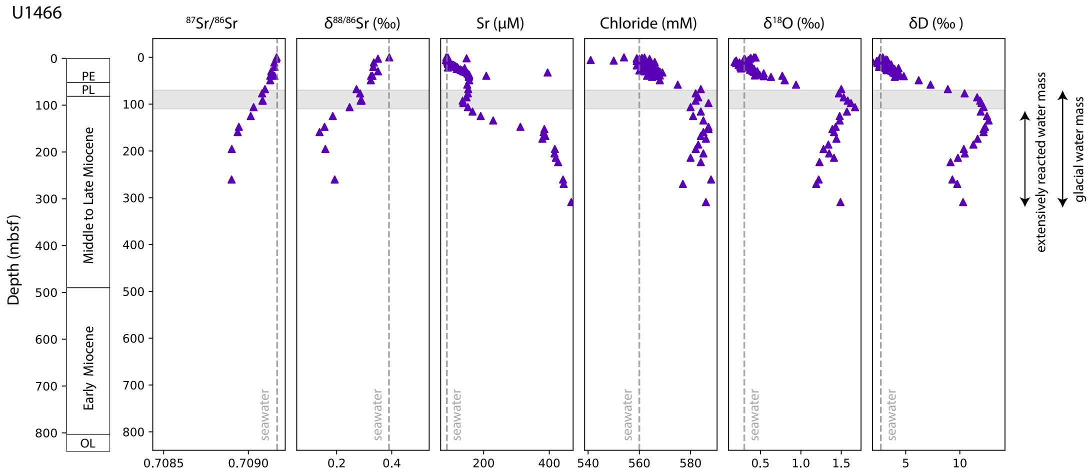

Figure 3.1: Site U1466 pore fluid profiles of ^{87}Sr/^{86}Sr and $\delta^{88/86}$Sr measured in this study, with published [Sr], chloride concentrations, δ^{18}O, and δD profiles (Blättler et al., 2019). The best-preserved glacial interval (70 to 110 mbsf) is indicated by the shaded region and is defined based on the conservative tracers (chloride, δ^{18}O, δD) and [Sr] as in Blättler et al. (2019). Modern seawater compositions are shown by the dashed vertical lines.

The $\delta^{88/86}$Sr values show considerably less variation within the upper 150 meters compared to the Site U1466 profile, gradually decreasing from 0.36 to 0.34‰ between 0 and 120 mbsf, to 0.28‰ at ∼150 mbsf. The $\delta^{88/86}$Sr minimum (0.08‰) is reached at 190 meters before $\delta^{88/86}$Sr begins increasing to a maximum value of 0.51‰ at 800 mbsf. As at Site U1466, pore fluid ^{87}Sr/^{86}Sr at Site U1468 decreases with depth but does so much more gradually between 0–150 mbsf (0.709182 to 0.709095). The pore fluid ^{87}Sr/^{86}Sr values are more radiogenic (higher) than the bulk carbonate values, most significantly so in the 70–170 mbsf depth interval and around 700 mbsf. Below 150 mbsf, Site 1468 ^{87}Sr/^{86}Sr values are similar to those at comparable depths at Site U1466.

Cross plots of [Sr] versus ^{87}Sr/^{86}Sr and $\delta^{88/86}$Sr illustrate the trends that are broadly shared between the two sites and highlight some key differences (Figure 3.3). Both sites show generally decreasing ^{87}Sr/^{86}Sr with increasing [Sr] at depths shallower than 400 mbsf. Site U1466 exhibits a deviation from this trend where [Sr] values remain mostly constant (∼150 μM) while ^{87}Sr/^{86}Sr values decrease from ∼0.70915 to ∼0.70903, in contrast to Site U1468 where ^{87}Sr/^{86}Sr values decrease by only about half as much during the plateau in [Sr] between ∼30 to 150 mbsf. At greater depths (Site U1468 only),

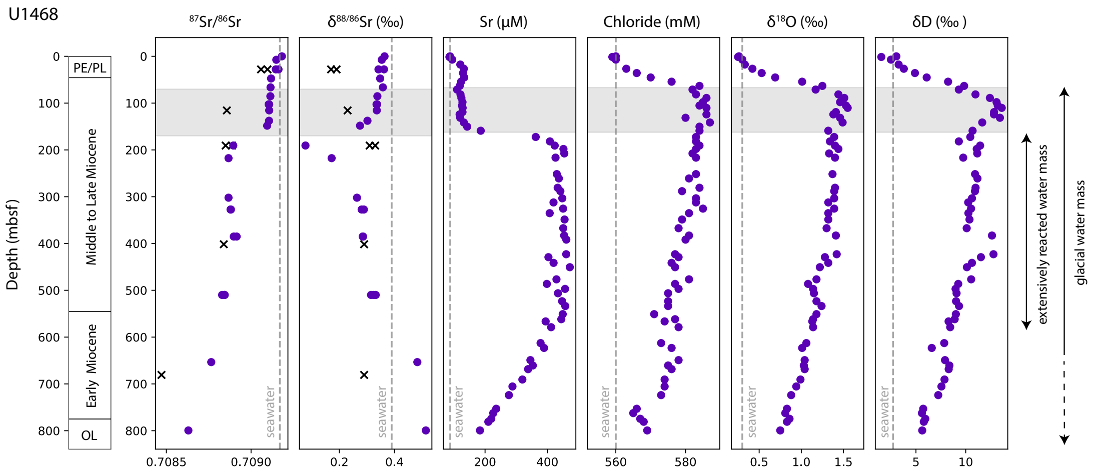

Figure 3.2: Site U1468 pore fluid profiles of ^{87}Sr/^{86}Sr and $\delta^{88/86}$Sr measured in this study, with published [Sr], chloride concentrations, δ^{18}O, and δD profiles (Blättler et al., 2019). Bulk carbonate values at select depths are plotted as black "x" symbols. The best-preserved glacial interval (70 to 170 mbsf) is indicated by the shaded region and is defined based on the conservative tracers (chloride, δ^{18}O, δD) and [Sr] as in Blättler et al. (2019). Modern seawater compositions are shown by the dashed vertical lines.

the negative relationship between [Sr] and ^{87}Sr/^{86}Sr is reversed, with [Sr] decreasing while ^{87}Sr/^{86}Sr values continue to decrease. In [Sr] versus $\delta^{88/86}$Sr space, $\delta^{88/86}$Sr values also generally decrease with increasing [Sr] in the shallower depths sampled at both sites (0 to 400 mbsf), with similar structures to the ^{87}Sr/^{86}Sr vs. [Sr] plots around the 130–150 μM [Sr] plateau. At both sites, $\delta^{88/86}$Sr values reach a minimum around 400 μM [Sr], shifting back to higher values as [Sr] increases in deeper samples (~200 mbsf). Below ~400 mbsf (Site U1468 only), the relationship between $\delta^{88/86}$Sr and [Sr] is again negative, but shifted to significantly higher $\delta^{88/86}$Sr values above even that for modern seawater.

3.4.2 Bulk carbonate $\delta^{88/86}$Sr and ^{87}Sr/^{86}Sr

Bulk carbonate measurements at Site U1468 yielded $\delta^{88/86}$Sr and ^{87}Sr/^{86}Sr values of 0.17 to 0.33‰ and 0.708471 to 0.709097, respectively (Figure 3.2). The Pleistocene/Pliocene carbonate sediments in the upper part of the core (<50 mbsf) are characterized by more radiogenic ^{87}Sr/^{86}Sr (0.709078) compared to the deeper Miocene sediments as expected based on the global seawater ^{87}Sr/^{86}Sr curve (McArthur et al., 2012). Carbonate

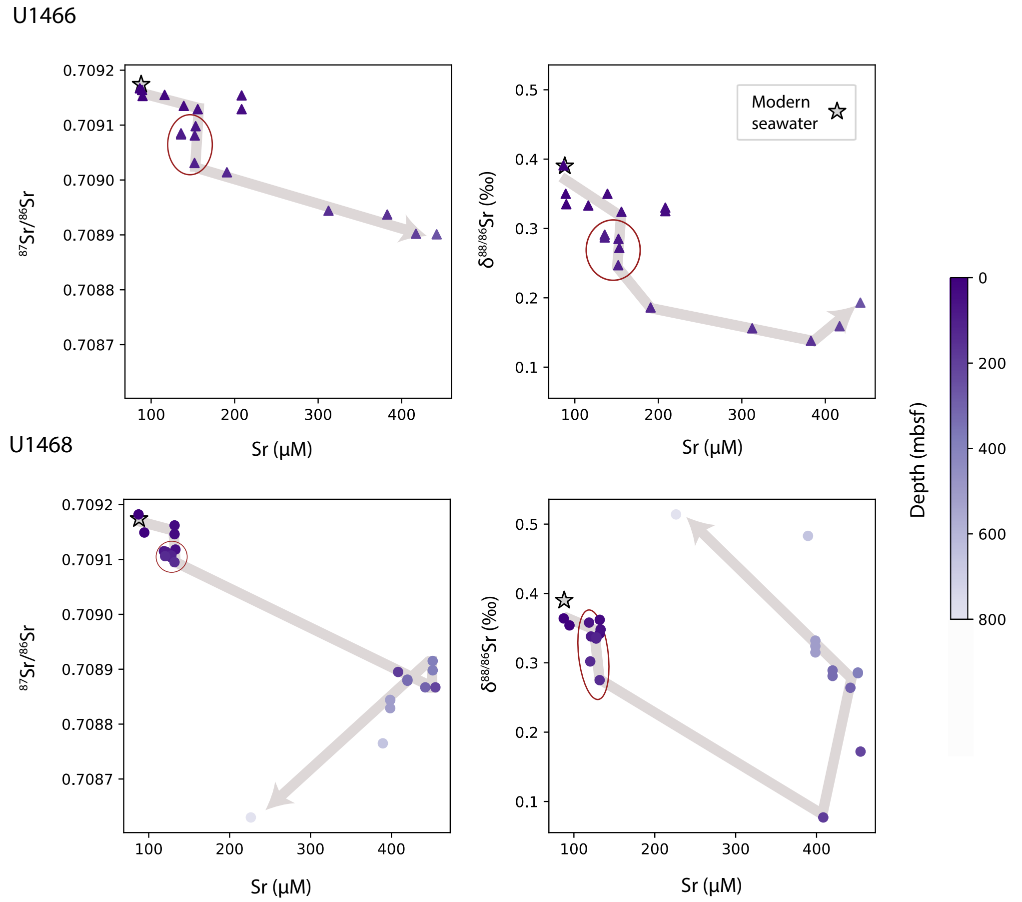

Figure 3.3: Crossplots of pore fluid $^{87}Sr/^{86}Sr$ and $\delta^{88/86}Sr$ versus [Sr] at Site U1466 (*top*) and U1468 (*bottom*). Gray arrows provide a visual guide for changes with depth. Red outlines indicate samples that fall within the best-preserved glacial depth intervals defined by conservative tracers as described in the text and by Blättler et al. (2019).

$^{87}Sr/^{86}Sr$ values between 100 and 400 mbsf range from 0.708839 to 0.708888 (∼10–12 Ma, McArthur and Howarth (2020)), while the deepest carbonate sample at 680 mbsf has the least radiogenic $^{87}Sr/^{86}Sr$ value of 0.708471 (∼19.6 Ma, McArthur and Howarth (2020)). The lowest carbonate $\delta^{88/86}Sr$ is 0.18‰ in the Pleistocene/Pliocene sediments, generally consistent with the 0.15 to 0.21‰ range estimated for marine carbonates (Krabbenhöft et al., 2010; Pearce et al., 2015). The late Miocene carbonate sample at 115.6 mbsf has a $\delta^{88/86}Sr$ value of 0.23‰, with higher $\delta^{88/86}Sr$ values in the older, deeper sediments (0.29 to 0.33‰).

3.5 Discussion

3.5.1 Alteration of remnant glacial seawater

Our ^{87}Sr/^{86}Sr measurements show that the pore fluids in the intervals defined as best-preserved glacial seawater which were expected to record glacial seawater $\delta^{88/86}$Sr have experienced enough alteration to influence the pore fluid radiogenic Sr isotopes. Pore fluid ^{87}Sr/^{86}Sr provides a key constraint on recrystallization at these sites because the ^{87}Sr/^{86}Sr of the glacial ocean is known to be within analytical error of the modern value (Henderson et al., 1994; Mokadem et al., 2015). Reconstructed from measurements of glacial-age planktonic foraminifera, the average glacial seawater ^{87}Sr/^{86}Sr was 0.7091784 ± 0.0000035, compared to the average modern seawater value of 0.7091792 ± 0.0000021 obtained by sampling the major oceans (Atlantic, Pacific, Indian, and the Labrador Sea) (Mokadem et al., 2015). Within the best-preserved glacial pore fluid interval at Site U1468 (70–170 mbsf), the shift in pore fluid ^{87}Sr/^{86}Sr values away from the expected seawater composition indicates that both [Sr] and the Sr isotopic composition of the pore fluids in this depth range have been measurably influenced by carbonate recrystallization (Figure 3.2). The glacial pore fluids at Site U1466 (70–110 mbsf) appear even more altered, as ^{87}Sr/^{86}Sr values decrease rapidly with depth (Figure 3.1). Since seawater ^{87}Sr/^{86}Sr during the LGM was indistinguishable (within analytical error) from the modern ocean composition, sediment-pore fluid interaction is required to explain the pore fluid ^{87}Sr/^{86}Sr profiles.

Alteration of the best-preserved glacial pore fluids by carbonate recrystallization is consistent with the pore fluid $\delta^{44/40}$Ca profiles published by Blättler et al. (2019), which decrease to values lower than the modern seawater composition within the depth interval of the best-preserved glacial seawater. Lower $\delta^{44/40}$Ca values are indicative of carbonate recrystallization, supporting the interpretation that Sr has been added to the best-preserved glacial pore fluids by diagenesis. This result does not rule out the possibility that there may be true differences in LGM seawater [Sr] or $\delta^{88/86}$Sr compared to modern, but does confirm that the higher [Sr] in the best-preserved glacial pore fluid compared to modern seawater is at least partially due to the contributions from carbonate recrystallization, which will also impact pore fluid $\delta^{88/86}$Sr. Thus, neither of these tracers in the Maldives pore fluids can be defined as representing unaltered glacial seawater values but must instead be corrected for the effect of carbonate recrystallization, which will impact Sr but will not have an effect on conservative tracers.

3.5.2 Estimating glacial seawater [Sr] and $\delta^{88/86}$Sr

Mass balance of carbonate input to pore fluids

We used our pore fluid and bulk carbonate ^{87}Sr/^{86}Sr measurements to constrain the contribution of Sr from the sediments to the best-preserved glacial pore fluids. Since the ^{87}Sr/^{86}Sr of the glacial ocean is known, the recrystallized carbonate input to the glacial water mass can be determined by mass balance, which can then be used to calculate the $\delta^{88/86}$Sr of the remnant LGM seawater. As a first approximation we assumed that the measured pore fluid [Sr] and isotopic composition resulted from the addition of recrystallized input from surrounding carbonates to the glacial seawater end-member with negligible diffusion. We neglect the potential for diffusive mixing of the fluid end-members in the system (Holocene water, best-preserved glacial water, and highly altered pore fluid) and treat the best-preserved glacial interval as an isolated water mass altered only by reaction with the surrounding sediments. Based on the sharp transitions in some of the pore fluid Sr and $\delta^{44/40}$Ca profiles, we expect that vertical diffusive mixing was minimized by stratigraphic permeability barriers (Blättler et al., 2019). We recognize the uncertainty of potential upstream reactions with sediments along the advective flow path which could have different mineralogy, [Sr], age, and ^{87}Sr/^{86}Sr than the carbonate sediments recovered in the cores, so we use the core sediment composition as a starting point, but also perform calculations across a range of possible carbonate ^{87}Sr/^{86}Sr values.

Mass balance of the glacial seawater and recrystallized carbonate end member contributions to the pore fluid is described by:

$$[Sr]_{pf} * V_{pf} = [Sr]_{gsw} * V_{pf} + m_x \tag{3.1}$$

where V_{pf} is the pore fluid unit volume (V_{pf} = 1 L). The pore fluid Sr concentration ($[Sr]_{pf}$) is known, while the concentration of glacial seawater Sr ($[Sr]_{gsw}$) and the mass of Sr added by carbonate recrystallization (m_x) are unknown variables.

We solved for $[Sr]_{gsw}$ and m_x using the additional constraint of the radiogenic Sr isotopic mass balance:

$$[Sr]_{pf} * V_{pf} * F_{pf} = [Sr]_{gsw} * V_{pf} * F_{gsw} + m_x * F_x \tag{3.2}$$

The fractional isotopic abundance ($F = {}^{87}\mathrm{Sr}/{}^{86}\mathrm{Sr}$ / (1 + ${}^{87}\mathrm{Sr}/{}^{86}\mathrm{Sr}$)) of glacial seawater ($F_{gsw}$) is constrained by the reconstructed glacial seawater ${}^{87}\mathrm{Sr}/{}^{86}\mathrm{Sr}$ value (0.7091784, Mokadem et al. (2015)). We determined the pore fluid fractional isotopic abundance (F_{pf}) from our measurements of pore fluid ${}^{87}\mathrm{Sr}/{}^{86}\mathrm{Sr}$ and we used our carbonate ${}^{87}\mathrm{Sr}/{}^{86}\mathrm{Sr}$ measurements to constrain the recrystallized input composition (F_x), assuming that all recrystallization adds Sr to pore fluids and is represented by the m_x term (that is, there is negligible Sr isotopic exchange). First, we assumed that the measured ${}^{87}\mathrm{Sr}/{}^{86}\mathrm{Sr}$ of the bulk carbonate in the surrounding core sediment is representative of the recrystallized input ${}^{87}\mathrm{Sr}/{}^{86}\mathrm{Sr}$. We solved Equations 3.1 and 3.2 for each pore fluid sample within the best-preserved glacial intervals at both sites (11 samples total including two procedural replicates) using the composition of the carbonate sediments within the best-preserved glacial interval (Late Miocene-age, ${}^{87}\mathrm{Sr}/{}^{86}\mathrm{Sr} = 0.708857$, $F_x = 0.414814$) (Table 3.3). We then evaluated the uncertainty associated with this assumption (e.g., the possibility of upstream reactions with sediments of a different age and ${}^{87}\mathrm{Sr}/{}^{86}\mathrm{Sr}$) by solving for $[Sr]_{gsw}$ and m_x as a function of F_x, allowing the assumed recrystallized input ${}^{87}\mathrm{Sr}/{}^{86}\mathrm{Sr}$ to vary within the range measured for the Pleistocene (0.709097) to Early Miocene (0.708471) bulk carbonates (Figure 3.4).

For a value of F_x equal to the surrounding Late Miocene carbonate composition, we found that recrystallized input contributed 24–70 μmol Sr (20–46% of the pore fluid unit volume Sr) (Table 3.3, Figure 3.4A). The recrystallized input requires dissolution of only a very small mass of aragonite sediment (<1 g). While this minimal degree of recrystallization is sufficient to alter [Sr] and the Sr isotopic composition of the pore fluids, the effect on the carbonate Sr composition would be negligible given the much greater Sr content of aragonite compared to seawater. For lower values of recrystallized input ${}^{87}\mathrm{Sr}/{}^{86}\mathrm{Sr}$, representing possible upstream reactions with older carbonate sediments with lower ${}^{87}\mathrm{Sr}/{}^{86}\mathrm{Sr}$ values, the recrystallized contribution is smaller (as low as 11–32 μmol for recrystallized input with Early Miocene bulk carbonate ${}^{87}\mathrm{Sr}/{}^{86}\mathrm{Sr} = 0.708471$). Increased recrystallization would be required if the pore fluids reacted with Pleistocene/Pliocene carbonate sediments with ${}^{87}\mathrm{Sr}/{}^{86}\mathrm{Sr}$ more similar to seawater (Figure 3.4A); this scenario may be more likely given decreased reactivity of carbonate sediments with increasing age

Table 3.3: Mass balance solutions for the recrystallized Sr mass added to the pore fluids (m_x) and glacial seawater Sr concentration ($[Sr]_{gsw}$) assuming a recrystallized input ^{87}Sr/^{86}Sr value equal to the composition of the surrounding Late Miocene carbonate sediments (0.708857). Asterisks indicate preparation replicate samples.

Site	**Depth (mbsf)**	**[Sr]$_{pf}$ (μM)**	**F$_{pf}$**	**m$_x$ (μmol)**	**Recrystallized contribution (%)**	**[Sr]$_{gsw}$ (μM)**
U1466	67.9	153	0.414896	38	25	115
U1466	76.9	152	0.414890	46	30	106
U1466	92.6	136	0.414892	39	29	96
U1466	92.6*	136	0.414891	40	30	95
U1466	106.4	152	0.414873	70	46	82
U1468	85.3	121	0.414902	24	20	97
U1468	102.65	127	0.414898	30	23	98
U1468	102.65*	127	0.414899	28	22	99
U1468	115.5	128	0.414899	28	22	100
U1468	137.7	120	0.414899	27	23	93
U1468	148.2	132	0.414895	34	26	98

(Richter & DePaolo, 1988) but the majority of the sediments at these sites are Miocene-age with Pleistocene/Pliocene carbonate sediments limited to the upper ~50–70 meters. We attribute the variability in our solutions for any given F_x to distinct reactive histories for each pore fluid sample. The pore fluid profiles for these sites demonstrate complex variation both laterally and with depth over relatively short spatial scales (Blättler et al., 2019). Therefore the composition of the recrystallized input may vary between the two sites and between pore fluid samples within a given depth range at the same site.

Assuming recrystallized input only from the surrounding sediments (^{87}Sr/^{86}Sr = 0.708857, carbonate age ~11 Ma), our solutions give a mean Sr concentration of glacial seawater of 98±5 μM (95% CI) (Figure 3.4B). This best estimate is ~10% higher than the modern seawater [Sr] and aligns with Paytan et al.'s (2021) calculated change in Pleistocene seawater (up to 25% higher than the modern concentration of 88 μM). For lower values of recrystallized input ^{87}Sr/^{86}Sr, the predicted glacial seawater [Sr] increases up to an average of 118±5 μM (recrystallized input ^{87}Sr/^{86}Sr = 0.708471, carbonate age ~20 Ma). Interaction with sediments younger than ~8 Ma (recrystallized input ^{87}Sr/^{86}Sr $>$ 0.70893) produces average glacial seawater [Sr] solutions similar to or lower than the modern ocean [Sr]. In summary, the hypothesis that the glacial ocean had a higher Sr

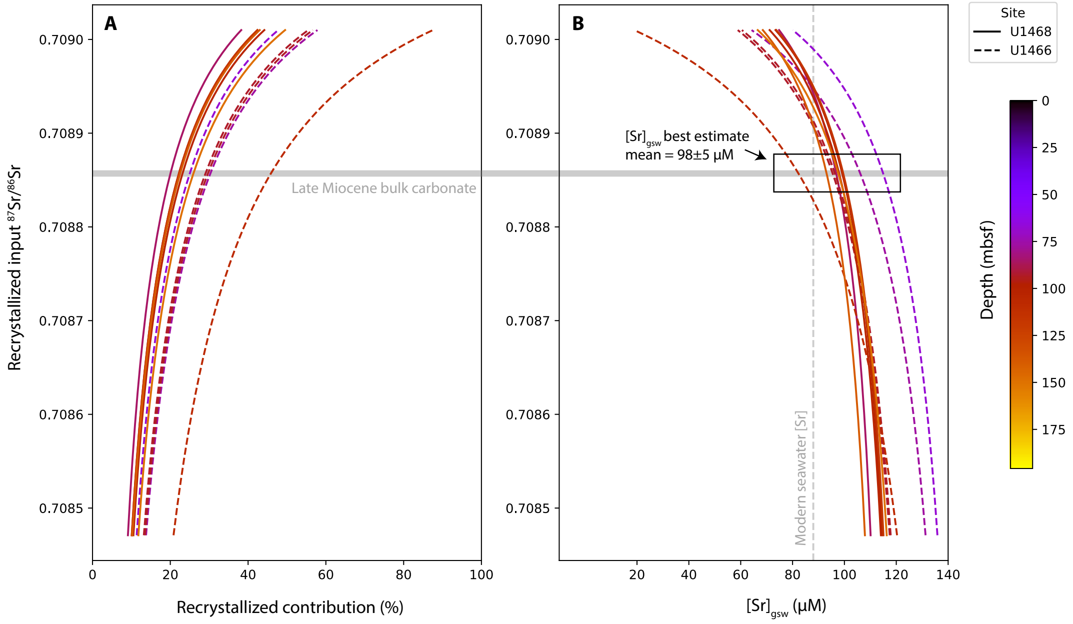

Figure 3.4: Mass balance solutions for (**A**) the recrystallized Sr contribution to the pore fluids and (**B**) glacial seawater Sr concentration ($[Sr]_{gsw}$) as a function of the recrystallized input ^{87}Sr/^{86}Sr (F_x) as described in Section 3.5.2. For a given value of F_x (*y-axis*), Equations 3.1 and 3.2 are solved simultaneously to yield the percent contribution from recrystallization and $[Sr]_{gsw}$ (*x-axes*). Continuous solutions for each pore fluid sample across the range of possible F_x values are shown by solid (Site U1468) and dashed (Site U1466) lines with colors indicating sample depth in the core. Discrete solutions computed assuming recrystallized input ^{87}Sr/^{86}Sr equal to the composition of the surrounding Late Miocene carbonate sediments (0.708857, shown with horizontal gray line) are also displayed in Table 3.3.

inventory than the modern ocean is supported for cases where the recrystallized input ^{87}Sr/^{86}Sr is less than ∼0.70893, corresponding to recrystallizing sediment ages older than ∼8 Ma. Given that the Maldives carbonate platform sediments are mainly Miocene, with younger drift deposits only in the upper ∼50–70 m at Sites U1466 and U1468 (Betzler et al., 2017, 2018), the glacial pore fluids likely interacted with the older (>8 Ma) sediments, though the flow patterns for this system remain speculative (Blättler et al., 2019) and exchange rates decrease as carbonate sediments age (Richter & DePaolo, 1988).

Stable Sr isotopic mass balance

We used the F_x-dependent solutions for m_x and $[Sr]_{gsw}$ to solve the stable Sr isotopic mass balance (Equation 3.3) and estimate glacial seawater $\delta^{88/86}$Sr (δ_{gsw}).

$$[Sr]_{pf} * V_{pf} * \delta_{pf} = [Sr]_{gsw} * V_{pf} * \delta_{gsw} + m_x * \delta_x \tag{3.3}$$

The $\delta^{88/86}$Sr of the pore fluids (δ_{pf}) is known from our measurements. As before, we took the composition of the surrounding Late Miocene carbonates ($\delta^{88/86}$Sr = 0.23‰, ^{87}Sr/^{86}Sr = 0.708857) to be representative of the recrystallized input composition (δ_x, F_x) while also solving across a range of δ_x values to evaluate the sensitivity of our δ_{gsw} solutions to this assumption (Figure 3.5). We chose values of δ_x based on the low end of the range of modern carbonate $\delta^{88/86}$Sr (0.15‰) and the highest carbonate $\delta^{88/86}$Sr we measured at Site U1468 (0.33‰). We again assume that all recrystallization adds Sr to pore fluids and is represented by the m_x term, with negligible Sr isotope exchange.

The resulting glacial seawater $\delta^{88/86}$Sr solutions given δ_x = 0.23‰ and F_x = 0.708857 have a mean of 0.32±0.02‰ (95% CI), significantly lower than the modern ocean value of 0.39‰. This finding of lower glacial $\delta^{88/86}$Sr holds across the range of δ_x values assumed, except for the lowest value of 0.15‰ which results in estimated glacial seawater $\delta^{88/86}$Sr values equal to the modern value for some samples. We conclude that for the majority of reasonable scenarios capturing variability in δ_x, the estimated glacial seawater $\delta^{88/86}$Sr is lower than the modern value, corresponding to a higher-than-modern Sr inventory. In the simplest case where the recrystallized input is isotopically similar to the carbonate presently surrounding the pore fluids, we find that glacial seawater [Sr] = 98±5 μM and $\delta^{88/86}$Sr = 0.32±0.02‰. The effect of Sr isotopic exchange would be to shift pore fluid $\delta^{88/86}$Sr to higher values, as secondary calcite precipitation has been observed to preferentially incorporate isotopically light Sr so that progressive recrystallization leads to increasingly more ^{88}Sr-enriched pore fluids (Voigt et al., 2015). This effect requires that the fractionation between pore fluids and secondary calcite is greater than the offset between dissolving carbonates and pore fluids. In the case of such isotope exchange, the true glacial seawater $\delta^{88/86}$Sr value would be lower than the value we estimate.

Assuming a closed system where glacial seawater represents a combination of interglacial

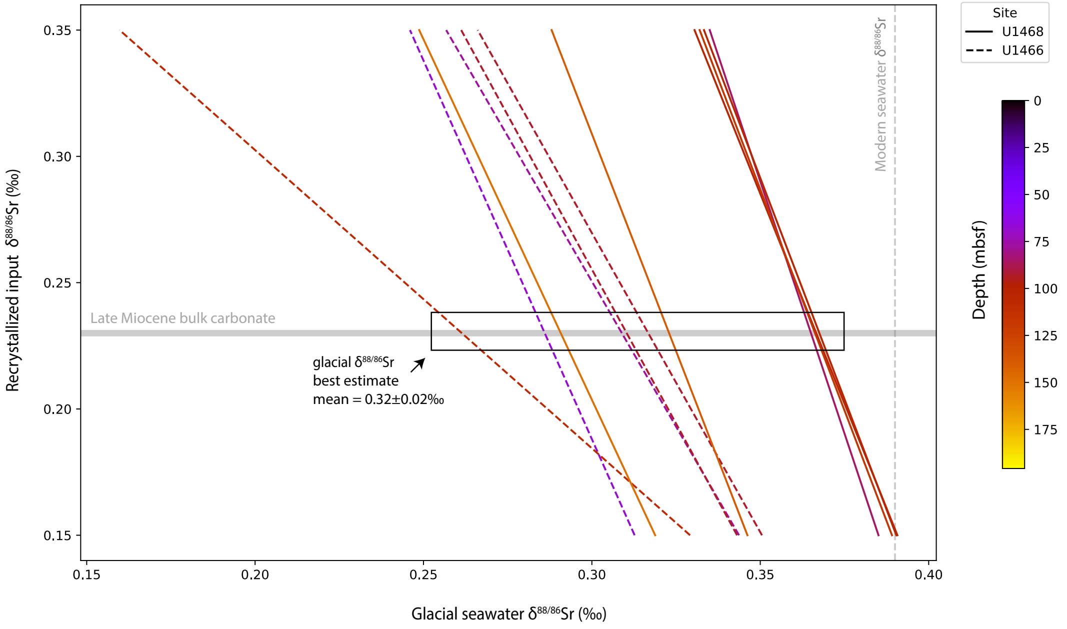

Figure 3.5: Mass balance solutions for glacial seawater $\delta^{88/86}$Sr (δ_{gsw}) calculated using Equation 3.3. Continuous solutions for each pore fluid sample across the range of possible recrystallized input $\delta^{88/86}$Sr (δ_x) values are shown by solid (Site U1468) and dashed (Site U1466) lines with colors indicating sample depth in the core. All solutions assume a recrystallized input ^{87}Sr/^{86}Sr (F_x) value equal to the ^{87}Sr/^{86}Sr of the surrounding carbonates (0.708857) as described in Section 3.5.2. The $\delta^{88/86}$Sr of the surrounding Late Miocene carbonates (0.23‰) is indicated by the gray horizontal line.

seawater and recrystallized input from the shelf carbonate reservoir (0.2‰), our estimated ∼10% increase in glacial seawater [Sr] predicts a seawater $\delta^{88/86}$Sr decrease of ∼0.02‰. The uppermost U1468 pore fluid solutions are close to 0.37‰ and the least altered of the pore fluids analyzed, suggesting that these samples might best reflect the remnant glacial seawater chemistry. The ∼0.07‰ decrease suggested by the mean pore fluid solution requires a greater [Sr] increase (∼30%) for this ocean mass balance, somewhat greater than the 25% increase calculated by Paytan et al. (2021). Additional constraints on either glacial seawater [Sr] or $\delta^{88/86}$Sr would allow further assessment of the preservation of the seawater Sr signal.

Implications for glacial carbon cycling

Lower glacial seawater $\delta^{88/86}$Sr and higher [Sr] relative to today is expected to result from recrystallization of shallow marine carbonate exposed by sea level fall during glacial periods (Krabbenhöft et al., 2010; Paytan et al., 2021; Pearce et al., 2015; Stoll & Schrag, 1998). During the interglacial period, the re-flooding of the continental shelves cut off this Sr source while simultaneously increasing the depositional area available for shallow marine calcifiers and reef builders, which preferentially removed light Sr from the ocean reservoir and increased seawater $\delta^{88/86}$Sr to the modern value. The recycling of Sr between the shelf and seawater over glacial/interglacial cycles is tied to the longstanding "coral reef hypothesis" that describes the implications of shelf-basin partitioning of carbonate for the glacial/interglacial carbon cycle and atmospheric carbon dioxide (Berger, 1982; Opdyke & Walker, 1992; Stoll & Schrag, 1998; Walker & Opdyke, 1995). Reconstructions of deep sea carbonate burial over the last glacial cycle reveal little difference between Holocene and LGM burial rates (Cartapanis et al., 2018; Hayes et al., 2021; M. Wood et al., 2023), implying that the addition of alkalinity from exposed continental shelves was not compensated by lysocline deepening but instead caused excess alkalinity to temporarily build up in the global ocean during glacial periods.

While not definitive, our direct measurements of the contribution of preserved glacial seawater to the Maldives pore fluids suggest that the glacial carbonate weathering flux from the shelf was sufficiently large to drive a change in the ocean Sr inventory and $\delta^{88/86}$Sr despite the relatively long residence time of Sr calculated for the long-term steady state ($\sim$2 Myr). This finding adds to the accumulating evidence that seawater $\delta^{88/86}$Sr and [Sr] may have fluctuated on short (100-kyr) timescales during the Pleistocene (Krabbenhöft et al., 2010; Paytan et al., 2021; Pearce et al., 2015; Stoll & Schrag, 1998) and suggests that a high-resolution reconstruction of seawater $\delta^{88/86}$Sr may help constrain glacial/interglacial changes in shelf carbonate burial and recrystallization (and resulting change in global carbon and alkalinity inventories), which to this point remain difficult to quantify from observations.

3.5.3 Diagenetic processes impacting pore fluid $\delta^{88/86}$Sr

While the primary objective of this study was to reconstruct LGM seawater $\delta^{88/86}$Sr from the Maldives pore fluids by quantifying and subtracting away the impact of carbonate diagenesis, our data set also provides an opportunity to examine the processes that impact pore fluid Sr in shallow carbonate platform systems.

The ^{87}Sr/^{86}Sr profiles for both Site U1466 and Site U1468 indicate that carbonate recrystallization has altered pore fluids at all depths; progressive recrystallization of older (mainly Miocene) carbonates with depth led to decreasing pore fluid ^{87}Sr/^{86}Sr values relative to the modern seawater composition (Figures 3.1 and 3.2). Because secondary carbonate incorporates less Sr than the primary phase, pore fluid [Sr] increases with progressive recrystallization; this effect is greatest for aragonite recrystallization, since aragonite incorporates ~10 times more Sr than calcite, although biogenic calcite also incorporates more Sr than inorganic forms of calcite (Zhang et al., 2020). Below 400 mbsf at Site U1468, the return towards modern seawater [Sr] despite progressively lower ^{87}Sr/^{86}Sr ratios could have different implications: either these pore fluids represent mixing with Holocene-age waters along with recrystallization of older sediments with lower ^{87}Sr/^{86}Sr, or these pore fluids may be even older than the LGM, possibly from the last interglacial (MIS Stage 5e), which would give them more time to exchange Sr with surrounding Miocene-aged sediments.

The variability of pore fluid $\delta^{88/86}$Sr with depth has a more complex pattern, likely reflecting different dominant processes at different depths. The precipitation of carbonate in seawater preferentially incorporates ^{86}Sr over ^{88}Sr ($\Delta^{88/86}\text{Sr}_{carb-sw} \approx$ -0.18‰) such that upon dissolution, carbonates will release isotopically light Sr to pore fluids. In addition to the reactions that occur during carbonate diagenesis, fractionation of Sr isotopes during precipitation of celestine ($SrSO_4$) may alter pore fluid $\delta^{88/86}$Sr where pore fluids become saturated with respect to $SrSO_4$ ($\Delta^{88/86}\text{Sr}_{SrSO_4-sw} \approx$ -0.4‰). If pore fluids drop below celestine saturation again at greater depths, dissolution of $SrSO_4$ may provide a source of light Sr. We untangle the patterns in pore fluid $\delta^{88/86}$Sr using the context of our [Sr] and ^{87}Sr/^{86}Sr profiles, the mineralogy at these sites, and previously reported mass-dependent Sr isotope fractionation associated with these processes.

Table 3.4: Diagenetic processes and their expected influence on pore fluid Sr concentrations, stable Sr isotopes and calcium isotopes.

Process	**$\delta^{88/86}$Sr fractionation**	**$\delta^{44/40}$Ca fractionation**	**Impact on pore fluid**
Aragonite dissolution	$\Delta_{diss} = 0$	$\Delta_{diss} = 0$	[Sr] increase $\delta^{88/86}$Sr approaches carbonate value $\delta^{44/40}$Ca approaches carbonate value
Calcite dissolution	$\Delta_{diss} = 0$	$\Delta_{diss} = 0$	lesser [Sr] increase $\delta^{88/86}$Sr approaches carbonate value $\delta^{44/40}$Ca approaches carbonate value
Aragonite recrystallization (dissolution + secondary calcite precipitation)	Preferential incorporation of light Sr in secondary carbonate (Voigt et al., 2015) is outweighed by aragonite dissolution effect	$\Delta_{precip} = 0.0 \pm 0.1$ (Fantle & DePaolo, 2007)	[Sr] increase $\delta^{88/86}$Sr approaches carbonate value $\delta^{44/40}$Ca approaches carbonate value
Calcite recrystallization (dissolution + secondary calcite precipitation)	Preferential incorporation of light Sr in secondary carbonate (Voigt et al., 2015) dominates dissolution effect	$\Delta_{precip} = 0.0 \pm 0.1$ (Fantle & DePaolo, 2007)	lesser [Sr] increase $\delta^{88/86}$Sr increase $\delta^{44/40}$Ca approaches carbonate value
Celestine precipitation	$\Delta_{precip} = \sim$-0.4 (Widanagamage et al., 2014)	n.a.	[Sr] decrease (just to maintain saturation) $\delta^{88/86}$Sr increase

Site U1468 pore fluid $\delta^{88/86}$Sr

We identify four distinct intervals in the $\delta^{88/86}$Sr profile at Site U1468. In the upper 200 m, pore fluid $\delta^{88/86}$Sr decreases, approaching the value of the surrounding carbonates (Figure 3.6). This trend follows the behavior of the pore fluid ^{87}Sr/^{86}Sr, which has shifted away from the seawater composition toward the composition of the bulk carbonate due to recrystallization. The experimentally determined equilibrium Sr isotope fractionation for inorganic calcite is very close to zero ($\Delta^{88/86}\text{Sr}_{eq(carb-aq)}$ = -0.01±0.06‰), suggesting that carbonate recrystallization will not measurably fractionate Sr isotopes and therefore the pore fluid $\delta^{88/86}$Sr should follow ^{87}Sr/^{86}Sr and approach the carbonate $\delta^{88/86}$Sr composition as recrystallization proceeds (Böhm et al., 2012). Previous work has shown this to be the case for calcium isotopes ($\Delta^{44/40}\text{Ca}_{eq(carb-aq)} \approx 0$‰) (Fantle & DePaolo, 2007; Jacobson & Holmden, 2008), and Sr is expected to behave similarly at low precipitation rates. However, Voigt et al. (2015) documented isotopically heavy $\delta^{88/86}$Sr values in deep sea carbonate sediments that were explained by fractionation during recrystallization, where secondary calcite preferentially incorporated light Sr. Consequently, we suggest that the approach of pore fluid $\delta^{88/86}$Sr toward carbonate $\delta^{88/86}$Sr within the 0–200 mbsf interval may instead be explained by the effect of aragonite dissolution "out-competing" the effect of secondary calcite precipitation. That is, the dissolution of aragonite has contributed so much isotopically light Sr to the pore fluids that the fractionation during calcite precipitation is insufficient to shift pore fluid $\delta^{88/86}$Sr to heavier values. This scenario may be more common in shallow marine systems where sediments are rich in aragonite, and may not commonly apply to deep sea settings where the fractionation by secondary calcite formation should dominate (Voigt et al., 2015).

At 200 mbsf, pore fluid $\delta^{88/86}$Sr reaches the lightest value observed at both our sites (0.08‰). This $\delta^{88/86}$Sr value is considerably lighter than any of the carbonates measured in this study, as well as most modern carbonates measured in other studies (Böhm et al., 2012; Krabbenhöft et al., 2010; Pearce et al., 2015). Carbonate $\delta^{88/86}$Sr values as low as 0‰ have been measured in culture experiments (Stevenson et al., 2014), but the average marine carbonate sink is ∼0.15 to 0.21‰ and we have no evidence for especially low $\delta^{88/86}$Sr carbonates at this site. We hypothesize that this datum may reflect the dissolution of celestine, which was detected by x-ray diffraction at this site starting around 200 mbsf (Betzler et al., 2017). Celestine precipitates when [Sr] increases sufficiently to reach $SrSO_4$ saturation, dependent on pore fluid sulfate concentrations, with a theoretical equilibrium isotope fractionation ($\Delta^{88/86}\mathrm{Sr}_{\mathrm{SrSO_4}-aq}$) of approximately -0.4‰ (Widanagamage et al., 2014). If celestine precipitated from pore fluids with $\delta^{88/86}\mathrm{Sr} \approx 0.24$‰, its isotopic composition would be close to -0.16‰ and a small amount of dissolution could shift pore fluid $\delta^{88/86}$Sr to 0.08‰.

Between 200–500 mbsf, the increase in pore fluid $\delta^{88/86}$Sr may be explained by multiple processes. The first possibility is that pore fluid $\delta^{88/86}$Sr approached the $\delta^{88/86}$Sr value of the surrounding bulk carbonate ($\Delta^{88/86}\mathrm{Sr}_{eq(carb-aq)} = 0$‰), which is heavier (0.29–0.33‰) compared to the shallower Pleistocene/Pliocene carbonates (0.17–0.23‰). In this case, the lighter values at ∼200 to 220 mbsf could be due to celestine dissolution as discussed above while the rest of the samples in this interval reflect the bulk carbonate composition. Conversely, if carbonate recrystallization instead fractionated Sr isotopes by preferentially precipitating light Sr, the shift toward higher $\delta^{88/86}$Sr could reflect this process. Compared to the decrease in $\delta^{88/86}$Sr above 200 mbsf where we suggest that aragonite dissolution dominated the $\delta^{88/86}$Sr signal, secondary calcite and dolomite formation may have been the dominant process impacting $\delta^{88/86}$Sr in this deeper interval. We favor this explanation, as it is consistent with the continuing trend of increasing $\delta^{88/86}$Sr to values significantly greater than the bulk carbonate composition in the deepest interval (>400 mbsf). This interpretation is also consistent with the carbonate mineralogy at this site, with the proportion of aragonite decreasing in favor of low-Mg calcite and dolomite below ~50 mbsf (Figure 3.6). Additionally, pore fluid ^{87}Sr/^{86}Sr has achieved the same value as the bulk carbonate, [Sr] has reached a maximum, and $\delta^{44/40}$Ca has reached the lowest values within this interval, indicating extensive recrystallization at these depths. Another process, not mutually exclusive, that could increase pore fluid $\delta^{88/86}$Sr is the precipitation of celestine. Given that celestine was detected in sediments throughout this interval, we conclude that $SrSO_4$ precipitation may have additionally contributed to the pore fluid $\delta^{88/86}$Sr changes. While the combined tracers point to carbonate recrystallization as the dominant process in this interval, it is not possible with the data available to deconvolve the contribution of celestine precipitation to the increasing $\delta^{88/86}$Sr values.

Below 500 mbsf, pore fluid $\delta^{88/86}$Sr continues to increase to values greater than both the bulk carbonate and modern seawater values. While the ^{87}Sr/^{86}Sr, [Sr], and $\delta^{44/40}$Ca profiles could indicate mixing with a Holocene water mass penetrating from below, consistent with the interpretations of (Blättler et al., 2019), the $\delta^{88/86}$Sr values greater than modern seawater $\delta^{88/86}$Sr can only be explained by a process that preferentially removes light Sr isotopes from pore fluids. We take these data as evidence for fractionation during carbonate recrystallization, as previously reported by Voigt et al. (2015). Thus, we conclude that the Site U1468 $\delta^{88/86}$Sr profile is best explained by: 1) aragonite dissolution out-competing the fractionation effect of secondary calcite formation from 0 to 200 mbsf, 2) celestine dissolution driving very light pore fluid $\delta^{88/86}$Sr at 200 mbsf, 3) a combination of secondary calcite formation and celestine precipitation preferentially incorporating light Sr from 200 to 500 mbsf, and 4) extensive secondary calcite formation further increasing pore fluid $\delta^{88/86}$Sr below 500 mbsf (Figure 3.6).

Site U1466 pore fluid $\delta^{88/86}$Sr

At Site U1466, where the profile covers shallower depths than Site U1468, similar carbonate recrystallization processes can explain the $\delta^{88/86}$Sr trends. In the upper section

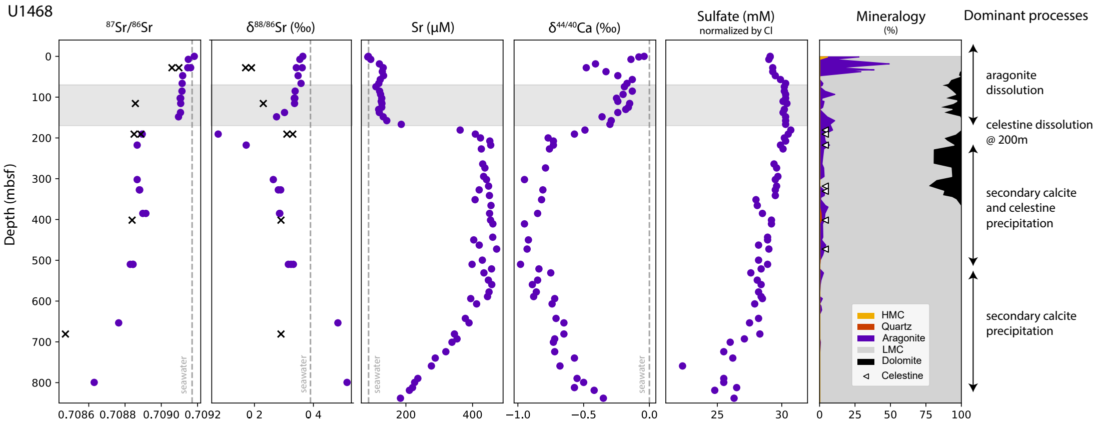

Figure 3.6: Pore fluid profiles of ^{87}Sr/^{86}Sr and $\delta^{88/86}$Sr from this study, with published [Sr], $\delta^{44/40}$Ca, sulfate concentrations, and sediment mineralogy for Site U1468 (Betzler et al., 2017; Blättler et al., 2019). The white triangles on the mineralogy plot indicate the presence of celestine ($SrSO_4$) detected by X-ray diffraction.

of the profile (0 to 160 mbsf), decreasing $\delta^{88/86}$Sr values reflect the dominance of aragonite dissolution on pore fluid $\delta^{88/86}$Sr. Based on our interpretation of the Site U1468 profile, we expect that fractionation of light Sr by secondary calcite precipitation has occurred in this interval but, as in the upper interval at Site U1468, this effect has been overbalanced by the release of light Sr to pore fluids from aragonite dissolution. The lowest $\delta^{88/86}$Sr value at this site is 0.14‰, which is consistent with the range of bulk carbonate $\delta^{88/86}$Sr and does not require a source from a phase with lower $\delta^{88/86}$Sr (e.g., celestine, which was not detected at this site). A switch in the dominant recrystallization process explains the inflection point at 160 mbsf; below this depth the fractionation effect of secondary calcite precipitation is no longer overwhelmed by aragonite dissolution and $\delta^{88/86}$Sr increases with depth (Figure 3.7). This is consistent with the apparent minimum in pore fluid ^{87}Sr/^{86}Sr, high [Sr], and low $\delta^{44/40}$Ca values that are reached by 200 mbsf, indicating extensive recrystallization of carbonate.

The similarities between the Site U1466 and U1468 $\delta^{88/86}$Sr profiles, namely decreasing values with depth to approximately 160 to 200 mbsf before $\delta^{88/86}$Sr increases, underpins our interpretation that the two processes involved in aragonite recrystallization (aragonite dissolution, secondary calcite precipitation) are the primary drivers of these trends. Celestine dissolution/precipitation may have played a secondary role at Site U1468, but

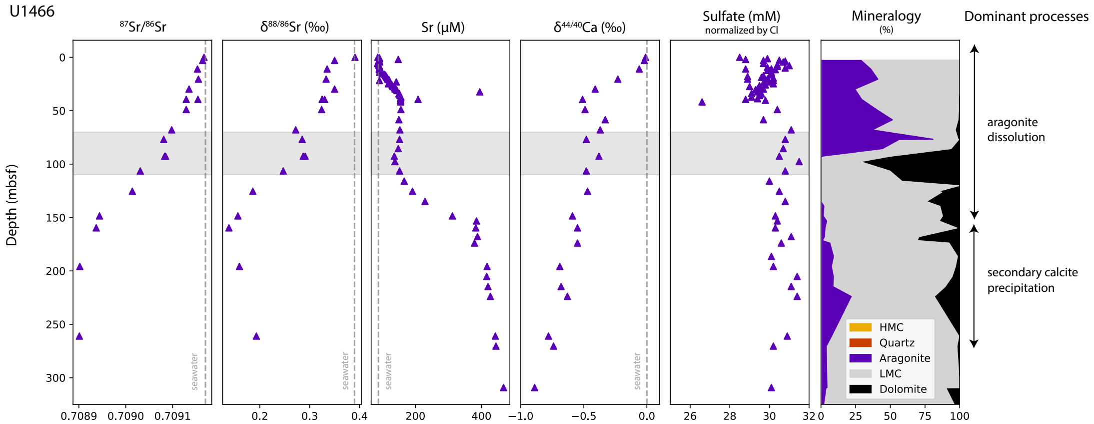

Figure 3.7: Pore fluid profiles of ^{87}Sr/^{86}Sr and $\delta^{88/86}$Sr from this study, with published [Sr], $\delta^{44/40}$Ca, sulfate concentrations, and sediment mineralogy for Site U1466 (Betzler et al., 2017; Blättler et al., 2019).

the increase in $\delta^{88/86}$Sr for the deepest Site U1466 samples in the absence of celestine indicates that another phase must have impacted the stable Sr isotope ratios in the pore fluid. Secondary calcite is the obvious candidate, providing support for the finding of Voigt et al. (2015) that secondary calcite precipitation preferentially incorporates ^{86}Sr over ^{88}Sr leaving the pore fluids enriched in ^{88}Sr. Our results further show that the effect of this fractionation can be obscured by the effect of aragonite dissolution in young sediments, which is particularly relevant in shallow marine systems dominated by aragonite. In contrast to pore fluid calcium isotopes, where fractionation was not detected during secondary calcite precipitation and pore fluids equilibrate with the bulk carbonate $\delta^{44/40}$Ca as recrystallization proceeds, pore fluid $\delta^{88/86}$Sr is sensitive to the balance of aragonite dissolution and secondary calcite precipitation occurring during recrystallization.

3.5.4 Bulk carbonate $\delta^{88/86}$Sr

The bulk carbonate $\delta^{88/86}$Sr values reflect the offset from contemporaneous seawater $\delta^{88/86}$Sr composition due to seawater-carbonate fractionation and potentially the effects of post-depositional processes that could fractionate Sr isotopes. At Site U1468, the Pleistocene/Pliocene carbonate sample (27.9 mbsf) has a $\delta^{88/86}$Sr value consistent with the modern marine carbonate sink (0.15 to 0.21‰) (Krabbenhöft et al., 2010; Pearce et al., 2015). The deeper Miocene carbonates have significantly higher $\delta^{88/86}$Sr values, indicating variation in seawater composition or fractionation processes occurring during or after carbonate precipitation during the Miocene compared to today. Assuming constant fractionation between seawater and carbonate through time ($\Delta^{88/86}\text{Sr}_{carb-sw} \approx$ -0.18‰), the $\delta^{88/86}$Sr values of the carbonate samples between 100 and 680 mbsf imply that early to middle Miocene seawater $\delta^{88/86}$Sr was between 0.47 and 0.51‰, with a decrease to ∼0.41‰ by the late Miocene. These inferred middle to early Miocene seawater values are significantly greater than the range of seawater $\delta^{88/86}$Sr reconstructed by Paytan et al. (2021) for the past 35 million years, and are inconsistent with the reconstructed trend of increasing seawater $\delta^{88/86}$Sr from a minimum of ∼0.33‰ in the middle Miocene to ∼0.36‰ in the late Miocene. The higher-than-expected $\delta^{88/86}$Sr values of the carbonates between 190–680 mbsf may suggest that the seawater-carbonate fractionation factor during the Miocene was smaller than the average fractionation of carbonates in the present day ocean. Alternatively, it is also possible that the primary $\delta^{88/86}$Sr composition of the carbonate has since been diagenetically altered towards higher values. In a closed system, carbonate $\delta^{88/86}$Sr is unlikely to be affected by carbonate diagenesis because carbonates contain much more Sr than pore fluids (Voigt et al., 2015). However, in a more open system with long-lived advection, evolution of pore fluid $\delta^{88/86}$Sr to higher values through secondary calcite precipitation or celestine precipitation could drive recrystallized bulk carbonate towards higher values as well. Both mechanisms underscore the need for caution when interpreting bulk carbonate $\delta^{88/86}$Sr values without fully understanding the potential variability of $\Delta^{88/86}\text{Sr}_{carb-sw}$ or the diagenetic history of the carbonate archive.

3.6 Conclusions

The Maldives pore fluid archive presented a unique opportunity to directly constrain the $\delta^{88/86}$Sr of the glacial ocean in the preserved remnant of LGM seawater at Sites U1466 and U1468. We find that glacial seawater $\delta^{88/86}$Sr was likely lower than today (∼0.32‰) and [Sr] higher (∼98 μM). Our estimate is consistent with the recent proxy record that indicated the average seawater $\delta^{88/86}$Sr during the Late Quaternary was 0.35‰ (Paytan et al., 2021). These findings support the hypothesis that the glacial ocean Sr reservoir was isotopically lighter than that of the modern ocean due to shelf carbonate recrystallization during sea level regression, motivating future study of the response of seawater $\delta^{88/86}$Sr to climate-driven sea level changes on relatively short timescales.

The shallow-marine carbonate platform setting of these Maldives sites and the multiple advected water masses in this system led to complex patterns in pore fluid profiles of reactive tracers including $\delta^{88/86}$Sr. The pore fluid $\delta^{88/86}$Sr profiles are altered by both secondary calcite and celestine precipitation, and indicate that in aragonite-dominated settings the fractionation associated with secondary calcite precipitation may be obscured by the dissolution of aragonite. We show that distinct diagenetic processes dominated at different depth intervals. Trends of increasing pore fluid $\delta^{88/86}$Sr within intermediate core depths suggest that carbonate recrystallization fractionates $\delta^{88/86}$Sr, supporting the conclusion of Voigt et al. (2015) who documented similar trends in deep-sea carbonate sediments. In the shallower pore fluids at the Maldives sites, aragonite dissolution overwhelmed the secondary calcite fractionation effect and caused $\delta^{88/86}$Sr to decrease toward the bulk carbonate composition. Pore fluid $\delta^{88/86}$Sr may also indicate the presence of celestine, which is common in carbonate-rich lithologies where carbonate recrystallization can lead to celestine saturation in pore fluids (Hoareau et al., 2010). In particular, our data show that the dissolution of celestine can drive pore fluid $\delta^{88/86}$Sr to very low values that cannot be explained by dissolution of carbonate. Since celestine formation can control pore fluid [Sr], diagenetic studies must take this into account and analysis of pore fluid $\delta^{88/86}$Sr can provide an additional means of detection.

The addition of $\delta^{88/86}$Sr to the suite of tracers measured in the Maldives pore fluids allows us to differentiate processes by the fingerprint of mass-dependent fractionation, bringing new insight to the reactive histories of the distinct water masses present in this system. By documenting pore fluid $\delta^{88/86}$Sr variability in a shallow marine setting for the first time, we suggest that $\delta^{88/86}$Sr can be a useful tracer of diagenetic processes when applied in multi-tracer studies.

3.7 Acknowledgements

This research used samples and data provided by the International Ocean Discovery Program (IODP). We would like to thank the crew, technical staff, and science party of Expedition 359. This work was supported by an IODP Schlanger Ocean Drilling Fellowship and graduate student research grants from the International Association of Geochemistry and the University of California, Santa Cruz Department of Earth and Planetary Sciences (to MMW).

Chapter 4

Glacial/interglacial variations in seawater stable strontium isotope ratios recorded in marine barite

4.1 Abstract

Paleorecords of seawater stable and radiogenic strontium isotope ratios ($\delta^{88/86}$Sr, ^{87}Sr/^{86}Sr) provide key insight to past changes in continental weathering and the marine carbonate sink. While traditional understanding suggests that the concentration and isotopic composition of Sr in seawater evolve slowly over millions of years, more recent studies suggest dynamic behavior on shorter timescales during the Pleistocene attributed to non-steady state weathering processes and sea level-driven changes in shallow marine carbonate burial and recrystallization. This study documents transient changes in seawater $\delta^{88/86}$Sr, which varied from 0.33‰ to 0.42‰ over the past two glacial cycles (0–250 ka), and reveals that seawater $\delta^{88/86}$Sr varied as much over the past 250 kyr as observed for the entire Late Cenozoic. We used a simple model of carbonate burial and recrystallization related to the flooding and exposure of continental shelf area to predict seawater $\delta^{88/86}$Sr responses to glacial/interglacial sea level fluctuations. The model simulations failed to predict the observed $\delta^{88/86}$Sr variations, suggesting a missing factor in our conceptualization of the hypothesized shelf carbonate burial/recrystallization mecha-

nism. We present a refined hypothesis that considers how complex environmental factors and reef platform history might have controlled carbonate fluxes and consequently the cycling of Sr over glacial/interglacial cycles.

4.2 Introduction

The isotopic composition of strontium (Sr) in the ocean traces past changes in continental weathering, hydrothermal activity, and carbonate deposition over Earth history. Radiogenic Sr isotope ratios (^{87}Sr/^{86}Sr) in seawater reflect the mixing of the input fluxes of Sr to the ocean – rivers, groundwater, hydrothermal fluxes, and diagenetic alteration. Stable Sr isotope ratios ($\delta^{88/86}$Sr) are governed by both the inputs of Sr and the carbonate sink due to mass-dependent fractionation between carbonate and seawater. According to the canonical view of conservative elements in the ocean, seawater Sr isotopes evolve in response to long-term changes in the input or output fluxes but will not be significantly altered by short-term perturbations. Consequently, the application of the paired ^{87}Sr/^{86}Sr and $\delta^{88/86}$Sr isotope systems has been limited to multi-million year timescales, with current paleorecords spanning the Late Cenozoic (Paytan et al., 2021), Phanerozoic (Vollstädt et al., 2014), and Precambrian (Wang et al., 2023). The evolution of seawater ^{87}Sr/^{86}Sr constrains long-term changes in the balance of silicate weathering and hydrothermal activity related to plate tectonic processes (McArthur et al., 2012; Veizer, 1989), while seawater $\delta^{88/86}$Sr provides information about global carbonate burial rates, particularly secular changes in the extent of reef deposition (Paytan et al., 2021). Together ^{87}Sr/^{86}Sr and $\delta^{88/86}$Sr measurements have provided critical insight to the interactions between the climate, tectonics, and the carbon cycle over millions of years, but these proxies have generally been considered insensitive to perturbation on timescales shorter than the calculated residence time of Sr ($\sim$2 Myr).

Yet, multiple studies have converged on the idea that the ocean Sr budget may have been dynamic on relatively short timescales during the Pleistocene (0–2.5 Ma). One line of evidence comes from the mismatch between the observed long-term increase of seawater ^{87}Sr/^{86}Sr (0.000054 Myr^{-1}) and modern hydrothermal and riverine flux estimates (Vance et al., 2009). To match the long-term evolution of seawater ^{87}Sr/^{86}Sr, an unrealistically high flux of low-^{87}Sr/^{86}Sr hydrothermal Sr is required to balance the observed modern riverine flux (Davis et al., 2003; Vance et al., 2009). Vance et al. (2009) proposed that the modern riverine flux is higher than the average Quaternary riverine flux due to non-steady state weathering processes, with chemical weathering of freshly-ground sediments producing a post-glacial pulse of silicate weathering that has not yet decayed away. While fluctuations in seawater ^{87}Sr/^{86}Sr are not observed over glacial/interglacial cycles, the paleorecords can accommodate a ±12–15% silicate weathering increase within the analytical uncertainty (Mokadem et al., 2015).

Characterization of the $\delta^{88/86}$Sr values of modern Sr fluxes has further demonstrated that the inputs and outputs are presently not at isotopic steady state (Krabbenhöft et al., 2010; Pearce et al., 2015). The offset between the modern input of Sr ($\delta^{88/86}$Sr = 0.31–0.32‰) and the carbonate sink ($\delta^{88/86}$Sr = 0.15–0.21‰) cannot be explained by the post-glacial silicate weathering peak alone and indicates that an additional source of isotopically-light Sr would be required for the Sr budget to attain isotopic equilibrium (Krabbenhöft et al., 2010). A potential source of this additional Sr flux is carbonate weathering of continental shelves exposed by sea level fall, which would supply low-$\delta^{88/86}$Sr Sr and could balance the Sr budget during glacial periods. Aragonite, the dominant polymorph of carbonate in the shallow ocean, recrystallizes to calcite during meteoric diagenesis and releases Sr to seawater (Schlanger, 1988; Stoll & Schrag, 1998). Since observational constraints suggest that glacial deep-sea carbonate fluxes were similar to the Holocene (Cartapanis et al., 2018; Hayes et al., 2021; M. Wood et al., 2023) and aragonite contains ∼10 times more Sr than calcite, the excess Sr input from exposed shelves would have accumulated in seawater rather than have been compensated by calcite burial in the deep ocean. Consequently, seawater $\delta^{88/86}$Sr and [Sr] are expected to have been lower and higher, respectively, during glacial sea level low stands (Krabbenhöft et al., 2010; Stoll & Schrag, 1998). When post-glacial sea level rise flooded the continental shelves, the Sr budget was perturbed as the the aragonite recrystallization flux was cut off and the area available for shallow (neritic) carbonate burial increased. Higher rates of aragonite burial lowered seawater [Sr] while carbonate-seawater fractionation caused seawater $\delta^{88/86}$Sr values to increase. Glacial/interglacial sea level fluctuations may have repeatedly caused large additions and removals of Sr via the shelf carbonate burial/recrystallization mechanism, driving changes in seawater $\delta^{88/86}$Sr over 10–100 kyr as Sr was recycled between the shelf carbonate reservoir and the ocean.

Paleorecords of seawater $\delta^{88/86}$Sr also point to a dynamic Pleistocene Sr budget. In Chapter 2, we showed that seawater from the Last Glacial Maximum (LGM) preserved within sediment pore fluids in the Maldives Inner Sea had lower $\delta^{88/86}$Sr ($\sim$0.32‰) and higher [Sr] ($\sim$98 μM) than the modern ocean ($\delta^{88/86}$Sr = 0.39‰, [Sr] = 89μM), consistent with recrystallization of shallow marine carbonate exposed by sea level fall during glacial periods. The long-term seawater $\delta^{88/86}$Sr record derived from marine barite by Paytan et al. (2021) varies between $\sim$0.31 and 0.39‰ during the Pleistocene with an average seawater $\delta^{88/86}$Sr value of 0.35‰ for the past 2.5 Myr, hinting at the possibility of high-frequency variations over glacial/interglacial cycles. This long-term record (temporal resolution of $\sim$15–20 kyr) may alias high-frequency variations that could be resolved with a higher-resolution record, which is the aim of this study.

We took a combined observational and modeling approach to determine whether the ocean Sr budget behaved dynamically on glacial/interglacial timescales and to investigate the relationship between sea level and seawater $\delta^{88/86}$Sr. First, we looked to the marine sedimentary record and used marine barite to reconstruct seawater $\delta^{88/86}$Sr and ^{87}Sr/^{86}Sr over the past two glacial cycles (0–250 ka). To provide context for the interpretation of these paleorecords, we modeled the relationship between the ocean Sr budget and sea level with a simple representation of the shallow marine carbonate sink and different sea level histories. By comparing our process-based model of glacial/interglacial Sr cycling to our observations, we illustrate that the relationship between seawater $\delta^{88/86}$Sr and sea level fluctuations is complex and we identify key limitations in our understanding of shallow carbonate burial and recrystallization on glacial timescales.

4.3 Methods

4.3.1 Marine barite separation and screening

Marine barite from sediment cores drilled by U.S. JGOFS Cruise TTN013 (TTN013-PC83, TTN013-PC72) and Cruise Venture 1 (VNTR01-PC8) in the equatorial Pacific was used to reconstruct seawater $\delta^{88/86}$Sr and ^{87}Sr/^{86}Sr from 250 ka to present (Table A.3). Age models for the TTN013 cores are from Murray et al. (2000) with 14C ages from Winckler et al. (2008) for the upper 100 cm of TTN013-PC72. The VNTR01-PC8 age model is from Pisias and Mix (1997). Barite was separated from sediments by a sequential leaching procedure that uses sodium hypochlorite, acetic acid, hydroxylamine, and a mixture of HF and HNO_3 acids to target non-barite sedimentary fractions (Eagle et al., 2003; Paytan et al., 1993). Samples were then checked for purity by scanning electron microscopy and dissolved by chelation with Mitsubishi MCI® Gel-CK08P cation exchange resin (Eagle et al., 2003; Paytan et al., 1993). Approximately 5–10 mg of powdered barite were weighed into Teflon beakers with 1 mL MCI® resin at neutral pH and Milli-Q water (18.2 MΩ). Samples were heated in a 90°C furnace and periodically sonicated until no visible sample remained and the pH of the supernatant no longer decreased. The cations bound to the resin were recovered by washing the resin with 5 mL triple-distilled 6N HCl and 4 mL triple-distilled 2N HNO_3. After collecting the cations, the samples were dried down, reconstituted in 2% HNO_3, and analyzed by ICP-OES and ICP-MS for concentrations of major (Ba, Sr, Ca) and trace elements, respectively. We further screened the samples for contaminating phases using elemental ratios (e.g., Al/Ba, Ti/Ba, Mn/Ba).

4.3.2 Strontium column chromotography

Chromatographic column separation of Sr from barite was performed using Bio-Rad AG®50W-X8 cation exchange resin on 22 cm glass columns with a flow rate of approximately 30 μL/min. Columns were preconditioned with triple-distilled 1.8N HCl before sample aliquots of 1200 ng Sr were loaded onto the resin. The resin was washed with 6 mL 1.8N HCl before Sr was eluted in 6 mL 1.8N HCl. Procedural blanks for the entire sample preparation were less than 1 ng Sr.

4.3.3 Strontium isotope analyses

Strontium isotope measurements were performed at GEOMAR Helmholtz Center for Ocean Research Kiel (Germany) following the DS-TIMS method published by Krabbenhöft et al. (2009). A single measurement requires separate analyses of an ^{87}Sr/^{84}Sr-spiked sample and an unspiked sample, from which the ^{88}Sr/^{86}Sr ratios were calculated by the double spike correction algorithm and reported in delta notation as $\delta^{88/86}$Sr

(‰) = (^{88}Sr/^{86}Sr$_{sample}$/ ^{88}Sr/^{86}Sr$_{SRM987}$ - 1) * 1000. We report the traditional radiogenic Sr isotope value ^{87}Sr/^{86}Sr normalized to a ^{88}Sr/^{86}Sr ratio of 8.375209. The external reproducibility was determined by repeated measurements of the JCp-1 coral standard ($\delta^{88/86}$Sr = 0.19±0.02‰, ^{87}Sr/^{86}Sr = 0.70918±0.00003, n = 9), the IAPSO seawater standard ($\delta^{88/86}$Sr = 0.39±0.02‰, ^{87}Sr/^{86}Sr = 0.709174±0.000007, n = 11), and NIST® SRM® 987 ($\delta^{88/86}$Sr = 0.00±0.02‰, ^{87}Sr/^{86}Sr = 0.710235±0.000009, n = 18).

4.3.4 Modeling

We constructed an ocean box model coupled to a spatially-resolved continental shelf model to predict the response of the ocean Sr inventory and isotopic composition to continental shelf exposure and flooding during glacial/interglacial sea level change. The model, illustrated in Figure 4.1, predicts spatially-resolved changes in aragonite burial and recrystallization on continental shelves as a function of paleotopography and calculates the effect of these variable shelf fluxes on the ocean Sr isotope mass balance. The carbonate sink is represented based on best estimates for carbonate burial fluxes in modern neritic environments (e.g., coral reefs, bays, and carbonate-rich shelves) and carbonate hot spots (O'Mara & Dunne, 2019), with the simplifying assumption that shallow carbonate burial changes through time solely as a function of shelf area within neritic habitat depth ranges. We also incorporated a post-glacial pulse of silicate weathering after Mokadem et al. (2015), allowing non-steady state variations in the riverine flux of <±15% over glacial/interglacial cycles. The model framework, fluxes, and assumptions are detailed in Appendix A. We forced the model with four different sea level histories to evaluate how the extent and timing of continental shelf flooding and exposure impacts the seawater Sr response to sea level change (Table 4.1).

4.4 Results

4.4.1 $\delta^{88/86}$Sr and ^{87}Sr/^{86}Sr records

The marine barite $\delta^{88/86}$Sr record spans the last 250 kyr at approximately 4-kyr resolution (Figure 4.2A). Inferred seawater $\delta^{88/86}$Sr values calculated using an isotope offset of 0.536‰ (Paytan et al., 2021) show significant variability over the last two glacial cycles,

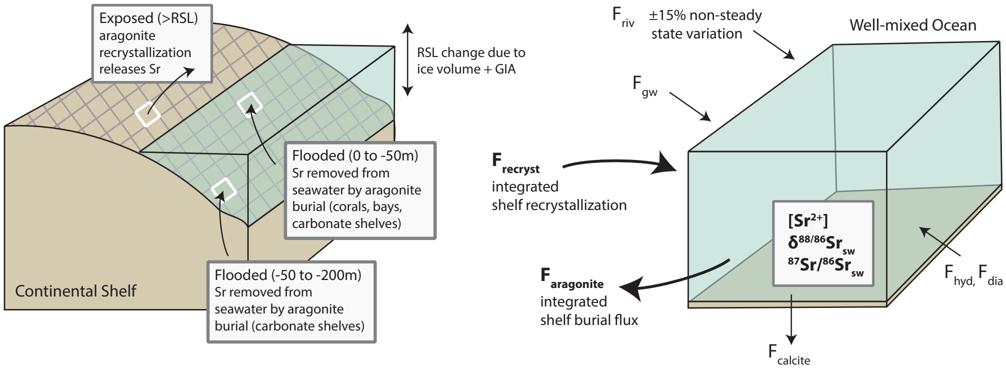

Figure 4.1: Schematic of the coupled continental shelf-ocean box model. Model equations and the fluxes illustrated here are described in detail in Appendix A.

ranging between 0.33 to 0.42‰. Two samples (at 10 and 67 ka) have lower $\delta^{88/86}$Sr values (0.31-0.32‰) but are not consistent with the rest of the data (Figure 4.2A); we consider these to be outliers and ignore these in our discussion but have no reason to exclude them from the dataset. Overall, the range of $\delta^{88/86}$Sr values is about five times the long-term analytical uncertainty (0.02‰) and is similar to the entire range reconstructed for the Late Cenozoic (∼0.3-0.4‰, Paytan et al., 2021).

At 250 ka, seawater $\delta^{88/86}$Sr was similar to the modern ocean (∼0.37–0.38‰). Seawater $\delta^{88/86}$Sr decreased by 0.05‰ between 250 and ∼220 ka before increasing to ∼0.40‰ by 210 ka. These 0.05–0.07‰ changes in $\delta^{88/86}$Sr occurring over 40 kyr span nearly the full range of seawater $\delta^{88/86}$Sr from the past 35 Myr (Paytan et al., 2021). The $\delta^{88/86}$Sr record is noisier from ∼210 to ∼120 ka, varying between 0.34–0.42‰ without a clear trend. Fitting a LOWESS polynomial weighted least squares regression with a span of $\leq$10% suggests that there may be some underlying structure to the $\delta^{88/86}$Sr variation within this period, with a slight decrease in $\delta^{88/86}$Sr between 175–150 ka. However, we are cautious about overinterpreting this interval given the large signal-to-noise ratio.

Between ∼120 and 66 ka, seawater $\delta^{88/86}$Sr decreased from ∼0.39‰ to 0.34‰. The record then shows several rapid shifts in $\delta^{88/86}$Sr between 66 ka and present day, starting with a 0.07‰ increase between 66 and 50 ka followed by a decrease of ∼0.05–0.06‰ by between 50 and 33 ka. After 33 ka, seawater $\delta^{88/86}$Sr increased to ∼0.39–0.40‰ between

21 and 14 ka, and finally decreased to a Holocene average of 0.37‰ (10 ka to present).

Marine barite ^{87}Sr/^{86}Sr values gradually increased over 250 kyr at a rate of 0.000059 Myr^{-1} (Figure 4.2B), comparable to the well-established record of ^{87}Sr/^{86}Sr in seawater which shows a long-term increase of 0.000054 Myr^{-1} (Vance et al., 2009). We compared the barite ^{87}Sr/^{86}Sr values from this study to published data from foraminifera (Ando et al., 2010; Henderson et al., 1994; Mokadem et al., 2015) and found them to be in good agreement (Figure 4.3). While structured variations in ^{87}Sr/^{86}Sr are not apparent in the data, Mokadem et al. (2015) previously used the foraminifera datasets to show that ^{87}Sr/^{86}Sr variation due to non steady-state changes of ±15% in the weathering flux can be accommodated within the data error envelope. Our barite ^{87}Sr/^{86}Sr measurements are generally consistent with the ^{87}Sr/^{86}Sr envelope defined by all the published datasets and with the Mokadem et al. (2015) model curve, and provide improved constraints for 150–250 ka where the existing datasets are sparse (Figure 4.3).

4.4.2 Marine barite Sr/Ba ratios

In core TTN013-PC83, where we have the most continuous and highest resolution sampling coverage, we found that marine barite Sr/Ba ratios varied systematically between ∼30–40 mmol/mol over the past 250 kyr. Previous work has suggested that barite Sr/Ba ratios may qualitatively indicate changes in seawater [Sr] (Averyt, 2004), but this proposed proxy has not been rigorously developed. The record of seawater $\delta^{88/86}$Sr is not significantly correlated with barite Sr/Ba fluctuations, suggesting differences in mechanism(s). The barite Sr/Ba reconstruction and its comparison to sea level changes and previous Sr/Ba records is presented in Appendix A.

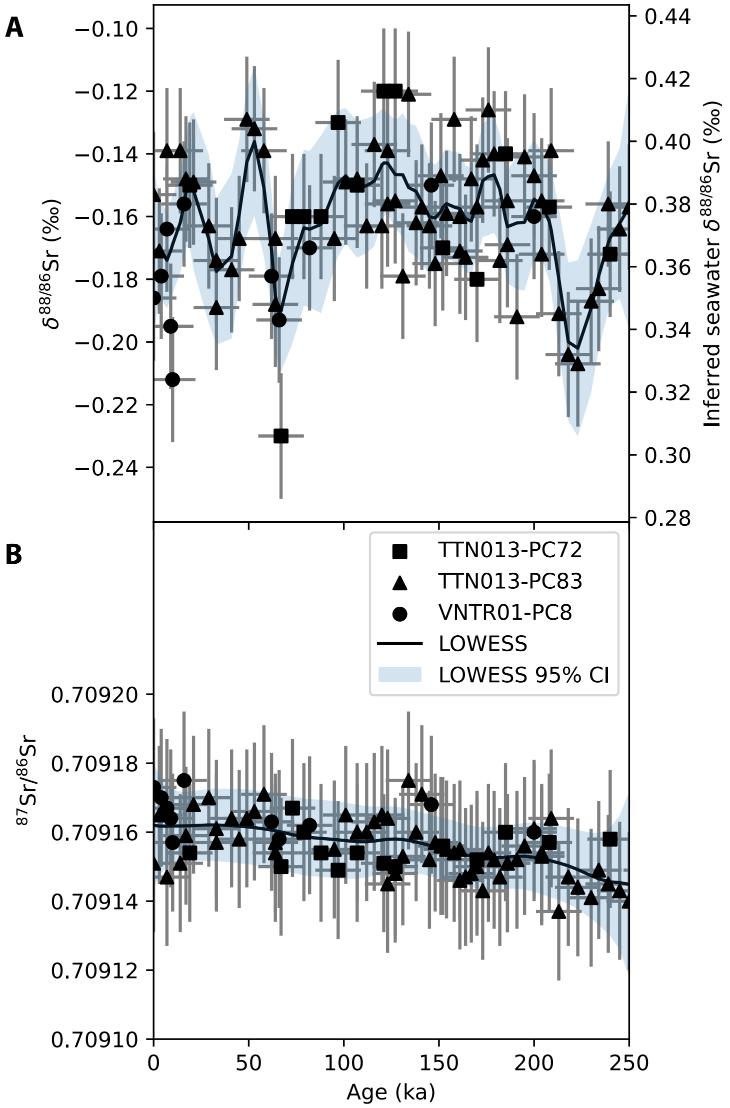

Figure 4.2: **(A)** Stable Sr isotope record in marine barite (*left axis*) with a polynomial weighted least squares regression (LOWESS). The inferred seawater $\delta^{88/86}$Sr values (*right axis*) were calculated using a constant seawater-barite isotopic offset of 0.536‰ as in Paytan et al. (2021). **(B)** Radiogenic Sr isotope record in marine barite with LOWESS fit. Error bars in both **(A)** and **(B)** are given by the long-term reproducibility of the isotopic measurements and by the estimated age uncertainty (see discussion).

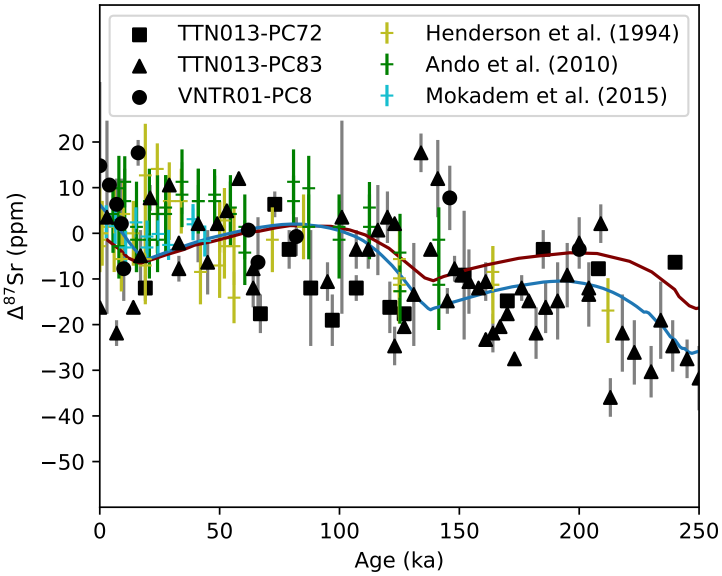

Figure 4.3: Radiogenic Sr isotope data for marine barite (black symbols, this study) and foraminifera reported by Ando et al. (2010), Henderson et al. (1994), and Mokadem et al. (2015) (colored "+" symbols). For each dataset, ^{87}Sr/^{86}Sr values were normalized to the reported value for modern seawater (Δ^{87}Sr (ppm) = ((^{87}Sr/^{86}Sr$_{sample}$/^{87}Sr/^{86}Sr$_{seawater}$) - 1) × 10^6) All errors are the analytical uncertainty (2σ, ppm). The red curve shows the modeled seawater ^{87}Sr/^{86}Sr response from Mokadem et al. (2015), which suggests that ±15% non steady-state variation in the weathering flux can be accommodated within the data envelope. The blue curve shows the model prediction from simulation ICE-PC2-SpLi16-F (this study).

4.4.3 Modeled relationship between sea level and seawater Sr

Model simulations forced by four different sea level histories illustrate the predicted magnitude and timing of seawater $\delta^{88/86}$Sr, [Sr], and ^{87}Sr/^{86}Sr variations due to shelf flooding and exposure over two glacial cycles. We compared predictions from: an idealized sea level curve (sinusoid) simulating sea level fluctuations between 0 and -120 m over the last two glacial cycles (Figure 4.4); a δ^{18}O-derived global mean sea level (GMSL) curve (Spratt & Lisiecki, 2016) (Figure 4.5); and spatially-resolved relative sea level (RSL) reconstructions based on glacial isostatic adjustment (GIA) modeling (Figures 4.6 and 4.7).

Table 4.1: Model simulations performed with different sea level histories and aragonite recrystallization rates. The sea level reconstructions are described in detail in Appendix A.

Simulation	**Sea Level Reconstruction**	**Recrystallization rate**	$\mathbf{t_{1/2}}$ **(kyr)**
SINE-S	sine wave (idealized)	slow	20
SINE-F	sine wave (idealized)	fast	5
GMSL-S	δ^{18}O-based GMSL[a]	slow	20
GMSL-F	δ^{18}O-based GMSL[a]	fast	5
ICE-PC2-S	GIA model RSL, ICE-PC2 ice history[b]	slow	20
ICE-PC2-F	GIA model RSL, ICE-PC2 ice history[b]	fast	5
ICE-PC2-SpLi16-S	GIA model RSL, ICE-PC2 + SpLi16 GMSL	slow	20
ICE-PC2-SpLi16-F	GIA model RSL, ICE-PC2 + SpLi16 GMSL	fast	5

[a] Spratt and Lisiecki (2016); [b] Pico et al. (2017); [c] Lisiecki and Raymo (2005)

Magnitude of modeled seawater Sr response

Across all of our model simulations, none of the sea level histories produced $\delta^{88/86}$Sr changes greater than 0.01‰ (Figures 4.4–4.7). There are differences in the timing of $\delta^{88/86}$Sr variations between simulations, but overall the predicted changes are within the analytical uncertainty of $\delta^{88/86}$Sr measurements. While the magnitude of the predicted $\delta^{88/86}$Sr change is small compared to our observations, the shelf carbonate fluxes predicted by the model that drove the $\delta^{88/86}$Sr responses (Figures A.7–A.10) are generally consistent with current estimates of Quaternary carbonate burial and previous modeling of the shelf carbonate burial/recrystallization mechanism (Stoll & Schrag, 1998).

All simulations predicted ∼3–4% variations in seawater [Sr], comparable in magnitude to the predictions made by Stoll and Schrag (1998) using a similar shelf-ocean model (1–3% variation in Sr/Ca). The recrystallization fluxes predicted by our shelf model are also comparable in magnitude to the flux predicted by Stoll and Schrag (1998). While the recrystallization flux varied significantly between our simulations due to the direct link between accumulated carbonate, sea level fall, and recrystallization, the flux typically ranged from negligible to peak values of ∼400–500 Gmol Sr yr^{-1}. Peak recrystallization fluxes were higher (∼1000 Gmol Sr yr^{-1}) for the RSL simulations due to substantially higher carbonate burial fluxes (Figure A.9 and A.10).

The shelf carbonate burial fluxes predicted by the continental shelf model are broadly consistent with estimates for the Quaternary carbonate budget based on observations and numerical modeling (Husson et al., 2018; Kleypas, 1997; M. Wood et al., 2023). Predicted total carbonate burial at interglacial high stands was approximately the modern flux (1.4 Pg $CaCO_3$ yr^{-1}) with about 0.7 Pg $CaCO_3$ yr^{-1}, 0.4 Pg $CaCO_3$ yr^{-1}, and 0.3 Pg $CaCO_3$ yr^{-1} buried in corals, bays, and carbonate-rich shelves, respectively (Figures A.7–A.10). Minimum total fluxes at glacial low stands were approximately 0.2 Pg $CaCO_3$ yr^{-1} with roughly half buried by coral reefs. These fluxes generally align with the reef model predictions of Kleypas (1997), which suggested that reef area was reduced by 80% at the LGM and reef production was 27% of the modern flux. Husson et al. (2018) similarly predicted peak reef production rates on the order of 0.5–5 Pg $CaCO_3$ yr^{-1} for typical high stands (∼50–80% of which can be assumed to accumulate) with minimal production during periods of sea level fall.

In summary, the model simulations did not reproduce the ∼0.1‰ range observed in our seawater $\delta^{88/86}$Sr reconstruction despite predicting realistic shelf carbonate recrystallization and burial fluxes. The modeled seawater ^{87}Sr/^{86}Sr response approximately reproduced the prediction of Mokadem et al. (2015); differences between the two model curves are due to the inclusion of incongruent weathering by Mokadem et al. (2015) which we neglected. Our model curve fits well within the range of reconstructed seawater ^{87}Sr/^{86}Sr values from this study and published records (Ando et al., 2010; Henderson et al., 1994; Mokadem et al., 2015) (Figure 4.3). Differences in predicted seawater ^{87}Sr/^{86}Sr between our simulations are negligible because radiogenic Sr is dominantly controlled by the weathering input.

Timing of modeled seawater Sr response

While all simulations predict $\delta^{88/86}$Sr changes of a similar magnitude, the sinusoidal, GMSL, and RSL model forcings produced seawater $\delta^{88/86}$Sr trends with variable timing due to differences in the onset of shelf flooding and exposure. Seawater [Sr] changes mirrored those of $\delta^{88/86}$Sr, as both were driven by the same processes and changed at the same time in opposing directions.

The sinusoidal sea level simulations (SINE-F, SINE-S) illustrate the timing of seawater $\delta^{88/86}$Sr change relative to idealized shelf flooding and exposure (Figure 4.4). Beginning at peak interglacial conditions ∼250 ka, seawater $\delta^{88/86}$Sr increased during the initial sea level fall for about 25 kyr until sea level dropped below -20 m and recrystallization caused $\delta^{88/86}$Sr to decrease. When sea level rose to about -60 m around 150 ka, $\delta^{88/86}$Sr increased again until peaking around 100 ka. Again, peak $\delta^{88/86}$Sr values lagged the high stand by about 25 ka. $\delta^{88/86}$Sr decreased until around 40 ka and began increasing toward present when sea level rose to about -60 m once more.

The GMSL simulations (GMSL-F, GMSL-S) $\delta^{88/86}$Sr results are similar in shape to the SINE runs but show additional structure within the 100-kyr cycles reflecting relatively small interstadial sea level fluctuations and offsets in the timing of sea level maxima and minima (Figure 4.5). Starting at 250 ka, seawater $\delta^{88/86}$Sr increased until 190 ka with only a small response to the glaciation-deglaciation sea level change around 225 ka. Seawater $\delta^{88/86}$Sr then decreased along with sea level until 130 ka when sea level rose rapidly following the low stand ~135 ka and $\delta^{88/86}$Sr increased. The 70 ka peak in $\delta^{88/86}$Sr was followed by decreasing $\delta^{88/86}$Sr until ~19 ka, when $\delta^{88/86}$Sr increased toward present.

Differences in the GMSL- and RSL-forced seawater $\delta^{88/86}$Sr trends arose from differences in the timing and extent of local shelf flooding/exposure. The GMSL forcing was uniformly applied across space, while the RSL forcings (ICE-PC2, ICE-PC2-SpLi16) captured local changes in sea level due to GIA (see Appendix A). Accounting for GIA also leads to differences in the estimated eustatic sea level curves for the GMSL and RSL scenarios, for example, the relative magnitude of the mid-MIS 3 high stand (see Pico et al. (2017) and discussion below).

The ICE-PC2 and ICE-PC2-SpLi16 sea level histories differ only in the penultimate glacial cycle, as the ICE-PC2 ice sheet history was used for 0–122 ka in both reconstructions. The predicted $\delta^{88/86}$Sr trends are very similar for both forcings, with one slight difference ~160 ka where ICE-PC2 predicts a higher peak $\delta^{88/86}$Sr value than ICE-PC2-SpLi16. From 250 ka until about 190 ka, $\delta^{88/86}$Sr increased until a slight decrease around 190 ka. Seawater $\delta^{88/86}$Sr peaks again around 160 ka before decreasing until 130 ka. Deglaciation ~130 ka led to a large increase in $\delta^{88/86}$Sr over about 60 kyr. A small decrease in $\delta^{88/86}$Sr occurred with the third interstadial sea level drop ~70 ka before $\delta^{88/86}$Sr increased along with sea level ~60 ka in contrast to the GSML simulations where $\delta^{88/86}$Sr only decreased between 70 and 19 ka. The interstadial high stand was more important in the RSL simulations, where substantially more carbonate was buried on the shelf (Figures A.8 –A.10). The increase in $\delta^{88/86}$Sr continued after the interstadial high stand until 36 ka when it again dropped as sea level decreased below -60 m. Finally, $\delta^{88/86}$Sr reached a minimum around 19 ka before increasing toward present.

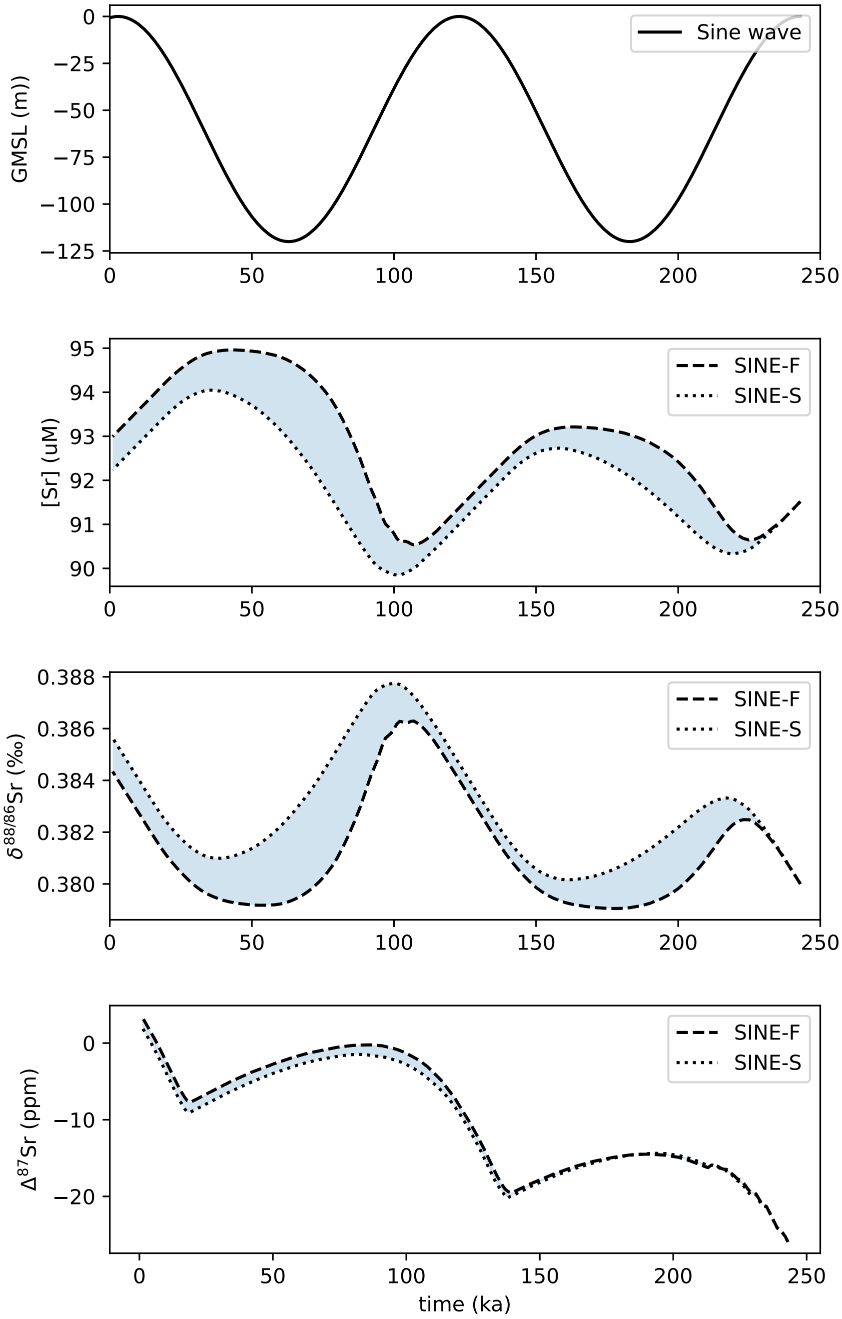

Figure 4.4: Model results for sinusoidal sea level forcing of shelf carbonate burial and recrystallization. Fast (SINE-F, $t_{1/2} = 5$ kyr, dashed line) and slow (SINE-S, $t_{1/2} = 20$ kyr, dotted line) aragonite recrystallization rates were tested to illustrate the sensitivity of the results to this parameter.

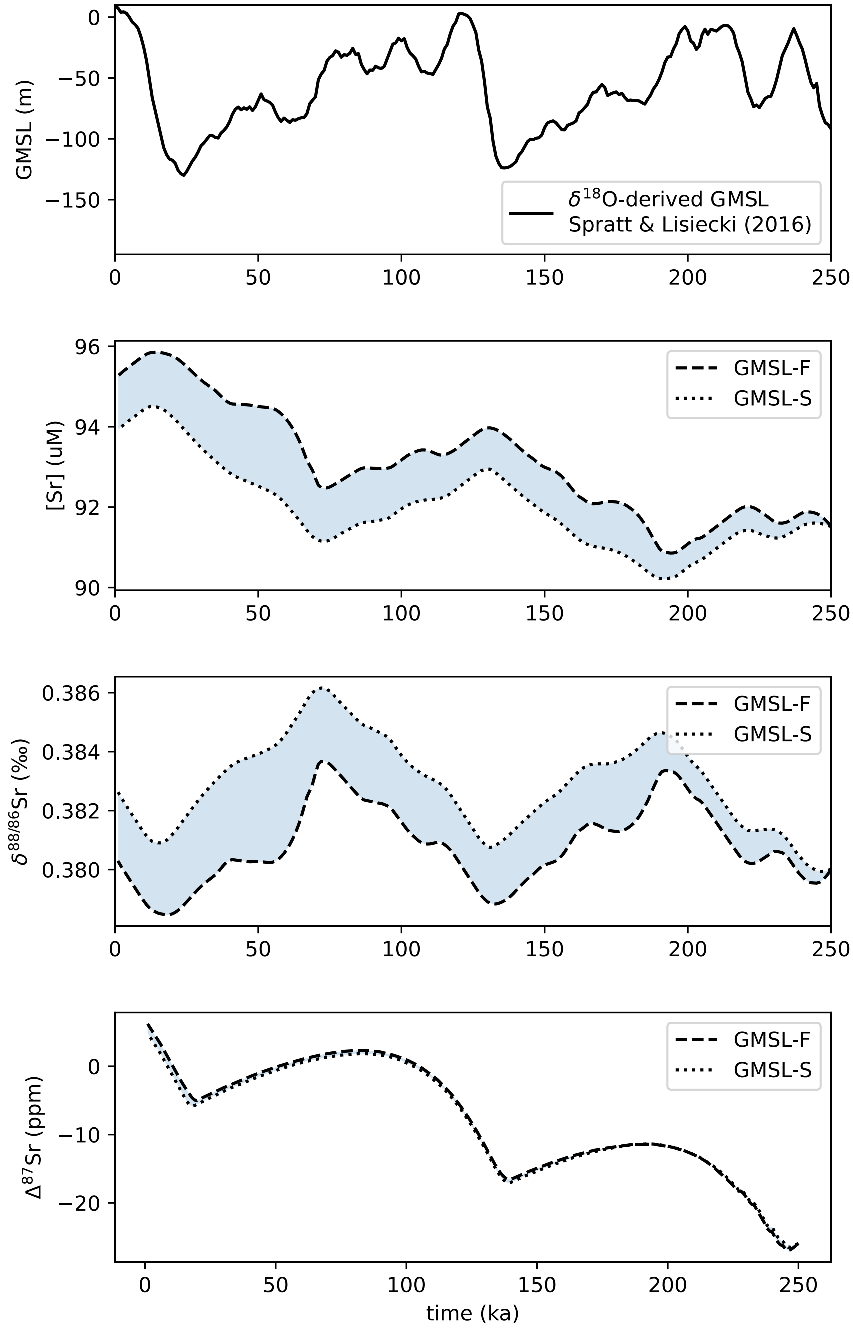

Figure 4.5: Model results for global mean sea level forcing of shelf carbonate burial and recrystallization. Fast (GMSL-F, $t_{1/2} = 5$ kyr, dashed line) and slow (GMSL-S, $t_{1/2} = 20$ kyr, dotted line) aragonite recrystallization rates were tested to illustrate the sensitivity of the results to this parameter.

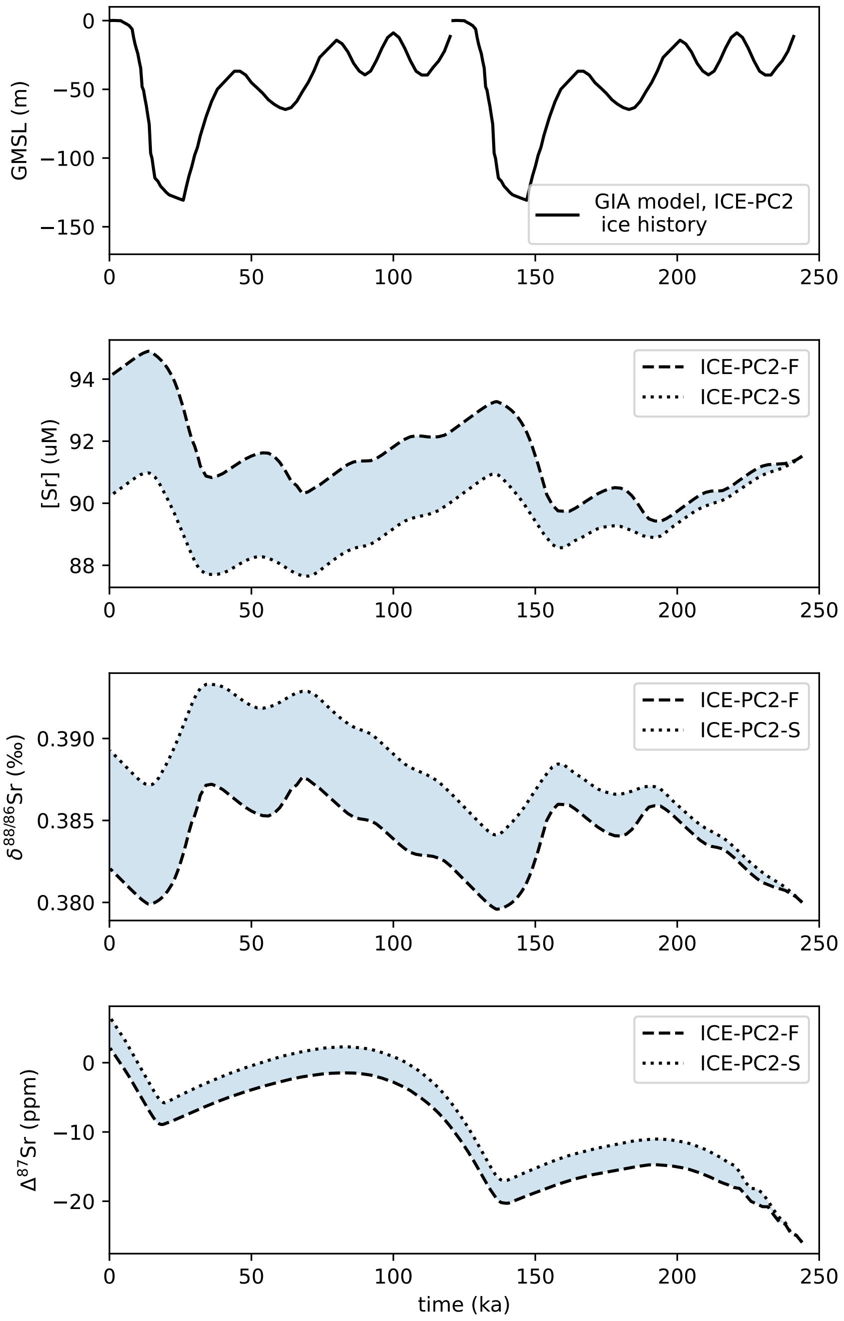

Figure 4.6: Model results for ICE-PC2 relative sea level forcing of shelf carbonate burial and recrystallization. Fast (ICE-PC2-F, $t_{1/2} = 5$ kyr, dashed line) and slow (ICE-PC2-S, $t_{1/2} = 20$ kyr, dotted line) aragonite recrystallization rates were tested to illustrate the sensitivity of the results to this parameter.

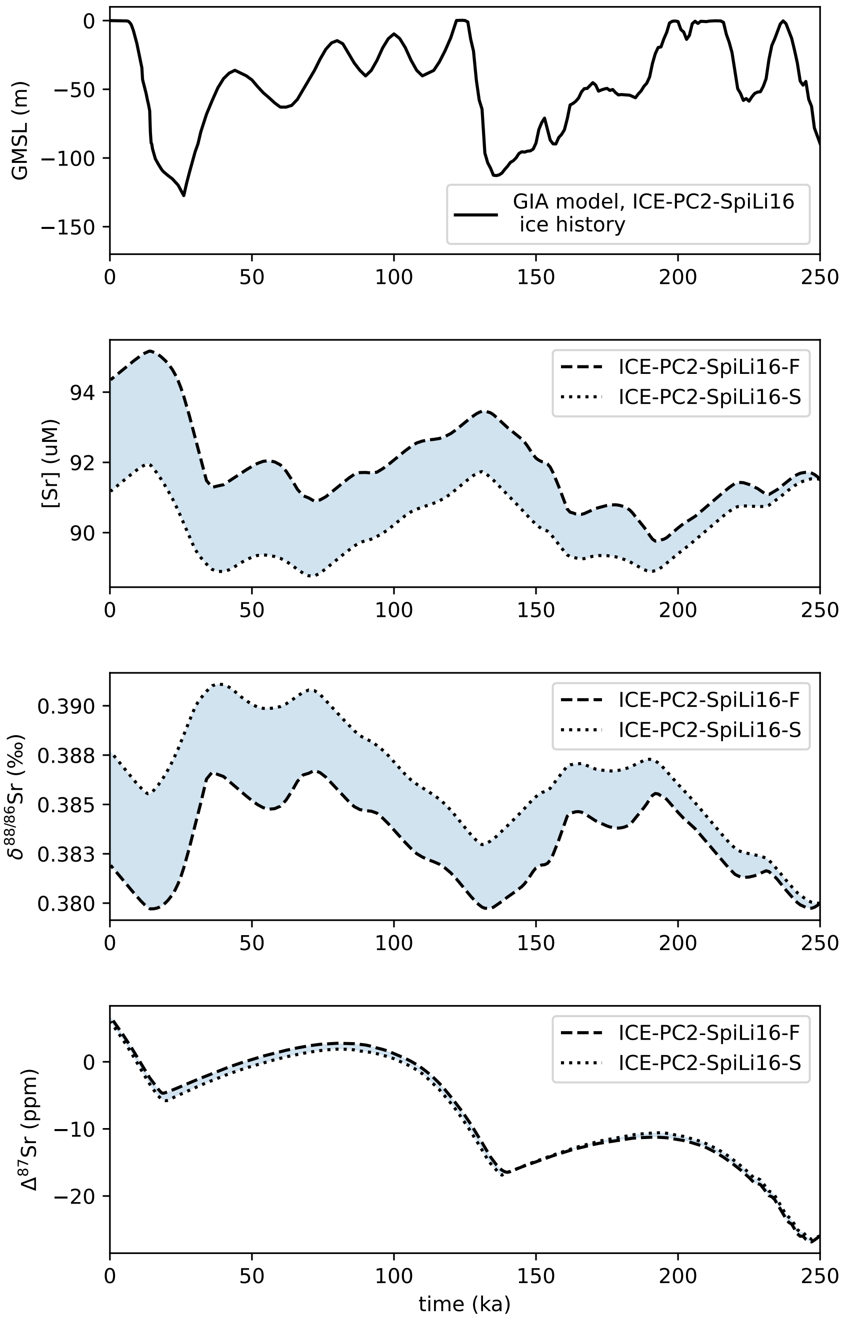

Figure 4.7: Model results for ICE-PC2-SpLi16 relative sea level forcing of shelf carbonate burial and recrystallization. Fast (ICE-PC2-SpLi16-F, $t_{1/2} = 5$ kyr, dashed line) and slow (ICE-PC2-SpLi16-S, $t_{1/2} = 20$ kyr, dotted line) aragonite recrystallization rates were tested to illustrate the sensitivity of the results to this parameter.

4.5 Discussion

4.5.1 A dynamic glacial/interglacial strontium budget

Our 250-kyr reconstruction of seawater $\delta^{88/86}$Sr clearly demonstrates that $\delta^{88/86}$Sr fluctuated over relatively short (<50 kyr) timescales during the Pleistocene. Systematic $\delta^{88/86}$Sr changes of ~0.05‰ occurred independently of seawater ^{87}Sr/^{86}Sr, consistent with changes in the Sr inventory due to shelf carbonate burial and recrystallization which do not significantly impact ^{87}Sr/^{86}Sr. The range of $\delta^{88/86}$Sr (~0.1‰) over the last two glacial cycles is equal to the entire range reconstructed for the Late Cenozoic (Paytan et al., 2021), implying that glacial/interglacial processes are a strong lever on Sr budget imbalances and the stable isotopic composition. However, we failed to reproduce the reconstructed $\delta^{88/86}$Sr variations in model simulations based on our current understanding and relatively simple approximation of shallow carbonate burial changes in the past, aragonite recrystallization rates, ice sheet histories, and sea level fluctuations. We take the data-model mismatch as evidence that a fundamental control on seawater Sr cycling over glacial/interglacial cycles is missing from our conceptualization of the shelf carbonate burial/recrystallization mechanism. In the discussion that follows, we evaluate the hypothesized link between seawater $\delta^{88/86}$Sr and sea level changes, which we had expected to be correlated, and consider alternative explanations for the observed $\delta^{88/86}$Sr fluctuations.

4.5.2 Relating $\delta^{88/86}$Sr to global mean sea level

The shelf carbonate burial/recrystallization hypothesis predicts that seawater $\delta^{88/86}$Sr will be low during periods of low sea level (high shelf exposure) when carbonate sediments recrystallize and provide a source of isotopically-light Sr to the ocean. The flooding of exposed shelves would theoretically cause $\delta^{88/86}$Sr to increase as neritic carbonate burial increases, leading to relatively higher $\delta^{88/86}$Sr during sea level high stands. However, the predicted relationship between seawater $\delta^{88/86}$Sr and sea level is not consistently borne out in the data. Comparison of the smoothed $\delta^{88/86}$Sr record with GMSL (Pico et al., 2017; Spratt & Lisiecki, 2016) shows contrasting patterns for the last two glacial cycles that are not clearly related to changes in sea level, despite some periods where they appear coupled (Figure 4.8).

For most of the last glacial cycle (122 to ∼35 ka), seawater $\delta^{88/86}$Sr trends follow sea level variations (Figure 4.8). The first of three major decreases in $\delta^{88/86}$Sr occurs between 120 and 66 ka as sea level decreases after the LIG high stand. Seawater $\delta^{88/86}$Sr then increases around the mid-MIS 3 high stand (Pico et al., 2017), consistent with increasing neritic carbonate burial on flooded shelves. The sea level drop following the mid-MIS 3 high stand is associated with a decrease in $\delta^{88/86}$Sr as expected if the carbonate sediments deposited on the shelf during the high stand recrystallized upon subsequent exposure. Just prior to the LGM, however, seawater $\delta^{88/86}$Sr increases while sea level continues to decrease into the glacial maximum. This LGM peak in $\delta^{88/86}$Sr is not consistent with the shelf carbonate burial/recrystallization mechanism, which predicts low $\delta^{88/86}$Sr at the LGM. The record also suggests that the Holocene $\delta^{88/86}$Sr values are lower than at the LGM, which is the opposite of what we expect if deglaciation is associated with increased neritic carbonate burial and increasing seawater $\delta^{88/86}$Sr. If the changes in seawater $\delta^{88/86}$Sr prior to ∼35 ka were related to shelf carbonate burial/recrystallization, there must be another factor to explain why the relationship between sea level and $\delta^{88/86}$Sr breaks down in the most recent section of the record, specifically why seawater $\delta^{88/86}$Sr began increasing before the LGM and decreased during deglaciation.

In the previous glacial cycle (250–122 ka), seawater $\delta^{88/86}$Sr is less variable and appears less related to sea level change (Figure 4.8). Most notably, there is little difference or change in seawater $\delta^{88/86}$Sr between the penultimate glacial maximum (PGM, 160–140 ka) and the Last Interglacial (LIG, 130 ka). As the deglaciation is associated with rapid sea level rise of ∼120 m to peak levels 5.5–9 m above modern-day sea level (Dutton & Lambeck, 2012), we would expect seawater $\delta^{88/86}$Sr to increase at least as significantly as observed for the mid-MIS 3 high stand, if indeed $\delta^{88/86}$Sr reflects increased neritic carbonate burial when exposed continental shelves become flooded. Instead, there is only a small change in $\delta^{88/86}$Sr (<0.03‰) associated with the deglaciation. The major $\delta^{88/86}$Sr change of the previous glacial cycle occurred during the penultimate interglacial (MIS 7, 240–170 ka). Between 250 and 200 ka seawater $\delta^{88/86}$Sr decreased from ∼0.38‰ to ∼0.34‰ before rebounding to 0.38‰. This $\delta^{88/86}$Sr change is associated with the MIS 7e-7d-7c glaciation and deglaciation, which was one of the fastest glaciation–deglaciation events of the Pleistocene (global ice volume change of ∼60 m global sea level equivalent within 20 kyr) (Choudhury et al., 2020). While the $\delta^{88/86}$Sr changes during MIS 7 fit our expectation for exposure and re-flooding of the continental shelves during the glaciation–deglaciation transition, it is unclear why a similar response would not be seen for the penultimate deglaciation around 138 ka.

Statistically, there is no evidence for strong correlation between the seawater $\delta^{88/86}$Sr record and GMSL over the past 250 kyr despite the coincident timing of the more significant changes in $\delta^{88/86}$Sr with rapid sea level fluctuations (e.g., mid-MIS 3 high stand, MIS 7e-7d glaciation). The lack of correlation doesn't necessarily rule out the shelf carbonate burial/recrystallization mechanism, but implies that shelf carbonate burial/recrystallization cannot simply be driven by GMSL if this is in fact the mechanism behind the $\delta^{88/86}$Sr changes.

4.5.3 Age model uncertainties

It is important to consider that the timing of the seawater $\delta^{88/86}$Sr changes we observe may be biased by uncertainties in the age models. The TTN013-PC72 and VNTR01-PC8 sediment core age models are derived from correlation of δ^{18}O with the SPECMAP stack (Murray et al., 2000; Pisias & Mix, 1997). The age model for TTN013-PC83 was determined by correlation of carbonate content with TTN013-PC72 (Murray et al., 2000). The TTN013-PC72 age model used here includes updated 14C ages from Winckler et al. (2008) for the upper 100 cm, though this update directly impacts the age estimate of only one of our samples at 46 cm depth and does not substantially shift the overall $\delta^{88/86}$Sr trend relative to the original Murray et al. (2000) age model. However, the Winckler et al. (2008) 14C ages demonstrate that the Murray et al. (2000) age model for TTN013-PC72 is biased younger by ∼2–7 ka over the upper 100 cm (0–40 ka), with the greatest bias between ∼50–70 cm (16–26 ka) (Figure A.12). Consequently, the age model used for TTN013-PC83 must be similarly biased, raising the possibility that the timing of the seawater $\delta^{88/86}$Sr changes are offset relative to sea level changes. Specifically, the apparent $\delta^{88/86}$Sr decrease observed at the deglaciation (∼14 ka) may instead be associated with the LGM low stand (∼21 ka), and the preceding peak in $\delta^{88/86}$Sr (14–21 ka) that we relate to the LGM may instead be associated with the mid-MIS 3 high stand (∼44 ka), with $\delta^{88/86}$Sr increasing during the high stand before decreasing with a ∼15-kyr lag behind sea level fall (Figure A.12). Lags in the seawater $\delta^{88/86}$Sr response to sea level changes are possible given an approximate decay half life of ∼10–40 kyr for aragonite-to-calcite recrystallization (Stoll & Schrag, 1998). We did not find evidence for strong lagged correlations between sea level and seawater $\delta^{88/86}$Sr across the duration of our record, but such relationships could be obfuscated by these age uncertainties.

We estimate an age uncertainty of ±12 kyr (error bars in Figure 4.2) based on the SPECMAP stack uncertainty of ±5 kyr (Martinson et al., 1987) and up to 7 kyr bias in the Murray et al. (2000) age models. We also note that bioturbation and mixing of sediments could have impacted our reconstructed seawater $\delta^{88/86}$Sr trends and likely contributed to some of the $\delta^{88/86}$Sr variability observed between barite samples close in age. For example, for a significant seawater $\delta^{88/86}$Sr change occurring within a 10-kyr time slice, core samples within that 10-kyr window may represent a mixture of the two $\delta^{88/86}$Sr extremes (Paytan et al., 2021). While these equatorial Pacific sediment cores are advantageous for the high barite accumulation rates and excellent preservation of this reliable seawater $\delta^{88/86}$Sr archive, these age uncertainties complicate the interpretation of mechanistic drivers of the $\delta^{88/86}$Sr changes observed, as will potential leads/lags in this system. In the following discussion, we explore potential explanations for the differences between sea level and $\delta^{88/86}$Sr trends in the record we have produced, with the caveat that high resolution records with higher confidence age models will be required to resolve the exact timing of $\delta^{88/86}$Sr variations relative to sea level, particularly for the LGM to present.

4.5.4 Importance of relative sea level changes

A potential explanation for the disconnect between observed seawater $\delta^{88/86}$Sr variations and GMSL change is the importance of local sea level change in regions that are carbonate factory hot spots. The (re)flooding and (re)exposure of shelves in key regions such as the Indo-Pacific or Caribbean over repeated sea level fluctuations might exert stronger influence on the Sr budget than globally-averaged sea level changes. Not only is the timing of RSL changes important, but δ^{18}O-derived GMSL has been shown to systematically underestimate GMSL during interstadial periods (de Gelder et al., 2020, 2022), which would lead to overestimation of shelf exposure and underestimation of the neritic Sr sink. For example, recent analysis of Huon Peninsula RSL indicators showed that interstadial sea level highstands (e.g., MIS 3, 5a, 5c, 6) are higher than δ^{18}O-derived GMSL estimates by up to ∼20 m (de Gelder et al., 2022). RSL predictions from GIA modeling produced a better fit to the Huon MIS 3 highstand indicators (Pico et al., 2017) and predicted substantially greater shelf inundation at high stands, particularly at MIS 3 (and thus greater exposure leading up to the LGM) (Figure A.6).

This consideration motivated our inclusion of the RSL forcings in our model simulations, which did influence the timing of seawater $\delta^{88/86}$Sr changes compared to the GMSL forcing (Figures 4.5–4.7). These differences are driven primarily by variable accumulation of carbonate within the assumed depth ranges for corals, seagrasses, and other shallow calcifiers. Seawater $\delta^{88/86}$Sr increased most significantly when relatively high sea levels accommodated high carbonate burial for a sustained period, and decreased significantly when sea level fall and shelf exposure coincided with large volumes of accumulated carbonate becoming exposed. For example, in the last glacial period GMSL-forced seawater $\delta^{88/86}$Sr peaked around 70 ka before decreasing toward the LGM, while the RSL-forced seawater $\delta^{88/86}$Sr peaked much later around 36 ka as high fluxes of carbonate accumulation were sustained by relatively extensive submergence of shelves in key regions like the Indo-Pacific. Setting aside the mismatch in the magnitude of observed versus predicted $\delta^{88/86}$Sr changes, the RSL effect might explain the timing of the $\sim$50 ka peak in $\delta^{88/86}$Sr (Figure 4.8) if, for example, the mid-MIS 3 high stand supported widespread reef accumulation. However, accounting for RSL changes still cannot explain why seawater $\delta^{88/86}$Sr began increasing before the LGM and decreased during the deglaciation, or why there was little change through the penultimate glacial maximum and deglaciation. These $\delta^{88/86}$Sr patterns might be related to complexity in how reefs grow (e.g., depositional processes) and recrystallize (e.g., possibly after re-submergence in seawater) and potential time lags associated with these processes that are not captured by our simple model.

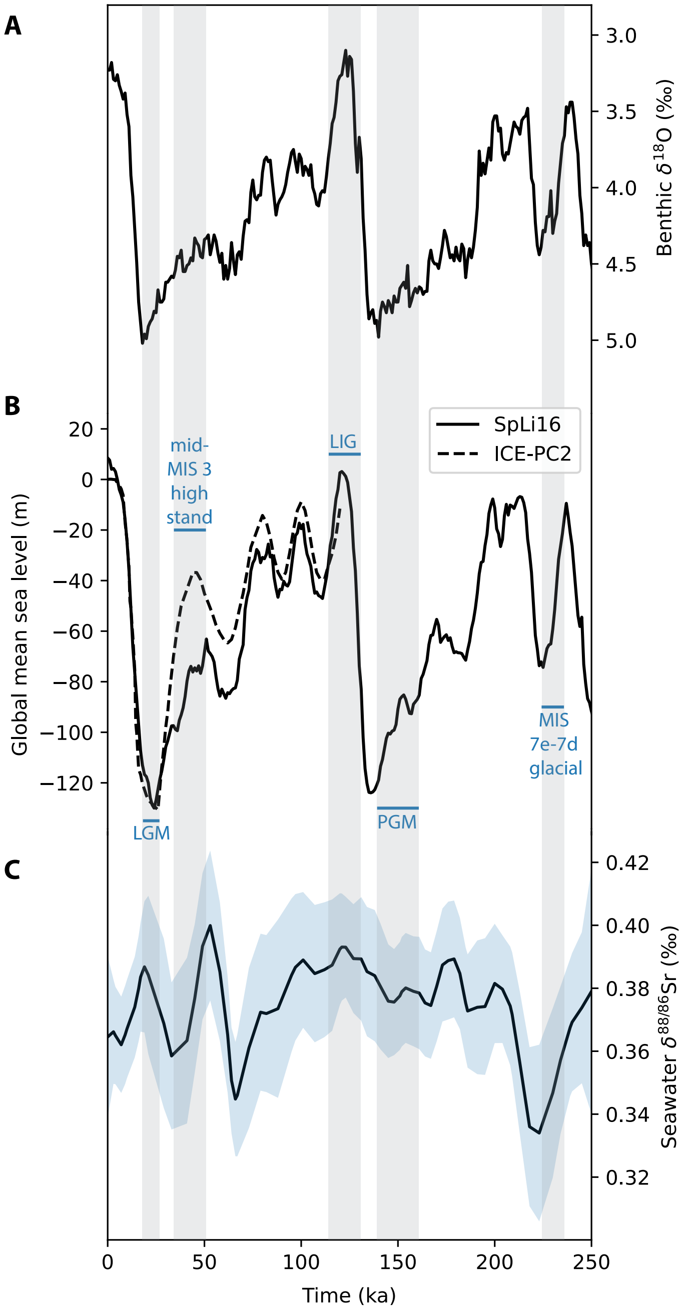

Figure 4.8: **(A)** Benthic $\delta^{18}O$ (Lisiecki & Raymo, 2005) and **(B)** global mean sea level reconstructed from $\delta^{18}O$ (solid line, Spratt & Lisiecki, 2016) and GIA modeling (dashed line, Pico et al., 2017) compared to **(C)** seawater $\delta^{88/86}Sr$ trends (LOWESS fit to the data with the 95% CI given by the shaded ribbon). Key transitions are highlighted by vertical shading, including the Last Glacial Maximum (LGM), Last Interglacial (LIG), and Penultimate Glacial Maximum (PGM).

4.5.5 Alternative drivers of seawater $\delta^{88/86}$Sr change

While sea level is typically regarded as the main driver of spatiotemporal variations in reef development and shallow carbonate accumulation, there are many factors that may influence glacial/interglacial reef growth (for detailed discussion, see Montaggioni, 2005). The response of coral communities to different rates of sea level rise depends on their depositional processes and growth styles (e.g., accretion rates, morphological structures) which can allow reefs to "keep up" or "catch up" to sea level rise, or cause reefs to be drowned. Environmental factors like sea surface temperature, salinity, nutrients, light intensity, wave energy and erosion are fundamental controls on reef growth (Montaggioni, 2005). Aragonite saturation state determines the calcification rate of corals and is thought to have been higher than present during the LGM when $p\mathrm{CO}_2$ was lower. Glacial aragonite saturation states might therefore have been more favorable for aragonite accretion with conditions becoming less favorable during deglaciation. Small-scale topographic features (e.g., substrate type, changes in slope, paleochannels) influence colonization and accretion by providing favorable substrate (Hinestrosa et al., 2014). Reef growth can also impact carbonate accumulation in other environments that contribute to the neritic carbonate budget (e.g., embayments, lagoons, estuaries) by altering shelf physiology; the topography, slope, drainage patterns are all potential controls on the accumulation versus export of shelf sediments (Hinestrosa et al., 2019).

All of these factors complicate the prediction of shallow carbonate burial fluxes back in time, and may help explain why the observed seawater $\delta^{88/86}$Sr changes do not follow a simple sea level model. The geographical distribution and development of reefs before the Holocene is very poorly constrained, as the majority of these fossil coral reefs are submerged at present. We focused in on the seawater $\delta^{88/86}$Sr record between $\sim$30 ka and present, a period for which geological reef records are available, to try to link field observations of LGM and post-glacial reef development to the $\delta^{88/86}$Sr trends.

4.5.6 Fossil coral reef records 30 ka to present

Some of the best constraints on LGM coral reef accumulation come from recent work at the world's largest reef system, the Great Barrier Reef (GBR). Webster et al. (2018) demonstrated that reefs were established on the GBR shelf edge at the LGM ($\sim$27 ka) following the sea level fall after the MIS 3 high stand. The shelf-edge reefs migrated seaward as RSL continued to fall to ~21 ka, then flourished until 17 ka when deglacial sea level rise initiated landward migration. Both the presence of the shelf-edge reefs at the LGM and their ability to rapidly aggrade seaward in response to the LGM sea level fall suggests that there could have been thriving coral ecosystems during the LGM (Webster et al., 2018). Similarly, the presence of coral reefs in other Indo-Pacific regions around 23–18 ka indicates that environmental conditions at the LGM remained conducive to reef growth (Montaggioni, 2005).

The GBR fossil coral records also revealed a two-step structure in sea level fall during the LGM that is not captured in any of the GMSL or RSL sea level reconstructions discussed so far. After the initial rapid sea level fall around 31 ka, GMSL was relatively constant from 28–22 ka (at which time GBR shelf-edge reefs were thriving) around -113±6 m, much shallower than previously estimated (Yokoyama et al., 2018). Sea level dropped again by ~20 m around 21.5 ka to a low of -130 m to -125 m before rising toward the deglaciation (Yokoyama et al., 2018).

If the GBR is representative of LGM coral ecosystems globally (or at least in the key regions like the Indo-Pacific), perhaps environmental conditions and the aragonite saturation state were favorable for reef development even during the LGM low stand. Minimal changes in reef accumulation between the LGM and Holocene could explain why the carbonate saturation horizon did not deepen significantly during the LGM (Cartapanis et al., 2018; Catubig et al., 1998; Farrell & Prell, 1989; M. Wood et al., 2023; Yu, Anderson, & Rohling, 2014) as would be expected if alkalinity removal by shallow carbonate burial was greatly reduced. GBR fringing reefs initiated around 27 ka, which is approximately when seawater $\delta^{88/86}$Sr increased after decreasing from ~50–33 ka. The decrease in $\delta^{88/86}$Sr from peak LGM values also coincides with the ~20 m sea level fall reported by Yokoyama et al. (2018), which lowered sea level to a -130 m low stand at 21.5 ka. We postulate that this sea level drop may have tapped into a deep Sr reservoir in low stand corals from previous glacial cycles that had not since been exposed by sea level cycles. The recrystallization of these deep fossil reefs resulted in the low seawater $\delta^{88/86}$Sr values observed following the LGM before seawater $\delta^{88/86}$Sr increased to the modern value due to postglacial carbonate accumulation, which likely peaked ~10 ka (Husson et al., 2018).

4.5.7 A refined shelf carbonate burial/recrystallization hypothesis

The connections between seawater $\delta^{88/86}$Sr and patterns of coral reef accumulation in the GBR region are merely speculative because observational constraints are insufficient to determine if LGM carbonate burial fluxes would have been large enough to drive the observed $\delta^{88/86}$Sr change, or if deep fossil reefs below about -120 m had accumulated a large Sr reservoir during prior glacial cycles. However, the complexities of reef development potentially explain why seawater $\delta^{88/86}$Sr changes are not clearly linked to sea level changes despite shelf carbonate burial and recrystallization being the most likely drivers. That is, seawater $\delta^{88/86}$Sr trends are not a simple function of sea level rise and the expansion of the shelf area, but instead arise from the integrated effect of coral growth, shelf carbonate burial, and aragonite recrystallization. The shelf carbonate burial/recrystallization hypothesis can be extended beyond the simple model based on sea level and shelf area to a more nuanced mechanism that depends on episodic reef development in relation to rates of sea level change, environmental conditions, and the history of reef platforms over many glacial cycles.

We propose that sea level is the dominant control on the Sr recrystallization flux, with a secondary factor of accumulated carbonate volume in the habitatable depth range (e.g., 0–50 m below sea level). For sea level to drive a seawater $\delta^{88/86}$Sr decrease, a sufficiently large reservoir of Sr must be mobilized and not immediately reburied in the new habitatable depth range. This could occur if a deep reservoir of Sr buried during a previous low stand was tapped, or if the sea level fall coincides with a period of reduced carbonate accumulation (as in our initial conceptual model). In contrast to our original hypothesis, we postulate that the removal of Sr via neritic carbonate burial is not directly controlled by sea level, because the conditions of reef establishment, accumulation, and persistence are much more complicated. Consequently, significant increases in seawater $\delta^{88/86}$Sr may indicate convergence of reef growth factors on ideal conditions, for example, high aragonite saturation states, extensive substrate, rates of sea level rise equal to reef accretion rates, and shallow calcifier communities capable of migrating seaward or landward. We can also imagine an intermediate scenario where Sr is rapidly recycled between exposed coral reefs and those growing just below them, leading to a cascade effect as Sr is transferred to deeper shelf intervals as sea level drops with little seawater $\delta^{88/86}$Sr response. Such a scenario could explain why seawater

$\delta^{88/86}$Sr change was muted during the penultimate glacial cycle.

This model implies there should be an ultimate sink of Sr in low stand reefs and the timing of recrystallization fluxes (indicated by decreasing $\delta^{88/86}$Sr) might provide insight to preceding periods of carbonate accumulation. While geological observations of low stand reefs are sparse and reconstructing global neritic carbonate burial fluxes in the past remains challenging, we identified three potential test cases for our refined hypothesis. First, the beginning of Northern Hemisphere ice ages ~2.7 Ma should coincide with a significant decrease in $\delta^{88/86}$Sr as coral reefs built over the Oligocene and Pliocene were exposed and recrystallized. Second, the shift from 41-kyr glacial cycles to 100-kyr cycles at the Mid Pleistocene Transition (MPT) is associated with increased severity (amplitude) of glacial cycles (Clark et al., 2006); hence the largest Cenozoic sea-level changes have occurred over the past 800 kyr with ~100-kyr glacial terminations (Miller et al., 2020). Accordingly, Sr buried at sea level low stands prior to the MPT should have become mobilized when subsequent low stands exceeded the depth of the deepest reef deposits. Finally, unusually high sea levels at the MIS 11 (~400 ka) and MIS 31 (~1,070 ka) "super-interglacials" are predicted to have supported exceptionally high reef productivity compared to most interglacials (Husson et al., 2018). At MIS 31 sea level was higher than it had been for the preceeding 400 kyr, and the MIS 11 high stand exceeded that of MIS 31. At these times, the reef platforms built during the preceding interglacial periods were simultaneously flooded and likely provided ideal substrate and accommodation space for extensive reef accumulation (Husson et al., 2018). We would consequently expect MIS 11 and MIS 31 to be associated with high seawater $\delta^{88/86}$Sr values.

4.6 Conclusions

By reconstructing seawater $\delta^{88/86}$Sr over the past 250 kyr, we have shown that the ocean Sr budget was dynamic over glacial/interglacial cycles. The systematic variations in seawater $\delta^{88/86}$Sr occurred independently of ^{87}Sr/^{86}Sr, indicating that carbonate burial fluxes rather than weathering likely drove Sr mass imbalances on <50-kyr timescales. This finding adds to the accumulating evidence in favor of the shelf carbonate burial/recrystallization mechanism of Sr cycling during the Pleistocene. However, we also demonstrated that a simple model linking carbonate burial/recrystallization to flooded/exposed shelf area does not adequately explain the magnitude and timing of the seawater $\delta^{88/86}$Sr variations in relation to sea level fluctuations. In light of the mismatch between our observations and model predictions, we developed a more nuanced hypothesis for the cycling of Sr over glacial cycles and proposed a refined shelf carbonate burial/recrystallization mechanism that could be tested with records of seawater $\delta^{88/86}$Sr extending further back into the Pleistocene. Obtaining higher-resolution data spanning the LGM through the last deglaciation with wider geographic sampling coverage (e.g., using carbonate archives carefully screened for diagenetic alteration) would also provide better insight to the exact timing and global nature of the observed minima and maxima in seawater $\delta^{88/86}$Sr relative to sea level and climate changes, helping to elucidate mechanisms underlying the fluctuations we observe.

4.7 Acknowledgements

This research used samples provided by the University of Rhode Island Marine Geological Samples Laboratory. L. Ognibene assisted with the preparation of barite samples. T. Pico helped implement the ICE-PC2 relative sea level predictions in model simulations and S. Kodama developed the ICE-PC2-SpLi16 ice history. We acknowledge J. Webster for useful discussions of reef growth and erosion and T. Horner for sharing barite elemental ratio data for comparison to our findings. The study was supported by an IODP Schlanger Ocean Drilling Fellowship and graduate student research grants from the International Association of Geochemistry, Geological Society of America, Myers Oceanographic and Marine Biology Trust, and University of California, Santa Cruz Department of Earth and Planetary Sciences (to MMW).

Chapter 5

Seawater stable strontium isotope ratios during the Eocene-Oligocene Transition

This chapter has been submitted to *Geology*: Wood, M.M., Kolevica, A., Eisenhauer, Hain, M., A., Paytan, A. Seawater stable strontium isotope ratios during the Eocene-Oligocene transition.

5.1 Abstract

The greenhouse-to-icehouse climate shift at the Eocene-Oligocene Transition (EOT) was marked by global cooling, ice sheet growth, and a carbon cycle perturbation evident in the ~1 km deepening of the Pacific Ocean carbonate compensation depth (CCD). The favored mechanism for the carbon perturbation is a shelf-to-basin shift in carbonate ($CaCO_3$) burial and increased $CaCO_3$ weathering from exposed continental shelves during sea level fall. We investigated the impact of these carbon cycle changes on the ocean strontium (Sr) budget and seawater stable Sr isotopic composition ($\delta^{88/86}$Sr), reconstructed from marine barite in deep sea sediment cores. Our record shows minimal change in seawater $\delta^{88/86}$Sr (mean 0.38±0.03‰) indicating that the mechanisms responsible for deepening the CCD did not alter Sr sources or sinks sufficiently to perturb

the Sr isotopic mass balance. Shelf-to-basin repartitioning of $CaCO_3$ burial is consistent with the $\delta^{88/86}$Sr data only if Eocene shelf ecosystems were devoid of aragonitic calcifiers such as scleractinian corals and *Halimeda* macroalgae, which dominate neritic $CaCO_3$ production and Sr burial in the modern ocean. Eocene carbonate sequences composed almost entirely of low-Sr calcite instead held a small Sr inventory that was released to the ocean when sea level dropped. Further, the lack of a trend in seawater $\delta^{88/86}$Sr in the million years following the EOT suggests that geologic sources of Sr from weathering remained within ±10% of the $CaCO_3$ burial flux, without significantly upsetting the long-term ocean Sr isotope budget.

5.2 Introduction

A permanent ~1 km deepening of the carbonate compensation depth (CCD) coincided with the expansion of the Antarctic ice sheet at the Eocene-Oligocene Transition (EOT, ~34 Ma) (Coxall et al., 2005; Taylor et al., 2023). The CCD, below which calcium carbonate ($CaCO_3$) is no longer preserved, reflects the ocean's carbonate saturation state that adjusts on ~4-kyr e-folding timescales to balance the ocean alkalinity budget (Hain et al., 2024). The EOT CCD deepening roughly doubled the seafloor $CaCO_3$ deposition area (Rea & Lyle, 2005), implying a significant imbalance in carbonate sources and sinks.

The favored EOT carbon cycle perturbation mechanism is "shelf-basin fractionation," or repartitioning of $CaCO_3$ burial from the shallow to the deep ocean due to ~75 m sea level fall (Armstrong McKay et al., 2016; Coxall & Wilson, 2011; Merico et al., 2008; Miller et al., 2020; Opdyke & Wilkinson, 1988). Box models require an ~80% reduction in global neritic $CaCO_3$ burial and a $CaCO_3$ weathering pulse to match the CCD deepening (Armstrong McKay et al., 2016; Merico et al., 2008). Such changes in global $CaCO_3$ burial and weathering are expected to impact the concentration and isotopic composition of strontium (Sr) in seawater. We investigated the impact of EOT sea level fall and shelf-to-basin repartitioning of $CaCO_3$ burial on the stable Sr isotopic composition ($\delta^{88/86}$Sr) of seawater, which has been shown to respond to secular changes in neritic $CaCO_3$ burial and weathering over the past 35 Ma (Paytan et al., 2021).

Strontium enters the ocean by rivers, groundwater, release from the oceanic crust, and diagenetic alteration of marine sediments, and is removed by $CaCO_3$ burial in the shal-

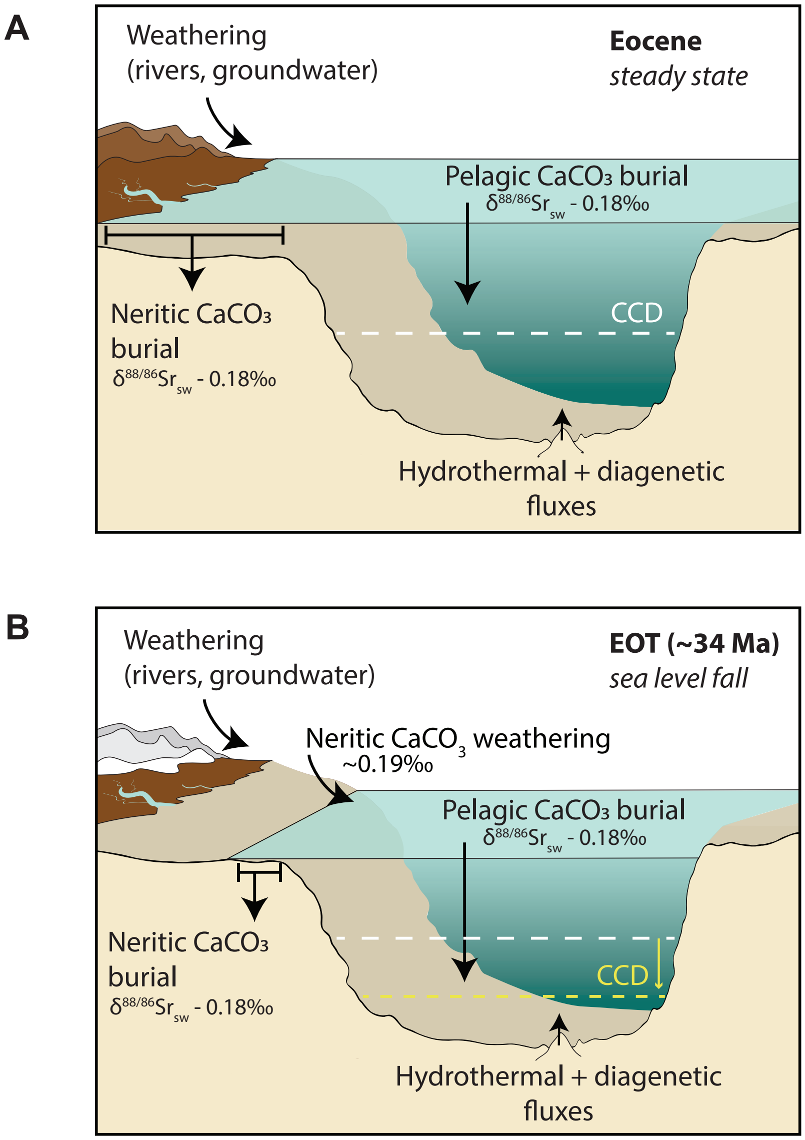

Figure 5.1: (**A**) Steady state sources and sinks of Sr in the Eocene ocean. (**B**) Hypothesized perturbation of the ocean Sr fluxes by the shelf-basin fractionation mechanism. The isotopic fractionation of $\delta^{88/86}$Sr between seawater and carbonate raises the possibility that changes in the neritic carbonate burial and weathering fluxes could impact seawater $\delta^{88/86}$Sr at the EOT, depending on the timescale of the perturbation and the mineralogy of the neritic carbonate fluxes.

low and deep ocean (Figure 5.1A). Preferential incorporation of ^{86}Sr over ^{88}Sr in CaCO$_3$ means that increased (*decreased*) Sr removal from the ocean due to increased (*decreased*) CaCO$_3$ burial will drive seawater $\delta^{88/86}$Sr to higher (*lower*) values, while increased CaCO$_3$ weathering will both increase the supply of isotopically-light Sr to the ocean (Krabbenhöft et al., 2010; Paytan et al., 2021) and increase the oceanic CaCO$_3$ burial flux. Sea level fall reduces shelf area and shallow CaCO$_3$ burial while increasing weathering from exposed shelf CaCO$_3$ sediments, lowering seawater $\delta^{88/86}$Sr until deep ocean CaCO$_3$ burial has compensated for the weathering and shelf burial changes (Hain et al., 2024), ocean alkalinity mass balance is reestablished, and Sr burial matches the geologic sources.

The sink and supply of Sr also depend on CaCO$_3$ mineralogy. Aragonite, the dominant form of CaCO$_3$ in the modern shallow ocean, contains ~10x more Sr than calcite which dominates pelagic sediments (Krabbenhöft et al., 2010). Thus, shelf mineralogy determines the magnitude of neritic Sr burial and weathering fluxes (greater for aragonite than calcite) and variable aragonite-calcite partitioning can alter seawater Sr concentration ([Sr]) and $\delta^{88/86}$Sr (Paytan et al., 2021). Secular variations in seawater Mg/Ca suggest a transition from calcite to aragonite seas just prior to the EOT (Sandberg, 1983; Stanley, 2006; Stanley & Hardie, 1998); increasing Mg/Ca throughout the Paleogene implies that the Late Eocene ocean became more favorable for aragonitic producers following a prolonged period of calcite seas throughout the Jurassic and Cretaceous. The timing of this transition is not precisely known relative to the EOT (Stanley, 2006), but the Late Eocene CaCO$_3$ sink mineralogy and ecological turnover are important considerations for Sr cycling in addition to sea level change.

We considered the following scenarios for possible seawater $\delta^{88/86}$Sr responses to the EOT carbon cycle perturbation:

1) Aragonite-calcite shelf-to-basin repartitioning: an efficient aragonite-hosted shelf Sr sink was replaced by a less efficient calcite-hosted deep ocean sink via carbonate compensation, permanently reducing the ocean Sr sink with net zero change in global CaCO$_3$ burial before and after the transient compensation event. The resulting large secular Sr budget deficit would drive a persistent long-term decline in seawater $\delta^{88/86}$Sr.

2) Calcite-calcite shelf-to-basin repartitioning: reduced calcite-hosted shelf Sr burial was

fully balanced by increased deep ocean calcite-hosted Sr burial after carbonate compensation. Seawater $\delta^{88/86}$Sr may decline while the ocean is experiencing a transient budget surplus of alkalinity and low-$\delta^{88/86}$Sr strontium, but the deepening of the lysocline and CCD (Hain & Sigman, 2024) would increase the deep ocean calcite-hosted Sr burial flux to reestablish a balanced Sr budget without a long-term deficit and hence without a secular declining trend in seawater $\delta^{88/86}$Sr.

3) Changes in global silicate weathering may drive changes in seawater $\delta^{88/86}$Sr either by causing an imbalance in the ocean Sr budget (weathering $>$ burial) or via shifting input $\delta^{88/86}$Sr at steady state (Paytan et al., 2021). That is, a secular $\delta^{88/86}$Sr trend may have occurred with changes in geological source $\delta^{88/86}$Sr without a sustained Sr budget imbalance.

The only available record of seawater $\delta^{88/86}$Sr for the late Cenozoic suggests that seawater $\delta^{88/86}$Sr was slightly lower in the Early Oligocene compared to the Late Eocene (Paytan et al., 2021) (Figure 5.2C). Though these few data show long-term $\delta^{88/86}$Sr change, it is possible that this shift occurred rapidly during the EOT coincident with the CCD deepening. We aimed to obtain additional data between 32 and 36 Ma to evaluate whether and at what rate seawater $\delta^{88/86}$Sr responded to the EOT carbon cycle perturbation.

5.3 Methods

We reconstructed seawater $\delta^{88/86}$Sr between 32 and 36 Ma at about 500-kyr or better resolution using marine barite extracted from sediment cores at Integrated Ocean Drilling Program Site U1333 and Ocean Drilling Program Site 1218 in the Equatorial Pacific. We also analyzed coeval bulk $CaCO_3$ samples from Site U1333, which we expect to show similar trends to barite $\delta^{88/86}$Sr in the absence of diagenetic alteration or changes in $CaCO_3$-seawater Sr fractionation. Detailed methodology is provided in Appendix B.

Analyses of $\delta^{88/86}$Sr and radiogenic Sr isotope ratios (^{87}Sr/^{86}Sr) were made by double spike thermal ionization mass spectrometry at GEOMAR Helmholtz Center for Ocean Research Kiel (Germany) using the method detailed by Krabbenhöft et al. (2009). Seawater $\delta^{88/86}$Sr ratios were calculated from barite $\delta^{88/86}$Sr using a constant seawater-

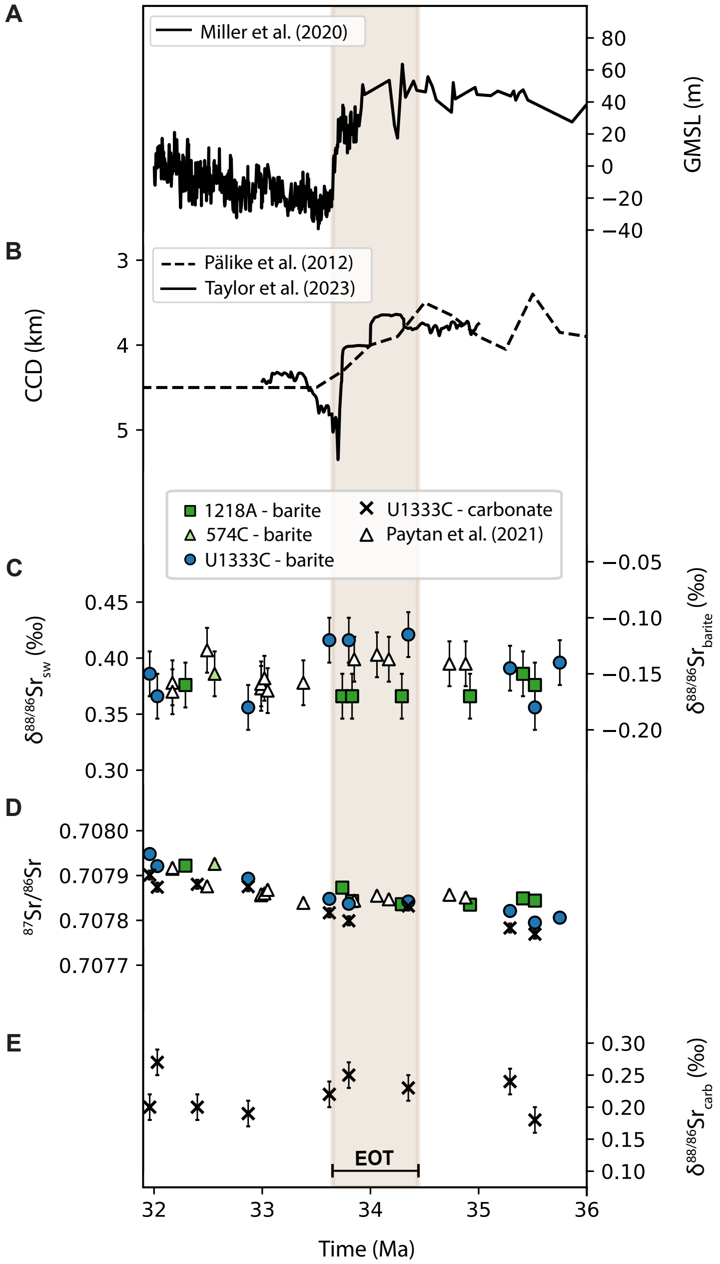

Figure 5.2: (**A**) Global mean sea level (GMSL) (Miller et al., 2020). (**B**) Carbonate compensation depth (CCD) in the equatorial Pacific (Pälike et al., 2012; Taylor et al., 2023). (**C**) Barite $\delta^{88/86}$Sr (*right axis*) from this study and Paytan et al. (2021) at IODP Site U1333, ODP Site 1218, and DSDP Site 574 with inferred seawater $\delta^{88/86}$Sr (*left axis*) calculated by adding the seawater-barite offset of 0.536‰ (Paytan et al., 2021). (**D**) Barite and bulk carbonate ^{87}Sr/^{86}Sr. (**E**) Bulk carbonate $\delta^{88/86}$Sr at IODP Site U1333. Replicate analyses are plotted as the average with error bars given by the long-term external reproducibility. Vertical shading shows the timing of the EOT after Hutchinson et al. (2021).

barite offset of 0.536‰ (Paytan et al., 2021).

5.4 Results

Combined with the published data from Paytan et al. (2021), our $\delta^{88/86}$Sr data show small but statistically insignificant differences in barite $\delta^{88/86}$Sr across the EOT (Figure 5.2C). We observe some variability in barite $\delta^{88/86}$Sr values between sites; specifically, Site U1218 $\delta^{88/86}$Sr values are consistently lower than those from Site U1333 and Site 574 between ~35 and 33.7 Ma (though within error). However, the overall trend across all sites is statistically indistinguishable from a slope of zero (p-value=0.158, Appendix B). We consider one sample from Site U1333 at 32.4 Ma to be an outlier (excluded from Figure 5.2) and the remaining differences between sites to be natural variability consistent with that observed for core-top barite samples (Paytan et al., 2021).

The average seawater $\delta^{88/86}$Sr for the duration of the record, determined by adding a constant offset of 0.536‰ to barite $\delta^{88/86}$Sr values, is 0.38±0.03‰ (mean±2σ). Comparison of the Late Eocene mean $\delta^{88/86}$Sr (0.39±0.04‰) and Early Oligocene mean $\delta^{88/86}$Sr (0.38±0.03‰) confirms that there is no statistically significant difference in seawater $\delta^{88/86}$Sr as recorded in all three cores between these time periods (Appendix B). Similarly, no notable trend is observed in coeval bulk carbonate $\delta^{88/86}$Sr (mean±2σ = 0.22±0.06‰) at Site U1333 (Figure 5.2E). The offset between barite and carbonate $\delta^{88/86}$Sr ($\Delta_{carbonate-barite}$) varies between 0.33‰ and 0.44‰ over the duration of the record, most likely due to post-burial alteration of the primary carbonate composition or possibly due to small local changes in $CaCO_3$-seawater fractionation during this interval as observed for calcium isotopes by Griffith et al. (2011). These data do not suggest any significant change in the $\delta^{88/86}$Sr of the carbonate sink during the carbon cycle perturbation although a small change within error may be inferred (see Appendix B for further discussion).

5.5 Discussion

The lack of trend in seawater $\delta^{88/86}$Sr across the EOT indicates that the mechanism(s) responsible for the CCD change did not significantly alter Sr sources or sinks at the timescale represented by our record. The Sr budget was balanced following carbonate compensation with a maximum 10% contribution from the transfer of low-$\delta^{88/86}$Sr shelf Sr to the ocean allowed by the analytical uncertainty (0.02‰).

Our data suggest that any shelf-to-basin shift in $CaCO_3$ burial was not associated with a major change in the global proportion of aragonite to calcite in the ocean. For a shelf that is two-thirds aragonite (Krabbenhöft et al., 2010), an 80% loss of shallow $CaCO_3$ burial would result in a permanent Sr mass imbalance of approximately 50 Gmol yr^{-1} after carbonate compensation, changing seawater [Sr] by +13% and $\delta^{88/86}$Sr by -0.02‰ over 500 kyr (for modeling, see Appendix B). A pulse of $CaCO_3$ weathering would exacerbate the persistent Sr budget imbalance causing +22% seawater [Sr] and -0.03‰ $\delta^{88/86}$Sr over the course of 500 kyr. Such a systematic trend in seawater $\delta^{88/86}$Sr is not apparent in our data. In this scenario, deep ocean calcite-associated Sr burial balances only ∼10% of the loss of the shallow Sr sink, so the mass imbalance is sustained after the CCD deepening; the full magnitude of the $\delta^{88/86}$Sr response would depend on the duration of the Sr budget imbalance and the initial ocean Sr inventory.

Instead, our reconstruction is consistent with calcite-calcite shelf-to-basin repartitioning, which allows for a shelf-to-basin shift of $CaCO_3$ burial without significant seawater $\delta^{88/86}$Sr change on timescales greater than that of carbonate compensation. That is, the transient excess of alkalinity and low-$\delta^{88/86}$Sr strontium from the loss of shelf calcite burial was balanced by increased deep ocean calcite burial as the lysocline and CCD deepened, restoring the alkalinity and Sr isotope mass balances without driving a secular trend in seawater $\delta^{88/86}$Sr. A pulse of $CaCO_3$ weathering could slightly decrease seawater $\delta^{88/86}$Sr (<0.01‰ over 500 kyr for 100% stepped increase in $CaCO_3$ weathering after Armstrong McKay et al. (2016)) but is not sufficiently large relative to the oceanic Sr inventory to produce a measurable transient change.

Changes in silicate weathering rates during and in the 2 Myr following the EOT are not supported by the seawater $\delta^{88/86}$Sr record. Any variation in weathering fluxes must have remained within 10% of the Sr burial flux while maintaining the long-term Sr isotope mass balance, consistent with explanations that attribute the early Cenozoic rise in ^{87}Sr/^{86}Sr to changes in weathering patterns rather than fluxes (Misra & Froelich, 2012; Ravizza & Peucker-Ehrenbrink, 2003; Zachos et al., 1999). Variable input $\delta^{88/86}$Sr may have driven a secular trend in seawater $\delta^{88/86}$Sr at steady state, which requires balanced rather than constant weathering and burial fluxes, but the net $\delta^{88/86}$Sr of all geological sources must have remained within ± 0.02‰ of the long-term flux or any secular weathering trend was cancelled by changes in the $CaCO_3$ fluxes.

We suggest that Eocene seawater $\delta^{88/86}$Sr was largely insensitive to shelf-to-basin repartitioning of $CaCO_3$ burial due to a calcite-dominated shallow $CaCO_3$ factory. While the secular seawater Mg/Ca trend suggests that the calcite-to-aragonite sea transition occurred before the EOT, paleoecological surveys indicate that aragonitic reef builders had not yet taken hold. Rudists were the dominant reef builders before their extinction at the K-Pg boundary (Stanley, 2005) while reef-building corals remained sparse in the Paleocene and declined following the Paleocene-Eocene boundary (Scheibner & Speijer, 2007), leaving only scattered reef deposits in the Western Tethys throughout the Early-Middle Eocene (Pomar et al., 2017; Tosquella et al., 2022). Tethyan carbonate platforms were instead dominated by calcitic larger benthic foraminifera (LBF) dwelling on carbonate ramps (Coletti et al., 2022; Pomar et al., 2017), rather than modern coral reef tracts that create back-reef habitat and depocenters for fragile aragonite-producers such as *Halimeda*. Although reef development increased starting in the Late Eocene and large coral buildups were present during the formation of ephemeral Antarctic ice sheets in the lead up to the EOT, their main expansion throughout the Tethys was during the Oligocene (Pomar et al., 2017). Modern corals emerged as the dominant reef builders only in the Late Miocene (Pomar & Hallock, 2008).

The EOT $\delta^{88/86}$Sr record demonstrates a significant role for ecological turnover in seawater Sr cycling. Though seawater chemistry implies that the ocean was favorable for aragonite producers around the EOT, aragonite deposition was not yet widespread enough to significantly impact the Sr cycle when perturbed by sea level change. We conclude that only with the development of modern barrier reef systems did the shallow ocean accumulate sufficient aragonite to become the ocean's dominant Sr sink and hence a driver of seawater $\delta^{88/86}$Sr change over the Late Cenozoic, in general agreement with the interpretation of secular variations in seawater $\delta^{88/86}$Sr since the Oligocene by Paytan et al. (2021).

A calcite-dominated shallow Eocene ocean also has implications for the interpretation of a ∼1.0‰ positive excursion in EOT benthic δ^{13}C values (Coxall et al., 2005). Model experiments suggest that weathering of relatively ^{13}C-enriched shelf CaCO$_3$ (∼1.5 to 3‰) is needed to explain the δ^{13}C excursion (Armstrong McKay et al., 2016). These CaCO$_3$ δ^{13}C values imply an aragonite-dominated shallow ocean, since aragonite-rich sediments have higher δ^{13}C values (∼1 to 6‰) compared to pelagic sediments (∼0 to 1‰) (Swart, 2008). Paleorecords of neritic CaCO$_3$ δ^{13}C reach only the latest Oligocene (∼2‰) but show that δ^{13}C is strongly correlated with aragonite content (Swart & Eberli, 2005). Our $\delta^{88/86}$Sr record is more consistent with calcite-dominated neritic sediments that may have had δ^{13}C values like pelagic sediment (∼0 to 1‰), underscoring the need for data on Paleogene neritic CaCO$_3$ δ^{13}C to refine EOT carbon cycle models.

5.6 Conclusions

The EOT record of seawater $\delta^{88/86}$Sr shows that shelf-to-basin repartitioning of CaCO$_3$ burial, considered the best explanation for the observed CCD deepening, did not significantly perturb the ocean Sr budget. Our findings indicate that this mechanism did not involve a major shift in the proportion of aragonite to calcite burial in the ocean and suggest a calcite-dominated shallow CaCO$_3$ factory during the Eocene; aragonitic reef builders were not yet prevalent enough to influence the Sr cycle substantially when perturbed by sea level change. The lack of secular trend in seawater $\delta^{88/86}$Sr further implies that any long-term changes in silicate weathering rates were minimal, maintaining balanced Sr fluxes during this major climate transition. Overall, we have shown that the evolution of the shallow marine CaCO$_3$ factory has important implications for the Sr isotope mass balance and the response of seawater $\delta^{88/86}$Sr to past carbon cycle perturbation.

5.7 Acknowledgements

This work was supported by an International Ocean Discovery Program Schlanger Ocean Drilling Fellowship and graduate research grants from the Geological Society of America, the International Association of Geochemistry, and the Myers Oceanographic and Marine Biology Trust (to MMW).

Appendix A

Supplementary materials for: Glacial/interglacial variations in seawater stable strontium isotope ratios recorded in marine barite

A.1 Marine barite Sr/Ba ratios

In core TTN013-PC83, where we have the most continuous and highest resolution sampling coverage, marine barite Sr/Ba ratios varies systematically between ∼30–40 mmol/mol over the past 250 kyr (Figure A.1). This range of Sr/Ba ratios is similar to the distribution of core top barite Sr/Ba ratios in the Equatorial Pacific and Southern Oceans (24–40 mmol/mol, Averyt & Paytan, 2003), but the systematic changes suggest that this trend is a paleoceanographic signal rather than only natural variability. From 250 to 230 ka, Sr/Ba ratios decreased from ∼40 to 36 mmol/mol, then increased back to 40 mmol/mol by 175 ka. Sr/Ba decreased again to ∼35 mmol/mol by 150 ka followed by a smaller increase to ∼38 mmol/mol at 100 ka, though the data are slightly noisy between 150 and 100 ka. After 100 ka, there was a large decrease to 30 mmol/mol at 50 ka before Sr/Ba ratios increased back to 40 mmol/mol by present-day.

The Sr/Ba record shares some notable similarities with the $\delta^{88/86}$Sr record. First, the two records have similar structures between 250 ka and ~120 ka, a period that spans Marine Isotope Stage (MIS) 7 to MIS 5e (the last interglacial). Both $\delta^{88/86}$Sr and Sr/Ba ratios decreased from 250 to 225 ka, then increased to 200 ka. Increased noise in both records makes the signal between 200 and 120 ka less clear (more so in the $\delta^{88/86}$Sr record), but the dip in Sr/Ba ratios during this period is also reflected in the (more uncertain) $\delta^{88/86}$Sr LOWESS fit. Finally, both $\delta^{88/86}$Sr and Sr/Ba ratios decreased around the Last Interglacial (LIG, ~120 ka).

The $\delta^{88/86}$Sr and Sr/Ba records diverge, however, in the last glacial period. While Sr/Ba ratios decreased from the LIG maximum until 50 ka, $\delta^{88/86}$Sr increased between 66 and 50 ka before decreasing until 33 ka. By 33 ka, Sr/Ba was increasing again and continued to rise until the present day, but $\delta^{88/86}$Sr only increased from 21–14 ka before the trend reversed and $\delta^{88/86}$Sr decreased to the present day. There is no statistically significant correlation between Sr/Ba and $\delta^{88/86}$Sr over the entire duration of the records (Kendall's $\tau = 0.15$, p-value $= 0.11$), indicating no global synchrony between these time series.

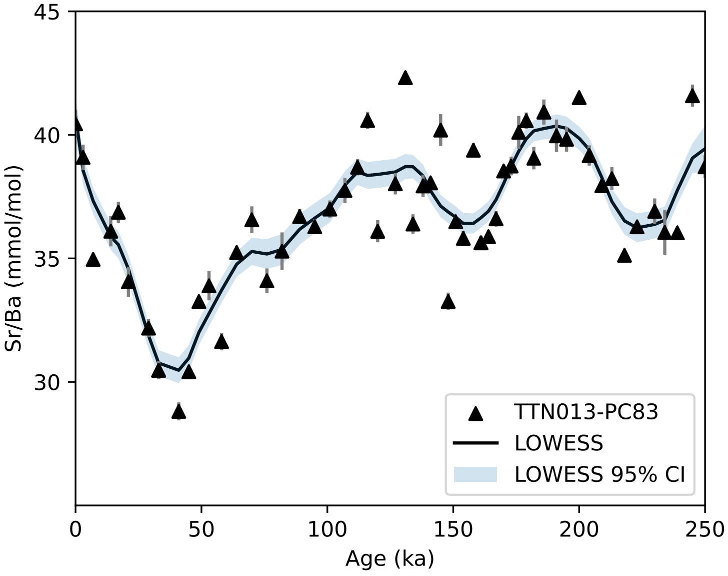

Figure A.1: Marine barite Sr/Ba ratios in core TTN013-PC83 with LOWESS fit. Error bars represent the analytical uncertainty.

Previous work has suggested that changes in marine barite Sr/Ba ratios may be a qualitative indicator of glacial/interglacial seawater [Sr] (Averyt, 2004). The marine barite Sr/Ba data from the TTN013-PC83 sediment core show trends similar to reconstructions of marine barite Sr/Ba ratios in other equatorial Pacific cores (VNTR01-PC8, TTN013-PC72), which revealed Sr/Ba fluctuations at 100-kyr periodicity and were coherent with sea level records over the past 500 kyr (Averyt, 2004). The TTN013-PC83 Sr/Ba record particularly resembles that of TTN013-PC72 (Kendall's τ=0.50, $p<0.001$). At both sites, Sr/Ba ratios increase from minima when glacial sea level drops below ∼-40 to -80 m below present sea level (Figure A.2). Averyt (2004) interpreted the TTN013-PC72 trends as reflecting seawater [Sr] changes due to sea level fluctuations with increased Sr input from recrystallization of exposed shelf carbonate lagging behind the initiation of glaciation. A lagged response to shelf exposure is possible given the time dependence of aragonite recrystallization to calcite, with an approximate decay half life of ∼10–40 ka (Stoll & Schrag, 1998). The VNTR01-PC8 record from Averyt (2004) showed no lag relative to low stands and less pronounced cyclicity compared to their TTN013-PC72 record, which the author attributed to post-depositional processes or local oceanographic variations that muted the response to glacial/interglacial forcing at VNTR01-PC8.

The overall consistency of the trends observed across these sites does suggest that barite Sr/Ba may serve as a qualitative indicator of global seawater [Sr] changes, with additional local effects possibly driving small differences between sites and complicating the relationship between the Sr/Ba and $\delta^{88/86}$Sr proxies. We suggest that the Sr/Ba records provide another line of evidence for sub-Myr variability in the oceanic Sr cycle. However, it remains possible that environmental factors other than seawater [Sr], such as thermodynamics, precipitation rates, or depth of barite formation in the water column, influence the partitioning of Sr in BaSO4, thus limiting our ability to derive quantitative seawater [Sr] estimates from the Sr/Ba records. Partition coefficients for Sr and Ca in marine barite have been empirically defined (Averyt & Paytan, 2003) but require broad assumptions about the consistency of oceanic conditions and the microenvironments of barite formation. We applied the empirical partition coefficient calculated for Sr to our TTN013-PC83 Sr/Ba record to infer the magnitude of seawater [Sr] change from the Sr/Ba variations, with the caveat that the absolute [Sr] values remain uncertain and natural variability of barite Sr/Ba may change through time.

The range of reconstructed barite Sr/Ba over the last glacial cycle (30–40 mmol/mol) implies a seawater [Sr] range of ~83–110 μM ($D_{Sr} = 2.9\text{x}10^{-5}$, Averyt and Paytan (2003)). A 10 mmol/mol increase in barite Sr/Ba (e.g., from ~50 ka to present) would correspond to a 30% increase in [Sr], a greater change than most previous estimates of seawater Sr/Ca variations (1–3%) and seawater [Sr] variations (~10–25%) over similar timescales (Chapter 3, Paytan et al., 2021; Stoll & Schrag, 1998). A ~30% change in seawater [Sr] is however consistent with the [Sr] change predicted by the isotope mass balance of pore fluid $\delta^{88/86}$Sr solutions presented in Chapter 3 Section 5.2. Thus, the magnitude of [Sr] variation remains uncertain though we qualitatively conclude from these multiple lines of evidence that seawater [Sr] measurably varied on 100-kyr timescales. Teasing apart the relative contributions of the background seawater composition versus other environmental factors to barite Sr/Ba ratios may support more quantitative estimates and will require additional records from other oceanographic settings (i.e., beyond the equatorial Pacific) where it would be unlikely for conditions of barite formation (e.g., microenvironment chemistry) to change simultaneously in the same way.

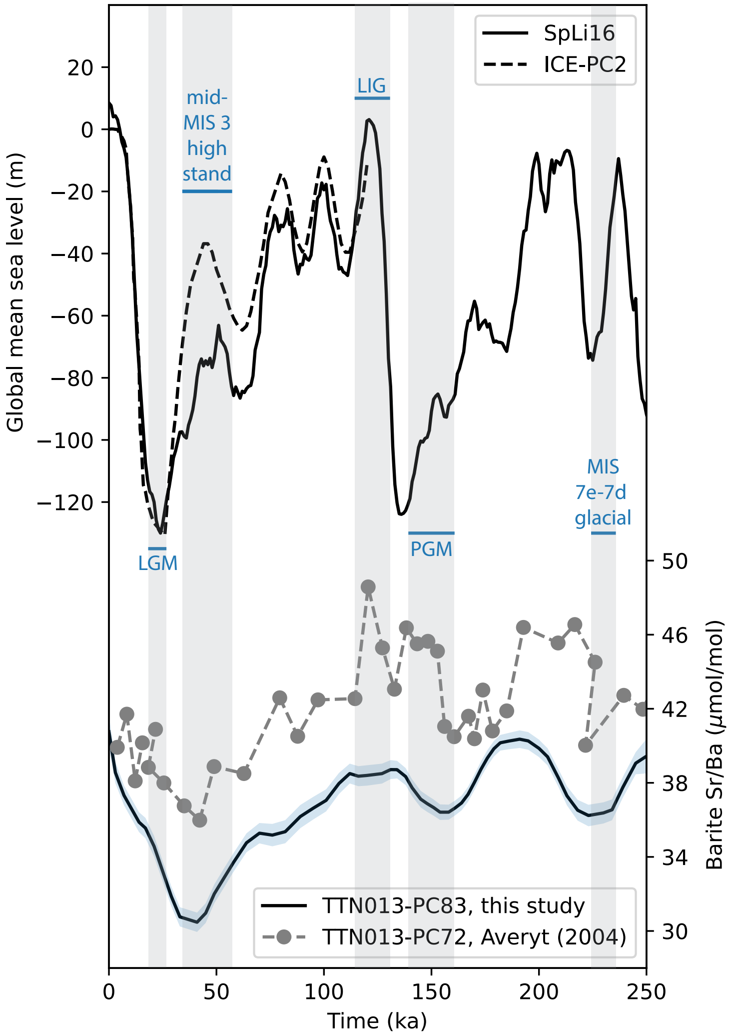

Figure A.2: Marine barite Sr/Ba ratios at TTN013-PC83 (LOWESS fit to the data with the 95% CI given by the shaded ribbon) and TTN013-PC72 (Averyt, 2004) compared to GMSL fluctuations reconstructed from δ^{18}O (solid line, Spratt & Lisiecki, 2016) and GIA modeling (dashed line, Pico et al., 2017). Key transitions are highlighted by vertical shading, including the Last Glacial Maximum (LGM), Last Interglacial (LIG), and Penultimate Glacial Maximum (PGM).

A.2 Modeling seawater $\delta^{88/86}$Sr response to sea level change

The model consists of a well-mixed ocean box coupled to a spatially-resolved continental shelf model (Figure 4.1). For a given eustatic sea level or relative sea level (RSL) history, the model predicts spatially-resolved changes in aragonite burial and recrystallization on continental shelves as a function of paleotopography and calculates the effect of these variable shelf fluxes on the ocean Sr isotope mass balance. The carbonate sink is represented based on best estimates for carbonate burial fluxes in modern neritic environments (e.g., coral reefs, bays, and carbonate-rich shelves) and carbonate hot spots (O'Mara & Dunne, 2019), with the simplifying assumption that shallow carbonate burial changes through time solely as a function of shelf area within neritic habitat depth ranges. We also incorporated a post-glacial pulse of silicate weathering after Mokadem et al. (2015), allowing non-steady state variations in the riverine flux of $<\pm 15\%$ over glacial/interglacial cycles. We forced the model with four different sea level histories to evaluate how the extent and timing of continental shelf flooding and exposure impacts the seawater Sr response to sea level change.

A.2.1 Ocean box model

Sr sources

The box model ocean is a well-mixed reservoir that receives Sr from riverine, groundwater, hydrothermal, and diagenetic sources, plus an additional source from aragonite recrystallization when sea level fall exposes carbonate on the continental shelf. The recrystallization flux depends on RSL and the Sr inventory of the continental shelf, described in more detail in Section A.2.2. The groundwater, hydrothermal, and diagenetic fluxes are based on modern estimates and were assumed constant over a glacial cycle (Table A.1). The riverine flux was allowed to vary by ±15% of the modern flux with the diffuse post-glacial silicate weathering peak modeled by Mokadem et al. (2015).

Non-steady-state silicate weathering

Applying modern Sr fluxes for groundwater, hydrothermal, diagenetic, and riverine sources produces modeled seawater ^{87}Sr/^{87} values that increase at a faster rate (0.000425 Myr^{-1}) than observed over the past few million years (0.000054 Myr^{-1}) (Vance et al., 2009). To address this mismatch, Mokadem et al. (2015) modeled a diffuse post-glacial silicate weathering peak that produced non-steady-state variations in the riverine flux of $<\pm 15\%$ without violating the constraint of the seawater ^{87}Sr/^{87} reconstructions (Figure

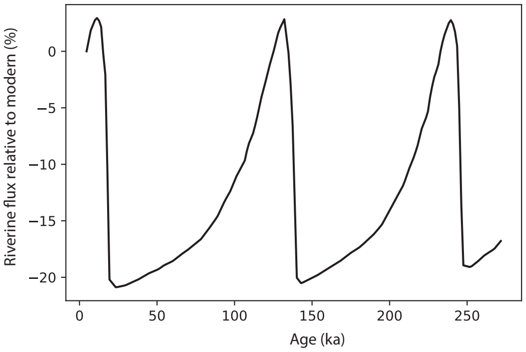

Figure A.3: Weathering forcing from Mokadem et al. (2015).

A.3). We took the variable weathering flux from Mokadem et al. (2015) and similarly applied the variations in our model by dividing the riverine flux into a steady-state component and a non-steady-state component.

As in Mokadem et al. (2015), we assumed 70% of the riverine flux is carbonate weathering with an isotopic composition similar to the average of Phanerozoic limestones (^{87}Sr/^{87} = 0.7080, $\delta^{88/86}$Sr = 0.16‰). Silicate weathering, equal to 30% of the riverine flux, is split into steady-state (30%) and non-steady-state (70%) terms and has an isotopic composition determined by mass balance to achieve a modern riverine flux with ^{87}Sr/^{87} = 0.71144 and $\delta^{88/86}$Sr = 0.317‰ (Mokadem et al., 2015; Paytan et al., 2021; Vance et al., 2009).

Sr sinks

Strontium is removed from the ocean by carbonate burial in the deep sea and shallow ocean. The deep sea is dominated by calcite burial with a lower Sr content (1800 ppm Sr) relative to the the shallow (neritic) sink which we assume is dominantly aragonite (9000 ppm Sr). Though a portion of the neritic non-reef carbonate burial flux is calcite, the partitioning of carbonate burial between aragonitic and calcitic species is uncertain, as are carbonate production and accumulation rates of different species (Krabbenhöft et al., 2010; Milliman, 1993; M. Wood et al., 2023). Previous work has relied on carbonate accumulation rates with large uncertainties and arbitrarily assumed non-reef shelf mineralogy (e.g., 2/3 aragonite, 1/3 calcite) (Krabbenhöft et al., 2010). We based our assumption of shallow mineralogy on recent work that has shown that the pelagic calcite contribution to the total shallow carbonate flux is quite small (0.0013 Pg C yr^{-1}) compared to the benthic contribution which is mainly aragonitic corals and seagrasses (0.163 Pg C yr^{-1}) (O'Mara & Dunne, 2019). We leveraged O'Mara and Dunne's (2019) updated, spatially explicit neritic carbonate accumulation rates for corals, seagrass bays, and carbonate-rich shelves to calculate Sr burial in aragonite within assumed continental shelf depth ranges and hot spot regions (Figure A.4) (described in detail in Section A.2.2). For the deep sea sink, we held the Sr burial flux constant based on the compilation of ^{230}Th-normalized carbonate burial fluxes by M. Wood et al. (2023) that showed no significant difference in the global pelagic carbonate flux between the LGM and Holocene.

Table A.1: Strontium fluxes and isotope values used in the ocean box model. Fluxes that are calculated within the model depend on continental shelf exposure, submerged area with habitat depth ranges, and the isotopic composition of seawater and shelf carbonates at model time *t*.

	Variable	**Sr**	$\delta^{88/86}$**Sr (‰)**	^{87}**Sr/**^{86}**Sr**	Refs
Initial	Seawater	$125\text{x}10^6$ Gmol	0.38	0.70916	1, 2
	Shelf aragonite	$93\text{x}10^4$ Gmol	0.21	0.709	2, 3, 4
Sources	Rivers (F_{riv})	33.7±15% Gmol/yr	0.317	0.71144	1, 2, 5
	Groundwater (F_{gw})	11.5 Gmol/yr	0.3	0.709	1
	Hydrothermal (F_{hyd})	3.1 Gmol/yr	0.24	0.70366	1
	Diagenesis (F_{dia})	3.4 Gmol/yr	0.39	0.7087	1
	Aragonite recryst. ($F_{recryst}$)	*calc.*	*calc.*	*calc.*	
Sinks	Pelagic $CaCO_3$ burial ($F_{calcite}$)	20 Gmol/yr	*calc.*	*calc.*	1
	Neritic $CaCO_3$ burial ($F_{aragonite}$)	*calc.*	*calc.*	*calc.*	

References: 1. Paytan et al. (2021) 2. Mokadem et al. (2015) 3. Hinestrosa et al. (2022) 4. Krabbenhöft et al. (2010) 5. Vance et al. (2009)

Isotope mass balance

The global ocean Sr inventory (Sr_{sw}) and seawater $\delta^{88/86}$Sr (δ_{sw}) were tracked over time according to isotope mass balance:

$$\frac{\Delta Sr_{sw}}{\Delta t} = F_{in} - F_{out} \tag{A.1}$$

$$\frac{\Delta(\delta_{sw} * Sr_{sw})}{\Delta t} = \delta_{in} * F_{in} - \delta_{out} * F_{out} \tag{A.2}$$

where δ_{in} and δ_{out} represent the $\delta^{88/86}$Sr values of the total input (F_{in}) and output fluxes (F_{out}), respectively. The input and output terms of Equation A.2 can be decomposed into the fluxes (F) and $\delta^{88/86}$Sr (δ) for each of the sources and sinks in Table A.1:

$$\delta_{in} * F_{in} = \delta_{riv} * F_{riv} + \delta_{gw} * F_{gw} + \delta_{hyd} * F_{hyd} + \delta_{dia} * F_{dia} + \delta_{recryst} * F_{recryst} \tag{A.3}$$

$$\delta_{out} * F_{out} = \delta_{calcite} * F_{calcite} + \delta_{aragonite} * F_{aragonite} \tag{A.4}$$

The isotopic composition of the output fluxes (calcite and aragonite burial) depends on the $\delta^{88/86}$Sr of seawater and the seawater-carbonate isotope effect (ε = -0.18‰), such that Equation A.4 can be rewritten as:

$$\delta_{out} * F_{out} = (\delta_{sw} + \varepsilon) * (F_{calcite} + F_{aragonite}) \tag{A.5}$$

Likewise, the evolution of seawater ^{87}Sr/^{86}Sr ($^{87}Sr/^{86}Sr_{sw}$) was calculated by:

$$\frac{\Delta(^{87}Sr/^{86}Sr_{sw} * Sr_{sw})}{\Delta t} = {}^{87}Sr/^{86}Sr_{in} * F_{in} - {}^{87}Sr/^{86}Sr_{out} * F_{out} \tag{A.6}$$

The ^{87}Sr/^{86}Sr of the total input ($^{87}Sr/^{86}Sr_{in}$) incorporates the known input flux compositions (Table A.1) and the time-dependent ^{87}Sr/^{86}Sr of recrystallized shelf carbonate, while $^{87}Sr/^{86}Sr_{out}$ is equal to $^{87}Sr/^{86}Sr_{sw}$ (no fractionation of ^{87}Sr/^{86}Sr between seawater and carbonate).

Non-steady-state behavior

By assigning well-constrained estimates for all model fluxes except the shallow carbonate burial and recrystallization fluxes, which are calculated as a function of submerged/exposed shelf area, we consequently did not require that the Sr budget be at steady state. While earlier models have required that carbonate budgets balance over a glacial cycle (Stoll & Schrag, 1998; Walker & Opdyke, 1995), the most recent compilations of deep-sea sedimentary records indicate that global pelagic burial rates did not change substantially over the last glacial cycle to offset sea level-driven changes in shallow carbonate burial (Cartapanis et al., 2018; Hayes et al., 2021; M. Wood et al., 2023). Instead, the ocean carbon and alkalinity inventories may have undergone large changes over the relatively short timescales of glacial/interglacial sea level changes, with important implications for carbonate compensation and atmospheric carbon dioxide concentrations (Cartapanis et al., 2018). Variable input from non-steady-state weathering processes could further exacerbate or offset this imbalance (Vance et al., 2009). We incorporated non-steady-state weathering as allowed by seawater ^{87}Sr/^{86}Sr after Mokadem et al. (2015), but it is not necessarily the case that the weathering input was balanced by the global carbonate output or that all Sr mobilized from the exposed shelf was re-buried within a glacial cycle. The result of the allowed imbalances in Sr sources and sinks is small degree of long-term drift in the seawater Sr inventory and $\delta^{88/86}$Sr. Given the frequency of sea level changes during glacial cycles and the variability in high stand and low stand elevations, it is reasonable to expect that the Sr budget was rarely balanced on 10–100 ka timescales even over an entire cycle. We focus primarily on the timing of transient seawater [Sr] and $\delta^{88/86}$Sr changes with respect to sea level rather than potential secular changes over the Pleistocene, since reasonably constraining the long-term trend will require additional observations over more glacial cycles.

A.2.2 Continental shelf model

The shallow ocean fluxes $F_{aragonite}$ and $F_{recryst}$ are calculated at each model time step by our continental shelf model. The spatially explicit model uses RSL to determine flooded and exposed shelf areas that bury and recrystallize aragonite, respectively.

The shelf model has a spatial resolution of 1°x1° and extends from 45°N to 45°S; we excluded the high latitudes where shallow carbonate accumulation is minimal and marine-terminating ice sheets might impact our shelf exposure calculations during glacial periods. The model tracks the shelf carbonate Sr inventory (Sr_{shelf_i}), $\delta^{88/86}$Sr (δ_{shelf_i}), and ^{87}Sr/^{86}Sr ($^{87}Sr/^{86}Sr_{shelf_i}$) in each grid cell ($shelf_i$) through time by isotope mass balance:

$$\frac{\Delta Sr_{shelf_i}}{\Delta t} = F_{aragonite_i} - F_{recryst_i} \tag{A.7}$$

$$\frac{\Delta(\delta_{shelf_i} * Sr_{shelf_i})}{\Delta t} = (\delta_{sw} + \varepsilon) * F_{aragonite_i} - \delta_{recryst_i} * F_{recryst_i} \tag{A.8}$$

$$\frac{\Delta(^{87}Sr/^{86}Sr_{shelf_i} * Sr_{shelf_i})}{\Delta t} = {}^{87}Sr/^{86}Sr_{sw} * F_{aragonite_i} - {}^{87}Sr/^{86}Sr_{recryst_i} * F_{recryst_i} \tag{A.9}$$

The isotopic composition of $F_{aragonite_i}$ depends on that of seawater at time t (as in Equations A.5 and A.6) while $F_{recryst_i}$ has the ^{87}Sr/^{86}Sr and $\delta^{88/86}$Sr of the recrystallizing shelf carbonate in grid cell $shelf_i$.

At each model time step, $F_{aragonite_i}$ and $F_{recryst_i}$ depend on paleotopography (i.e., whether $shelf_i$ is exposed or submerged), regional neritic carbonate burial fluxes, and the recrystallization rate. One of three conditions will be met: 1) $shelf_i$ is exposed (paleotopography>RSL) and will release Sr to the ocean via aragonite recrystallization, 2) $shelf_i$ is submerged within a defined depth range for aragonite burial (e.g., 0 to 50 meters below sea level (mbsl) for corals) and will remove Sr from the ocean, or 3) $shelf_i$ is submerged at >200 mbsl and remains unchanged. The sum of all shelf grid cell fluxes at model time t yields the global $F_{aragonite}$ and $F_{recryst}$ fluxes used in the ocean model.

Paleotopography

To determine the flooded area and exposure of the continental shelf over a glacial cycle, we predicted paleotopography at 1°x1° spatial resolution using four different sea level histories:

1. Idealized sea level fluctuations between modern day sea level and -120 m below modern sea level (given by a sinusoid)
2. δ^{18}O-derived global mean sea level (GMSL) estimates from Spratt and Lisiecki (2016) (SpLi16, Figure A.5)
3. Glacial isostatic adjustment (GIA) model estimates of RSL based on the ICE-PC2 global ice history (Pico et al., 2017) (ICE-PC2, Figure A.6). The ICE-PC2 ice history extends only to 122 ka, so we replicate the last glacial cycle back in time to model 244 kyr.

4. GIA model estimates of RSL based on a combination of the ICE-PC2 global ice history (Pico et al., 2017) (0–122 ka) and the Spratt and Lisiecki (2016) GMSL reconstruction (122–250 ka). The SpLi16 GMSL curve was used to extend ICE-PC2 and approximate an ice volume history for the penultimate glacial cycle. The reconstructed ice sheet history for 122–250 ka assumes that whenever GMSL is a certain value, the ice sheets have the same configuration as for the same GMSL during the past deglaciation.

The paleotopography of each grid cell at model time t was found by subtracting the RSL at time t from modern bathymetry (Figure A.4). For the GMSL histories (sinusoid and SpLi16), RSL is equal to GMSL everywhere. For the RSL histories (ICE-PC2, ICE-PC2-SpLi16), each grid cell experiences local paleotopography changes depending on glacial isostatic adjustment.

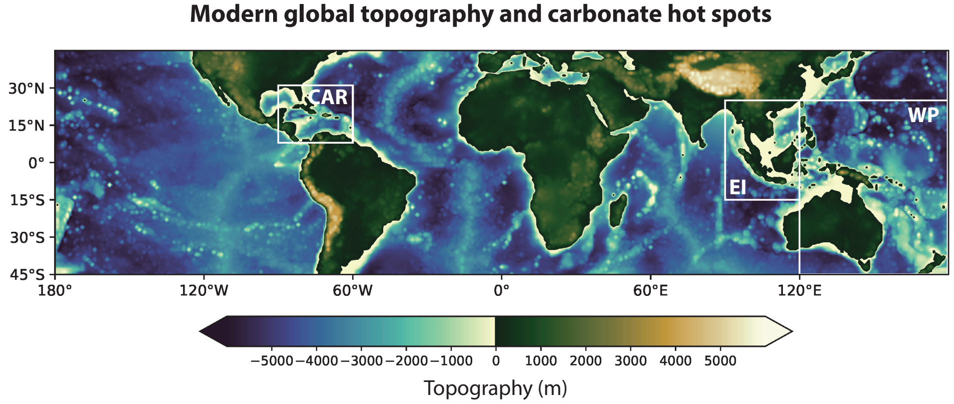

Figure A.4: Modern topography from the "ETOPO 2022 15 Arc-Second Global Relief Model" (2022) and carbonate hot spot regions identified by O'Mara and Dunne (2019): Western Pacific (WP), Eastern Indian (EI) and Caribbean (CAR).

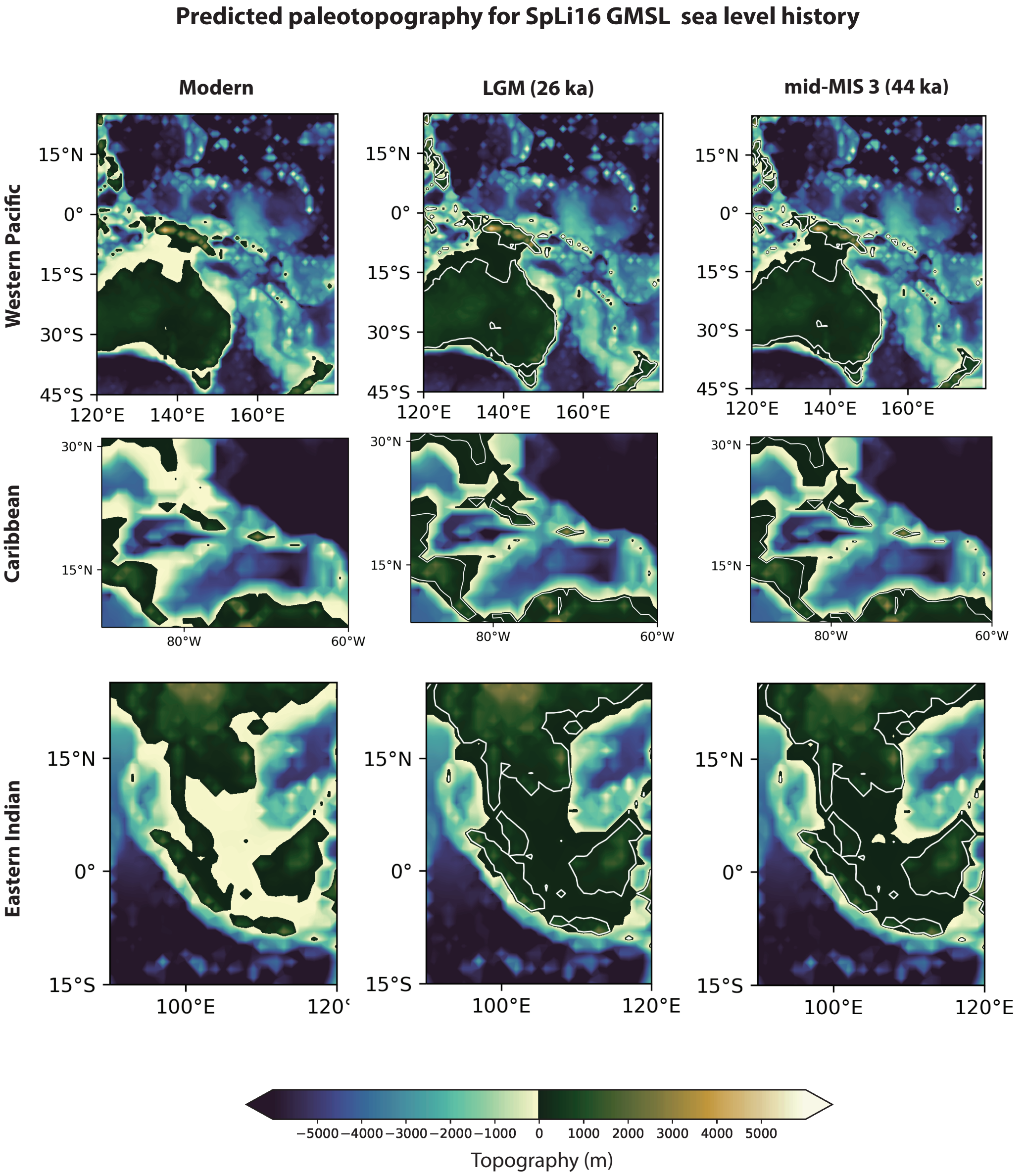

Figure A.5: Modern topography and predicted paleotopography based on the SpLi16 sea level history at the LGM and MIS 3 high stand in three hot spot regions for shallow carbonate burial. The modern shoreline is shown by the white line on the paleotopography maps.

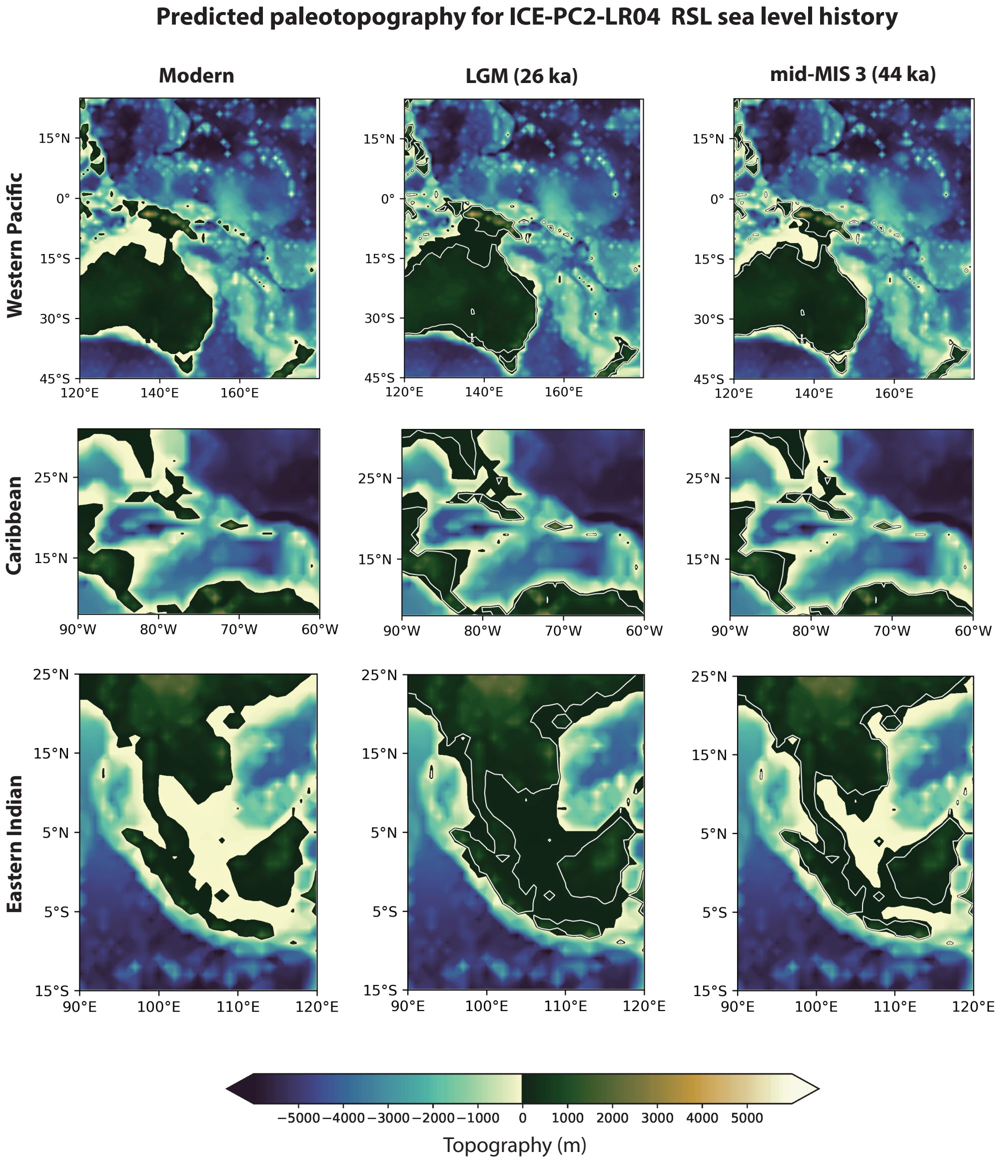

Figure A.6: Modern topography and predicted paleotopography based on the ICE-PC2 sea level history at the LGM and MIS 3 high stand in three hot spot regions for shallow carbonate burial. The modern shoreline is shown by the white line on the paleotopography maps.

Neritic carbonate recrystallization

The recrystallization of aragonite to calcite results from subaerial exposure of carbonate shelves by RSL fall and releases Sr to the ocean. In the model, $F_{recryst_i}$ depends on Sr_{shelf_i} and the half decay time for recrystallization ($\tau_{1/2}$) :

$$F_{recryst_i} = \frac{-ln2}{\tau_{1/2}} * Sr_{shelf_i} \tag{A.10}$$

We ran our simulations with a maximum $\tau_{1/2}$ of 20 kyr and minimum of 5 kyr to capture the sensitivity of the seawater Sr response to this parameter. Up to 90% of the shelf inventory was allowed to be recrystallized, simulating the conversion of Sr-rich aragonite to Sr-poor calcite.

Table A.2: Total modern carbonate accumulation (Pg $CaCO_3$ yr^{-1}) in neritic environments for model regions (O'Mara and Dunne, 2019).

Region	Corals (0 to -50 m)	Bays (0 to -50 m)	$CaCO_3$ shelves (0 to -200 m)
Western Pacific	0.37	0.10	0.11
Eastern Indian	0.11	0.04	0.03
Caribbean	0.07	0.07	0.05
Other	0.14	0.15	0.11
Total	**0.7**	**0.36**	**0.31**

Neritic carbonate burial

We leveraged the spatially explicit neritic carbonate budget by O'Mara and Dunne (2019) to parameterize $F_{aragonite}$ in our model. Neritic carbonate accumulation is unevenly distributed across modern continental shelves in a complex mosaic of neritic environments that remains poorly quantified and difficult to model (Husson et al., 2018; Kleypas, 1997; M. Wood et al., 2023). Fortunately, for the purpose of these simulations it was not critical to capture the precise magnitude or location of these fluxes but rather to approximate changes associated with RSL variations. We chose to define three "hot spot" regions of carbonate accumulation after O'Mara and Dunne (2019): Western Pacific (120°E to 180, 25°N to 45°S), Eastern Indian (90°E to 120°E, 25°N to 15°S), and Caribbean (90°W to 60°W, 8°N to 31°N) (Figure A.4). We assigned carbonate burial rates for each of three depositional environments (corals, bays, and carbonate-rich shelves) based on the fractional contribution of each region to the global flux (Table A.2). The depositional environments are defined by depth ranges in the model: corals and bays cover shelf areas from 0 to 50 mbsl, while carbonate shelves are shallower than 200 mbsl. This approach maintained a degree of spatial heterogeneity in carbonate accumulation while achieving regional average fluxes that were readily incorporated into our model framework.

Our strategy achieves a global interglacial carbonate burial flux in the model that matches modern estimates and is broadly representative of the relative contributions of each neritic environment type and hot spot region. The model assumes that changes in shelf area (as determined by RSL) is the only driver of changes in neritic carbonate burial on glacial/interglacial timescales, though there are many secondary factors that can influence carbonate production and accumulation rates (e.g., water temperature, light, nutrients, saturation state, reef morphology, vertical vs. horizontal reef growth). We also assumed that the LGM substrate depths are approximately the same as the present-day shelf bathymetry, neglecting any changes in sediment thickness which are generally small (Hinestrosa et al., 2022).

A.3 Supplemental tables and figures

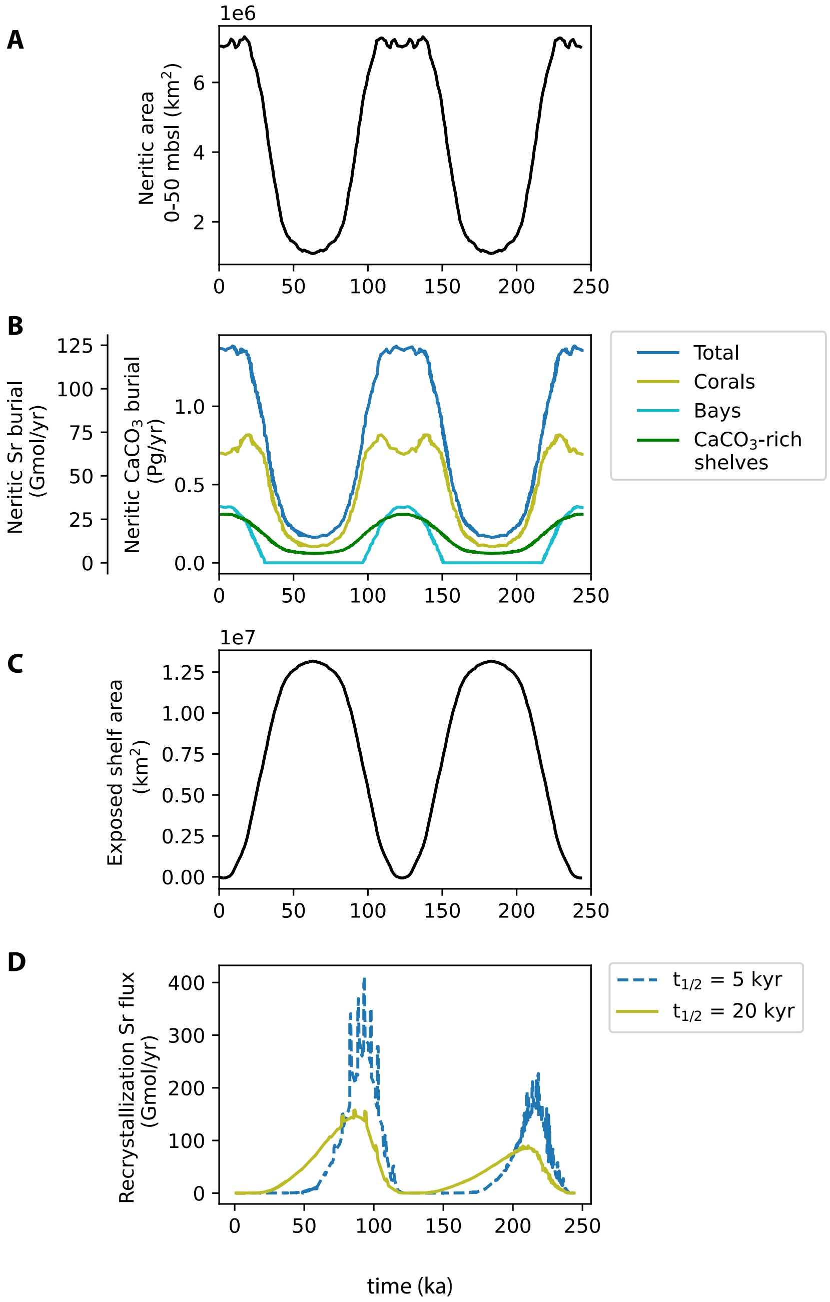

Figure A.7: For the sinusoidal sea level simulations (SINE-F, SINE-S): (**A**) Shelf area submerged between 0–50 m (assumed coral reef and bay depth range), (**B**) Calculated shallow carbonate (Sr) burial fluxes, (**C**) Shelf area exposed above sea level relative to present day, (**D**) Calculated aragonite recrystallization fluxes for decay half-lives of 5 kyr (SINE-F) and 20 kyr (SINE-S).

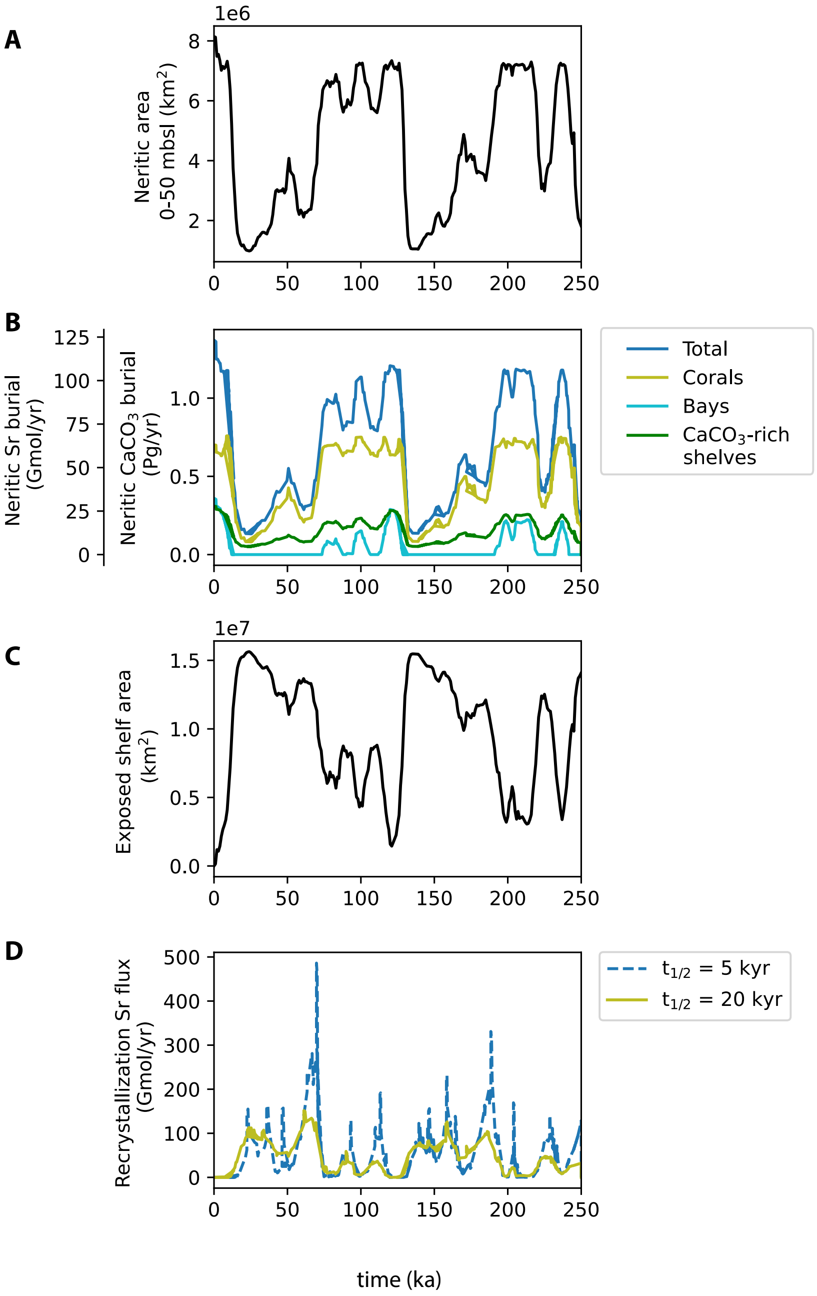

Figure A.8: For the global mean sea level simulations (GMSL-F, GMSL-S): (**A**) Shelf area submerged between 0–50 m (assumed coral reef and bay depth range), (**B**) Calculated shallow carbonate (Sr) burial fluxes, (**C**) Shelf area exposed above sea level relative to present day, (**D**) Calculated aragonite recrystallization fluxes for decay half-lives of 5 kyr (GMSL-F) and 20 kyr (GMSL-S).

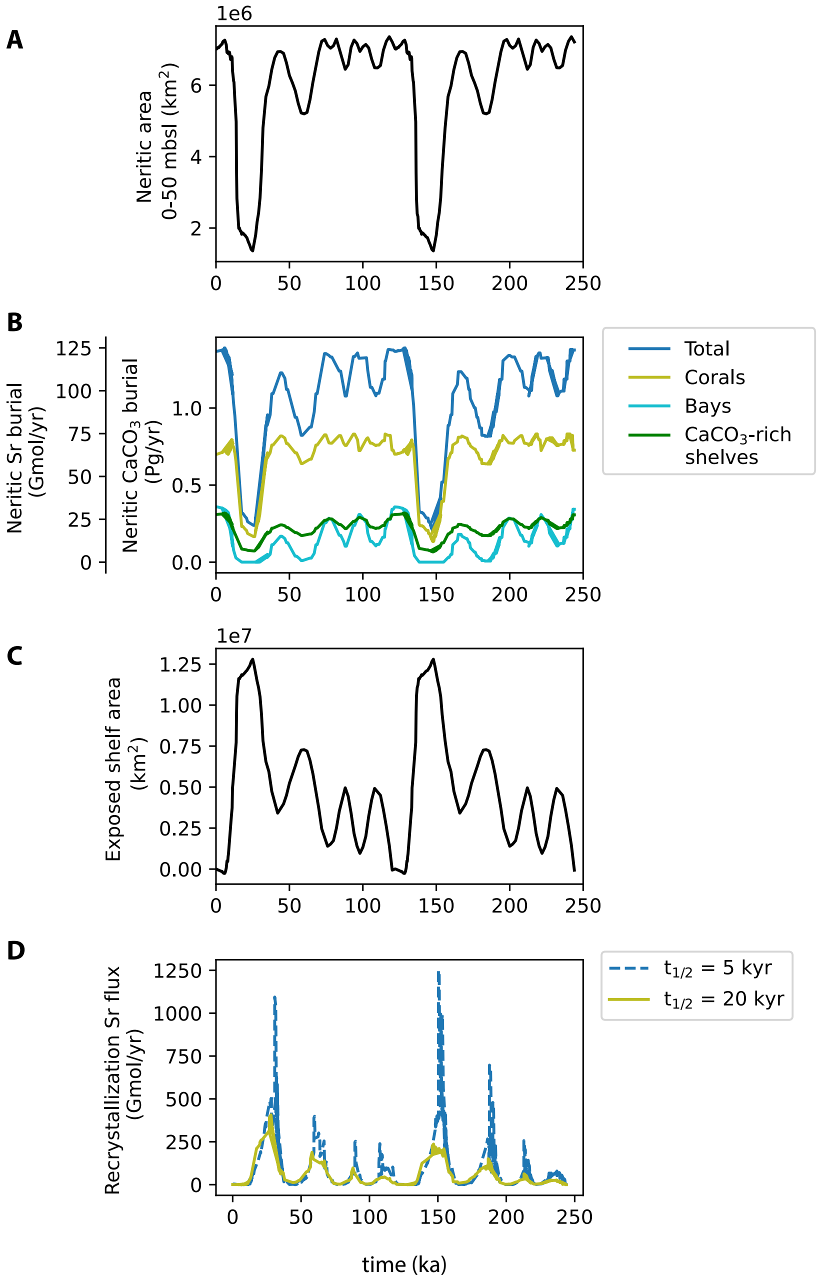

Figure A.9: For the relative sea level simulations (ICEPC2-F, ICEPC2-S): (**A**) Shelf area submerged between 0–50 m (assumed coral reef and bay depth range), (**B**) Calculated shallow carbonate (Sr) burial fluxes, (**C**) Shelf area exposed above sea level relative to present day, (**D**) Calculated aragonite recrystallization fluxes for decay half-lives of 5 kyr (ICEPC2-F) and 20 kyr (ICEPC2-S).

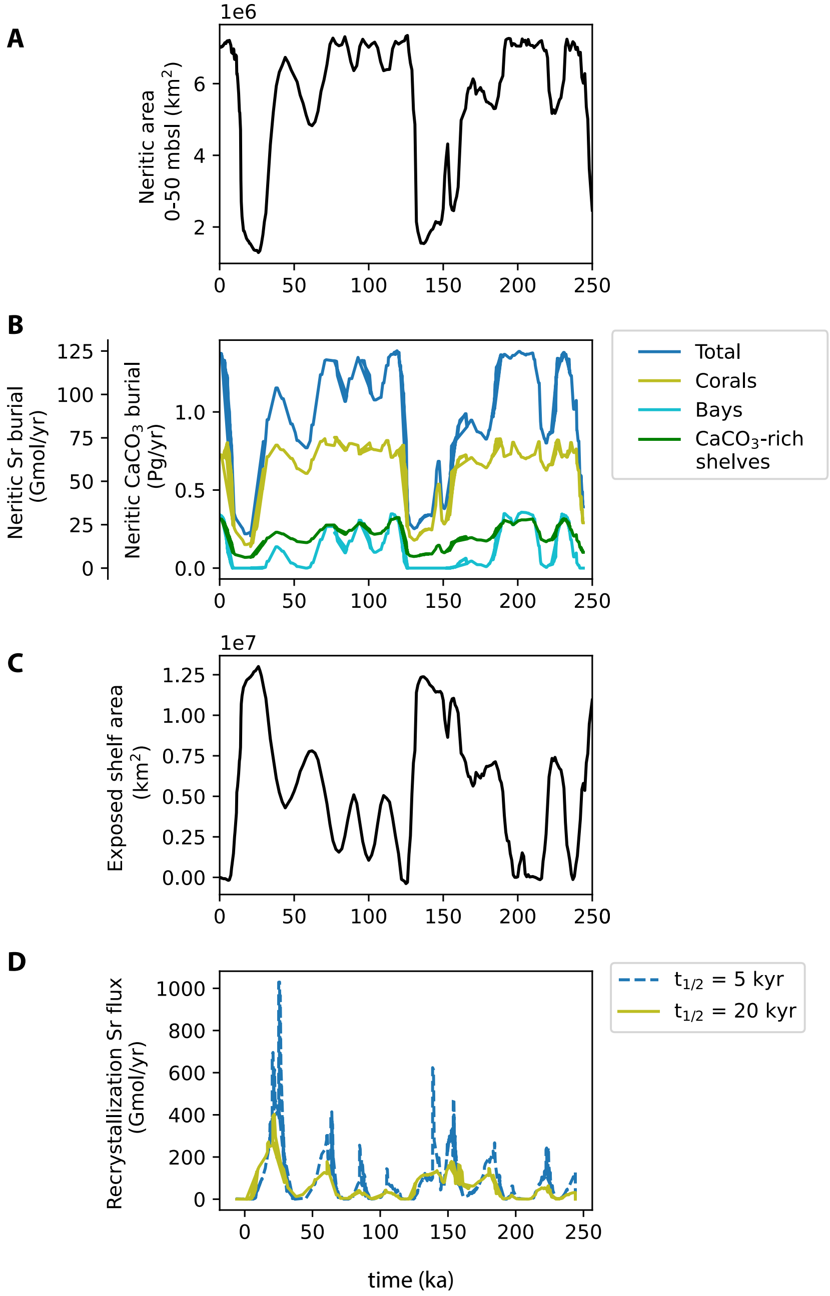

Figure A.10: For the relative sea level simulations (ICE-PC2-SpLi16-F, ICE-PC2-SpLi16-S): (**A**) Shelf area submerged between 0–50 m (assumed coral reef and bay depth range), (**B**) Calculated shallow carbonate (Sr) burial fluxes, (**C**) Shelf area exposed above sea level relative to present day, (**D**) Calculated aragonite recrystallization fluxes for decay half-lives of 5 kyr (ICE-PC2-SpLi16-F) and 20 kyr (ICE-PC2-SpLi16-S).

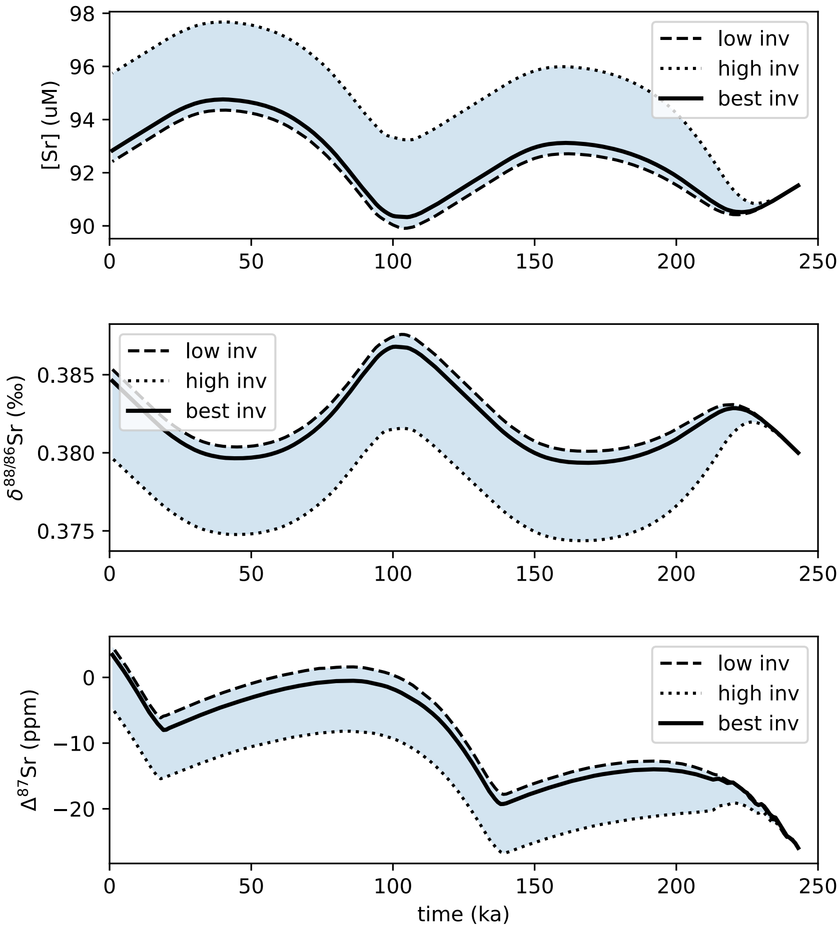

Figure A.11: Idealized sea level forcing (sine wave) sensitivity to initial Sr inventory of the continental shelf with a recrystallization half decay time of 10 kyr.

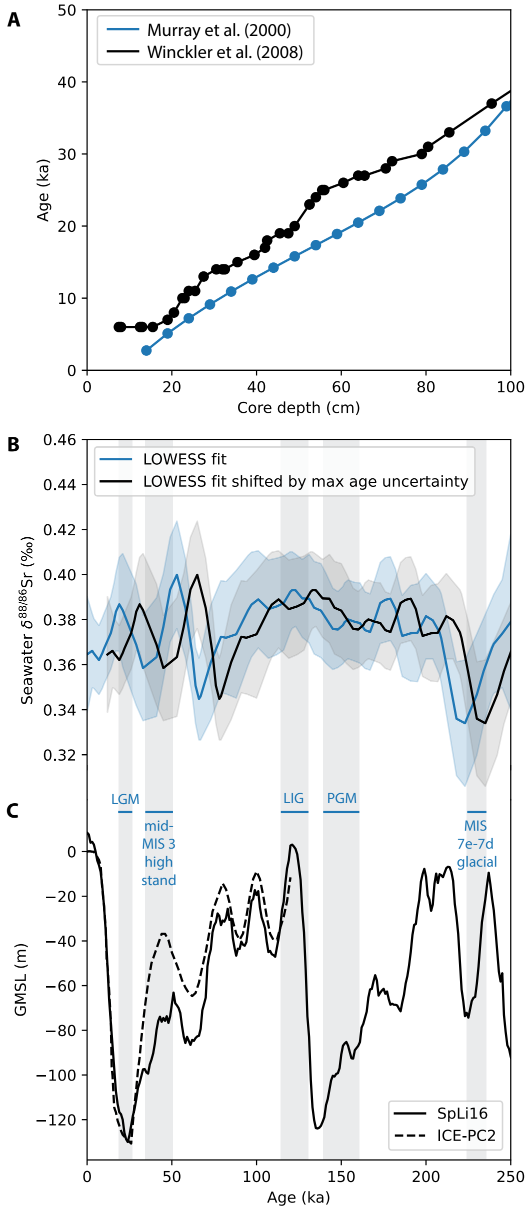

Figure A.12: **(A)** 14C ages from Winckler et al. (2008) show that the age model of Murray et al. (2000) for core TTN013-PC72 is biased toward younger ages by ∼2–7 kyr in the upper 100 cm. **(B)** and **(C)** Shifting the observed $\delta^{88/86}$Sr trends (plotted here as the LOWESS fit to our $\delta^{88/86}$Sr measurements) by our maximum estimated age uncertainty significantly shifts the timing of $\delta^{88/86}$Sr maxima and minima relative to sea level changes (see main text for discussion).

Table A.3: Stable and radiogenic strontium isotope ratios, strontium concentrations, and barium concentrations measured in marine barite samples from cores TTN013-PC83, TTN013-PC72, and VNTR01-PC8. Replicate samples are denoted by asterisks. Reported errors are the internal precision of each measurement.

Core	**Depth (cm)**	**Age (ka)**	$\delta^{88/86}$**Sr (‰)**	$\mathbf{2}\sigma_{mean}$	**n**	^{87}**Sr/**^{86}**Sr**	$\mathbf{2}\sigma_{mean}$	**Sr (ppm)**	**RSD**	**Ba (ppm)**	**RSD**
TTN013-PC83	0-3	0	-0.153	0.001	4	0.709151	0.000001	10.49	0.9	406	1.0
	3-6	3	-0.171	0.012	4	0.709165	0.000015	8.07	0.3	324	1.3
	6-9	7	-0.139	0.007	4	0.709147	0.000002	5.80	0.4	260	0.3
	12-15	14	-0.139	0.003	4	0.709151	0.000001	7.55	1.5	328	0.9
	15-18	17	-0.148	0.002	4	0.709159	0.000004	8.10	0.2	344	1.1
	18-20	21	-0.149	0.002	2	0.709168	0.000002	8.13	1.6	374	0.8
	24-27	29	-0.163	0.001	2	0.709170	0.000001	6.01	1.1	293	0.4
	27-30	33	-0.174	0.009	4	0.709161	0.000001	9.11	1.1	468	0.5
	27-30*	33	-0.189	0.001	4	0.709157	0.000002	9.11	1.1	468	0.5
	33-36	41	-0.177	0.002	4	0.709164	0.000006	4.40	0.1	239	1.3
	36-39	45	-0.167	0.008	4	0.709158	0.000005	5.72	0.4	295	0.1
	39-42	49	-0.129	0.001	4	0.709164	0.000000	5.37	0.3	253	0.4
	42-45	53	-0.132	0.009	4	0.709166	0.000001	5.97	0.8	276	1.5
	45-48	58	-0.139	0.013	4	0.709171	0.000001	7.05	0.7	349	0.9
	48-51	64	-0.188	0.009	4	0.709157	0.000000	7.12	0.2	317	0.6
	48-51*	64	-0.167	0.002	4	0.709154	0.000003	7.12	0.2	317	0.6
	51-54	70						7.48	0.1	320	1.5
	54-57	76						6.78	1.3	312	0.8

Continued on next page

Table A.3 – continued from previous page

Core	**Depth (cm)**	**Age (ka)**	$\delta^{88/86}$**Sr (‰)**	$2\sigma_{mean}$	**n**	^{87}**Sr/**^{86}**Sr**	$2\sigma_{mean}$	**Sr (ppm)**	**RSD**	**Ba (ppm)**	**RSD**
	57-60	82						5.82	1.3	259	1.7
	60-63	89						7.97	0.5	341	0.7
	63-66	95	-0.167	0.001	4	0.709155	0.000003	6.59	0.8	285	0.3
	66-69	101	-0.149	0.006	4	0.709165	0.000015	6.56	0.4	278	0.9
	69-72	107	-0.148	0.003	4	0.709160	0.000003	8.25	0.2	342	1.3
	72-75	112	-0.163	0.012	4	0.709160	0.000003	8.85	0.6	358	0.6
	75-78	116	-0.137	0.009	4	0.709163	0.000007	8.17	0.9	316	0.1
	78-81	120	-0.163	0.001	4	0.709165	0.000004	6.96	0.8	302	1.0
	81-84	123	-0.139	0.004	4	0.709145	0.000003	6.08	0.6	179	0.3
	81-84*	123	-0.156	0.006	4	0.709164	0.000000	6.08	0.6	179	0.3
	84-87	127	-0.155	0.012	4	0.709148	0.000001	6.72	0.7	277	0.9
	87-90	131	-0.179	0.005	4	0.709153	0.000008	9.55	0.5	354	0.3
	90-93	134	-0.121	0.003	4	0.709175	0.000003	7.05	0.1	304	1.1
	93-96	138	-0.162	0.002	4	0.709160	0.000001	8.60	0.9	355	0.8
	96-99	141	-0.157	0.004	4	0.709171	0.000006	6.09	0.6	251	0.3
	99-102	145	-0.163	0.012	4	0.709152	0.000002	8.38	1.0	327	1.2
	102-105	148	-0.175	0.001	4	0.709157	0.000002	6.33	0.4	298	1.0
	105-108	151	-0.147	0.004	4	0.709156	0.000001	11.11	0.6	477	0.1
	108-111	154	-0.159	0.004	4	0.709155	0.000005	9.31	0.7	407	0.5
	111-114	158	-0.129	0.004	4	0.709154	0.000001	10.37	0.6	413	0.4
	114-117	161	-0.160	0.011	4	0.709155	0.000003	6.13	0.3	270	0.6

Continued on next page

Table A.3 – continued from previous page

Core	**Depth (cm)**	**Age (ka)**	$\delta^{88/86}$**Sr (‰)**	**2**σ_{mean}	**n**	^{87}**Sr/**^{86}**Sr**	**2**σ_{mean}	**Sr (ppm)**	**RSD**	**Ba (ppm)**	**RSD**
	114-117*	161	-0.171	0.004	4	0.709146	0.000001	6.13	0.3	270	0.6
	117-120	164	-0.173	0.02	4	0.709147	0.000003	7.37	0.5	322	0.3
	120-123	167	-0.148	0.012	4	0.709148	0.000000	9.41	0.7	403	0.6
	123-126	170	-0.157	0.001	4	0.709150	0.000001	12.38	0.2	503	0.6
	126-129	173	-0.142	0.005	4	0.709143	0.000000	8.97	0.3	363	0.9
	129-132	176	-0.126	0.004	4	0.709154	0.000002	10.49	0.8	410	1.4
	132-135	179	-0.140	0.003	2	0.709152	0.000000	8.78	0.5	339	0.6
	135-138	182	-0.174	0.004	4	0.709147	0.000004	10.35	0.7	415	0.9
	138-141	186	-0.155	0.009	4	0.709151	0.000004	6.06	0.8	232	0.9
	138-141*	186	-0.169	0.006	4	0.709151	0.000000	6.06	0.8	232	0.9
	141-144	191	-0.192	0.002	2	0.709152	0.000006	20.16	0.8	791	1.4
	144-147	195	-0.141	0.01	4	0.709156	0.000005	10.06	0.5	396	1.1
	147-150	200	-0.147	0.008	4	0.709161	0.000004	12.38	0.6	467	0.2
	150-153	204	-0.155	0.008	4	0.709153	0.000005	7.72	0.4	309	0.9
	150-153*	204	-0.172	0.01	4	0.709154	0.000001	7.72	0.4	309	0.9
	153-156	209	-0.139	0.005	4	0.709164	0.000003	6.62	0.6	273	0.4
	156-159	213	-0.191	0.001	4	0.709137	0.000003	7.95	1.1	326	0.4
	159-162	218	-0.204	0.005	4	0.709147	0.000006	8.78	0.4	392	0.3
	162-165	223	-0.207	0.002	4	0.709144	0.000005	6.97	0.0	301	0.3
	166-168	230	-0.187	0.004	4	0.709141	0.000004	8.70	0.5	369	1.3
	168-171	234	-0.183	0.007	4	0.709149	0.000006	6.66	2.4	290	1.0

Continued on next page

Table A.3 – continued from previous page

Core	**Depth (cm)**	**Age (ka)**	$\delta^{88/86}$**Sr (‰)**	**2**σ_{mean}	**n**	^{87}**Sr/**^{86}**Sr**	**2**σ_{mean}	**Sr (ppm)**	**RSD**	**Ba (ppm)**	**RSD**
	171-174	239	-0.156	0.004	2	0.709145	0.000004	8.95	0.2	389	0.4
	174-177	245	-0.164	0.005	4	0.709143	0.000003	11.30	0.5	426	1.0
	177-180	250	-0.157	0.005	4	0.709140	0.000005	9.26	0.4	375	1.1
TTN013-PC72	46-48	19	-0.150	0.007	4	0.709154	0.000002	1.54	0.9	77	1.4
	156-158	67	-0.230	0.001	2	0.709150	0.000003	3.91	0.8	185	1.5
	166-168	73	-0.160	0.004	4	0.709167	0.000002	8.41	0.5	398	1.5
	176-178	79	-0.160	0.006	4	0.709160	0.000003	6.38	0.6	260	0.4
	186-188	88	-0.160	0.007	4	0.709154	0.000009	12.86	1.3	551	1.7
	196-198	97	-0.130	0.003	4	0.709149	0.000004	6.65	1.0	292	1.2
	206-208	107	-0.150	0.009	4	0.709154	0.000002	12.37	0.3	507	1.0
	226-228	121	-0.120	0.002	4	0.709151	0.000004	13.25	0.3	477	0.5
	236-238	127	-0.120	0.004	4	0.709150	0.000001	8.93	0.4	291	0.6
	284-286	152	-0.170	0.008	4	0.709156	0.000010	2.89	0.5	106	0.8
	334-336	170	-0.180	0.004	4	0.709152	0.000001	4.31	1.0	172	1.0
	364-366	185	-0.140	0.007	4	0.709160	0.000003	4.51	0.6	163	0.5
	394-396	208	-0.157	0.013	4	0.709157	0.000001	5.70	0.4	200	0.1
	444-446	240	-0.172	0.004	4	0.709158	0.000000	2.40	0.1	95	0.5
VNTR01-PC8	0-2	0	-0.186	0.006	4	0.709173	0.000013	2.35	0.1	95	0.5
	8-10	4	-0.179	0.003	4	0.709170	0.000001	7.49	0.2	259	0.4
	15-17	7	-0.164	0.007	4	0.709167	0.000004	28.68	0.4	706	1.1
	20-22	9	-0.195	0.009	4	0.709164	0.000007	7.80	0.3	271	0.8

Continued on next page

Table A.3 – continued from previous page

Core	**Depth (cm)**	**Age (ka)**	$\delta^{88/86}$**Sr (‰)**	$2\sigma_{mean}$	**n**	^{87}**Sr**/^{86}**Sr**	$2\sigma_{mean}$	**Sr (ppm)**	**RSD**	**Ba (ppm)**	**RSD**
	22-24	10	-0.212	0.011	4	0.709157	0.000005	1.59	0.2	57	0.6
	35-37	16	-0.156	0.007	4	0.709175	0.000002	33.93	1.2	921	1.1
	152-154	62	-0.179	0.004	4	0.709163	0.000000	12.07	0.3	444	0.5
	162-174	66	-0.193	0.003	4	0.709158	0.000007	13.03	0.6	462	0.8
	202-204	82	-0.170	0.009	4	0.709162	0.000003	2.70	0.1	122	0.1
	352-354	146	-0.150	0.005	4	0.709168	0.000005	3.36	0.1	119	0.3
	552-554	200	-0.160	0.012	4	0.709160	0.000001	1.90	0.6	66	0.3

Appendix B

Supplementary materials for: Seawater stable strontium isotope ratios during the Eocene-Oligocene Transition

B.1 Sample preparation and strontium isotope analyses

We selected sediment core samples spanning 32 to 36 Ma from Integrated Ocean Drilling Program Site U1333 and Ocean Drilling Program Site 1218 in the equatorial Pacific. Previous studies utilizing marine barite from Site 1218 (Griffith et al., 2010, 2011) and Site U1333 (Erhardt et al., 2013; Yao et al., 2021) have confirmed that marine barite is well preserved in these cores and reliably records seawater chemistry.

Barite was extracted from bulk sediments by sequential leaching and checked for purity by scanning electron microscopy before dissolution by chelation with Mitsubishi MCI® Gel-CK08P cation exchange resin (Eagle et al., 2003; Paytan et al., 1993). Bulk carbonate was leached from sediments using acetic acid following an ammonium acetate pre-leach after Bailey et al. (2000). Major cations (Ba, Sr, Ca) and trace elements were measured by ICP-OES and ICP-MS, respectively. Elemental ratios (e.g., Al/Ba, Ti/Ba, Mn/Ba) were used to further screen barite samples for contaminating phases.

For each sample, an ^{87}Sr/^{84}Sr-spiked aliquot and an unspiked aliquot of 1200 ng Sr were prepared for isotopic analysis by column chromatography with Bio-Rad AG®50W-X8 cation exchange resin (barite) or Eichrom's Sr-Spec resin (carbonate). Procedural blanks were less than 0.5 ng Sr. Strontium isotope ratios ($\delta^{88/86}$Sr and ^{87}Sr/^{86}Sr) were measured by double spike thermal ionization mass spectrometry on a Triton™ TIMS (ThermoFisher) at GEOMAR Helmholtz Center for Ocean Research Kiel (Germany) according to the method detailed by Krabbenhöft et al. (2009). In summary, approximately 600 ng Sr was loaded onto degassed rhenium filaments with a tantalum activator, dried, and heated briefly at ∼2 A before loading on the TIMS. For a single measurement, separate analyses of an ^{87}Sr/^{84}Sr-spiked sample and an unspiked sample were performed.

The ^{88}Sr/^{86}Sr ratios were calculated by the double spike correction algorithm and reported in delta notation as $\delta^{88/86}$Sr (‰) = (^{88}Sr/^{86}Sr$_{sample}$/ ^{88}Sr/^{86}Sr$_{SRM987}$ - 1) * 1000. We report the traditional radiogenic Sr isotope value ^{87}Sr/^{86}Sr normalized to a ^{88}Sr/^{86}Sr ratio of 8.375209. The typical internal precision for an individual measurement is <0.00001 for ^{87}Sr/^{86}Sr and <0.01 for ^{88}Sr/^{86}Sr. The external reproducibility was determined by repeated measurements of the JCp-1 coral standard ($\delta^{88/86}$Sr =0.19±0.02‰, ^{87}Sr/^{86}Sr,=0.70918±0.00002, n=9), the IAPSO seawater standard ($\delta^{88/86}$Sr =0.39±0.02‰, ^{87}Sr/^{86}Sr,=0.70917±0.00001, n=8), and NIST® SRM® 987 ($\delta^{88/86}$Sr =0.00±0.02‰, ^{87}Sr/^{86}Sr,=0.71024±0.00002, n=17) processed multiple times with both AG®50 and Sr-Spec chromatographic separations. Procedural blanks were less than 0.5 ng Sr.

The ^{87}Sr/^{86}Sr data set was used as an additional screening criteria, as barite and carbonate ^{87}Sr/^{86}Sr should reflect the contemporaneous seawater composition. We discarded three measurements based on ^{87}Sr/^{86}Sr values that fell outside of the reasonable range of Eocene-Oligocene seawater values (McArthur & Howarth, 2020).

B.2 Generalized additive model fit to the $\delta^{88/86}$Sr record

To formally test whether barite (and derived seawater) $\delta^{88/86}$Sr values changed with time, we fit a generalized additive model using the package `mgcv` in R (S. N. Wood,

2011) to the combined barite $\delta^{88/86}$Sr values from this study and Paytan et al. (2021). We estimated a smooth effect of time using 10 knots and a cubic spline basis function and used the gam.check function to confirm that this number of knots was sufficient. The spline term was associated with a p-value of 0.158, indicating no support for the alternative hypothesis of a nonzero trend in time.

B.3 Variability in barite $\delta^{88/86}$Sr between cores

Barite $\delta^{88/86}$Sr values from Site 1218 are consistently lower than those from Sites U1333 and 574 between 35 Ma and 33.7 Ma (though the error bars overlap). For the full dataset, a t-test comparison of pre-EOT (>33.7 Ma) and post-EOT (<33.7 Ma) $\delta^{88/86}$Sr shows no significant difference in the means (p-value = 0.28). Removing Site 1218 results in a statistically significant difference between the means (p-value = 0.02), because the lower $\delta^{88/86}$Sr values at Site 1218 lower the pre-EOT mean. However, we have no reason to exclude Site 1218. Even if we did so, the statistically significant difference in pre-EOT and post-EOT mean $\delta^{88/86}$Sr is small (0.017‰) and does not change our conclusions.

B.4 Strontium isotope mass balance

We used a simple ocean box model to calculate the effect of the shelf-basin fractionation mechanism on seawater Sr concentration ([Sr]) and $\delta^{88/86}$Sr assuming different shelf carbonate mineralogies. We tested the same shelf-basin fractionation forcing as Armstrong McKay et al. (2016): 1) an 80% reduction in shallow carbonate burial applied in two steps (33% in step one) and 2) a temporary 100% increase in carbonate weathering applied in two steps (33% in step one) (Supplementary Figure B.1). We assessed the changes in ocean [Sr] and $\delta^{88/86}$Sr over ~500 kyr, the approximate duration of the EOT.

The rate of change in the ocean Sr inventory (Sr_{sw}) is given by:

$$\frac{\Delta Sr_{sw}}{\Delta t} = F_{in} - F_{out} \tag{B.1}$$

where F_{in} is the total of all input fluxes of Sr to the ocean and F_{out} is the total output of Sr via carbonate burial.

The isotope mass balance for seawater $\delta^{88/86}$Sr (δ_{sw}) is:

$$\frac{\Delta(\delta_{sw} * Sr_{sw})}{\Delta t} = \delta_{in} * F_{in} - (\delta_{sw} + \Delta^{88/86}Sr_{sw-carb}) * F_{out} \tag{B.2}$$

where δ_{in} represents the $\delta^{88/86}$Sr value of the total input (F_{in}) flux and the isotopic composition of the carbonate sink (F_{out}) has an average isotopic offset ($\Delta^{88/86}Sr_{sw-carb}$) of -0.18‰ from seawater $\delta^{88/86}$Sr (Krabbenhöft et al., 2010).

The residence time (τ) of Sr in the ocean is given by:

$$\tau = Sr_{sw}/F_{out} \tag{B.3}$$

Model scenarios 1–4 assumed an initial steady state Eocene ocean with a Sr inventory equal to modern day ($Sr_{sw} = 120\text{x}10^6$ Gmol Sr) with an isotopic composition of 0.38‰. We used an initial global carbonate burial flux of 0.329 Gt C yr^{-1} with 45% buried in the shallow ocean (Armstrong McKay et al., 2016). The initial residence time (~3.8 Myr) is an important assumption in the model scenarios because the input flux is set based on the steady state output (F_{out}) and the seawater $\delta^{88/86}$Sr response to a perturbation depends on the standing stock of Sr in the ocean (Sr_{sw}). For the same perturbation, the $\delta^{88/86}$Sr response will be greater for a smaller ocean Sr inventory (shorter residence time). In model scenarios 5 and 6, we used shorter and longer residence times, respectively, to test the sensitivity of our results to this assumption.

The proportion of aragonite (8000 ppm Sr) to calcite (1000 ppm Sr) in the shallow carbonate burial flux was varied between different experiments and was maintained for the duration of each experiment since any global change in dominant polymorph would occur over longer timescales (Stanley & Hardie, 1998).

Scenario 1: Aragonite-calcite shelf-basin fractionation

We determined the effect of an 80% reduction in shallow carbonate burial as proposed by Armstrong McKay et al. (2016), assuming that shallow carbonates are 2/3 aragonite and 1/3 calcite (Krabbenhöft et al., 2010). The 80% reduction in neritic carbonate burial was applied in two steps following Armstrong McKay et al. (2016) with 33% of the reduction occurring at 34 Ma and the remainder at 33.7 Ma. The CCD deepening was approximated as a linear 100% increase in the pelagic carbonate flux over 500 kyr

(34 to 33.5 Ma), assuming that the change in the pelagic carbonate flux is proportional to the doubling of the seafloor area above the CCD (Rea & Lyle, 2005). The input flux of Sr (including weathering) was held constant at the initial steady state value.

This scenario results in a 13% increase in seawater [Sr] and a 0.02‰ decrease in $\delta^{88/86}$Sr over 500 kyr. Because the increase in pelagic carbonate (1000 ppm Sr) does not fully offset the reduced sink of Sr in shallow carbonate (8000 ppm Sr), the Sr mass imbalance is sustained and [Sr] and $\delta^{88/86}$Sr continue to increase and decrease, respectively, for longer than 500 kyr. After 750 kyr, $\delta^{88/86}$Sr decreased by 0.03‰. The actual magnitude of the $\delta^{88/86}$Sr response would depend on how long the Sr budget remained out of equilibrium before the input and output fluxes were eventually re-balanced.

Scenario 2: Aragonite-calcite shelf-basin fractionation + carbonate weathering pulse

We added a pulsed 100% increase in carbonate weathering with a $\delta^{88/86}$Sr value of 0.19‰ to the model configuration used in Scenario 1 after Armstrong McKay et al. (2016). The weathering pulse was applied in two steps with a 33% increase at 34 Ma and the remainder at 33.7 Ma.

This model scenario resulted in a 22% increase in ocean [Sr] and a 0.03‰ decrease in $\delta^{88/86}$Sr over 500 kyr.

Scenario 3: Calcite-calcite shelf-basin fractionation

We applied the 80% reduction in neritic carbonate burial as in Scenario 1 but assumed that the shallow carbonates were entirely calcite (no aragonite). The pelagic carbonate flux was linearly increased over 500 kyr until the 80% loss of the shallow carbonate was fully compensated ($F_{in} = F_{out}$).

The ocean Sr budget was only transiently perturbed by the transfer of carbonate burial from the shelf to basin and attained a new steady state once the input and output fluxes equalized. Changes in [Sr] and $\delta^{88/86}$Sr were negligible.

Scenario 4: Calcite-calcite shelf-basin fractionation + carbonate weathering pulse

The pulsed 100% increase in carbonate weathering with a $\delta^{88/86}$Sr value of 0.19‰ was included in the same model configuration as Scenario 3.

In this model scenario, [Sr] and $\delta^{88/86}$Sr increased by 4% and decreased by <0.01‰ over 500 kyr, respectively. We note that this scenario does not account for the initial overdeepening of the CCD, which probably rapidly compensated the carbonate weathering pulse so that the [Sr] inventory increased only transiently (i.e., returned to pre-perturbation steady state). Even without this extra compensation, the calculated $\delta^{88/86}$Sr change is too small to be measured given the analytical uncertainty.

Scenario 5: Calcite-calcite shelf-basin fractionation + carbonate weathering pulse + shorter residence time

We repeated Scenario 4 while reducing the initial ocean Sr inventory so that the residence time was 2 Myr (similar to modern). The shorter residence time resulted in a [Sr] increase of 7% and $\delta^{88/86}$Sr decrease of 0.01‰ over 500 kyr, approximately 50% greater change than calculated in Scenario 4 with a residence time of 3.8 Myr.

Scenario 6: Calcite-calcite shelf-basin fractionation + carbonate weathering pulse + longer residence time

We increased the initial ocean Sr inventory so that the residence time was 5.4 Myr ([Sr] = 120 umol/kg). A higher ocean [Sr] during the Eocene is suggested by Sr/Ca reconstructions, though the uncertainty and disagreement between benthic foraminifera, fossil fish teeth, calcite veins, and gastropods is substantial (Sosdian et al., 2012). The longer residence time resulted in negligible [Sr] increase (2%) and $\delta^{88/86}$Sr decrease (<0.01‰) over 500 kyr.

B.5 Supplemental tables and figures

Table B.1: Stable ($\delta^{88/86}$Sr) and radiogenic (^{87}Sr/^{86}Sr) strontium isotope ratios in marine barite samples. Replicate analyses are indicated by an asterisk. The standard error of the mean ($2\sigma_{mean}$) gives the internal error for each individual measurement. Age models from Westerhold et al. (2014).

	Age (Ma)	Sample	$\delta^{88/86}$Sr	$2\sigma_{mean}$	n	^{87}Sr/^{86}Sr	$2\sigma_{mean}$
U1333C	31.96	12-3, 100-102	-0.15	0.006	4	0.707948	0.000002
	32.03	12-4, 50-52	-0.17	0.007	4	0.707921	0.000007
	32.40	13-3, 148-150	-0.23[a]	0.007	4	0.707913	0.000007
	32.87	13-7, 50-52	-0.18	0.004	4	0.707893	0.000001
	33.62	14-3, 117-119	-0.12	0.001	4	0.707848	0.000002
	33.80	14-4, 137-139	-0.12	0.006	4	0.707837	0.000008
	34.35	14-5, 125-127	-0.10	0.007	4	0.707841	0.000003
	34.35	14-5, 125-127*	-0.13	0.007	4	0.707843	0.000006
	35.29	14-7, 45-47	-0.15	0.001	4	0.707819	0.000002
	35.29	14-7, 45-47*	-0.14	0.002	4	0.707823	0.000005
	35.52	15-1, 55-57	-0.18	0.003	4	0.707795	0.000007
	35.75	15-1, 145-147	-0.14	0.005	4	0.707806	0.000005
1218A	32.29	22-3, 145-150	-0.16	0.004	4	0.707922	0.000000
	33.74	24-1, 3-8	-0.17	0.004	4	0.707873	0.000003
	33.83	24-1, 90-93	-0.17	0.014	4	0.707843	0.000007
	34.29	24-3, 47-50	-0.17	0.002	2	0.707836	0.000002
	34.92	24-5, 42-45	-0.17	0.006	4	0.707835	0.000005
	35.41	24-6, 102-104	-0.15	0.002	4	0.707849	0.000000
	35.52	24-7, 8-11	-0.16	0.006	4	0.707844	0.000010
574C	32.56	31-2, 26-30	-0.15	0.008	4	0.707926	0.000000

[a] outlier excluded from Figure 2 in main text

Table B.2: Stable ($\delta^{88/86}$Sr) and radiogenic (^{87}Sr/^{86}Sr) strontium isotope ratios in bulk carbonate samples. Replicate analyses are indicated by an asterisk. The standard error of the mean ($2\sigma_{mean}$) gives the internal error for each individual measurement.

	Age (Ma)	Sample	$\delta^{88/86}$Sr	$2\sigma_{mean}$	n	^{87}Sr/^{86}Sr	$2\sigma_{mean}$
U1333C	31.96	12-3, 99-101	0.20	0.010	2	0.707901	0.000008
	32.03	12-4, 48-50	0.27	0.004	4	0.707874	0.000010
	32.40	13-3, 147-148	0.20	0.003	2	0.707880	0.000010
	32.87	13-7, 50-52	0.18	0.005	4	0.707847	0.000010
	32.87	13-7, 50-52*	0.20	0.003	2	0.707903	0.000016
	33.62	14-3, 117-119	0.22	0.007	2	0.707817	0.000006
	33.80	14-4, 137-139	0.25	0.008	4	0.707799	0.000006
	34.35	14-5, 125-127	0.23	0.000	4	0.707832	0.000001
	35.29	14-7, 45-47	0.24	0.006	4	0.707783	0.000016
	35.52	15-1, 55-57	0.18	0.009	4	0.707769	0.000003

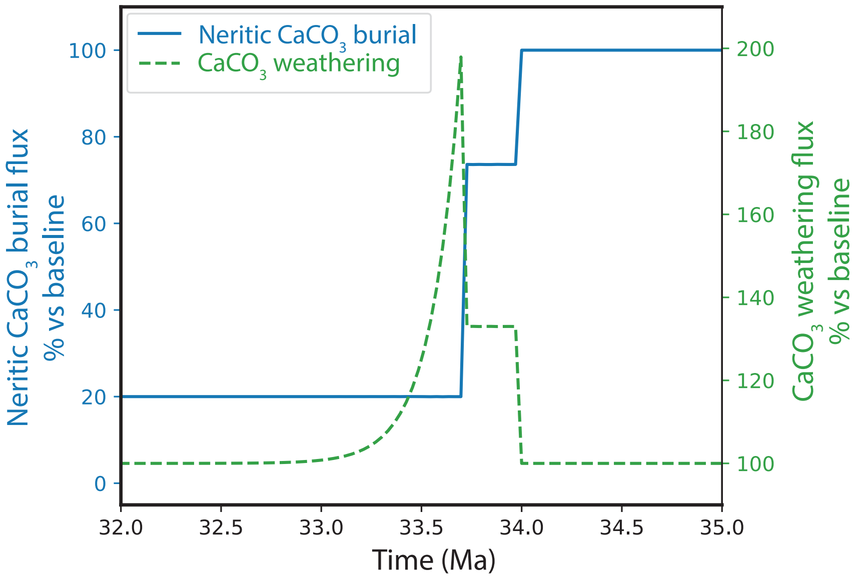

Figure B.1: Box model scenarios of the shelf-basin fractionation mechanism after Armstrong McKay et al. (2016). A two-step 80% reduction in neritic carbonate burial was applied in all scenarios (blue solid curve). For scenarios that also included a pulse of carbonate weathering, a two-step temporary 100% increase in carbonate weathering was added (green dashed curve).

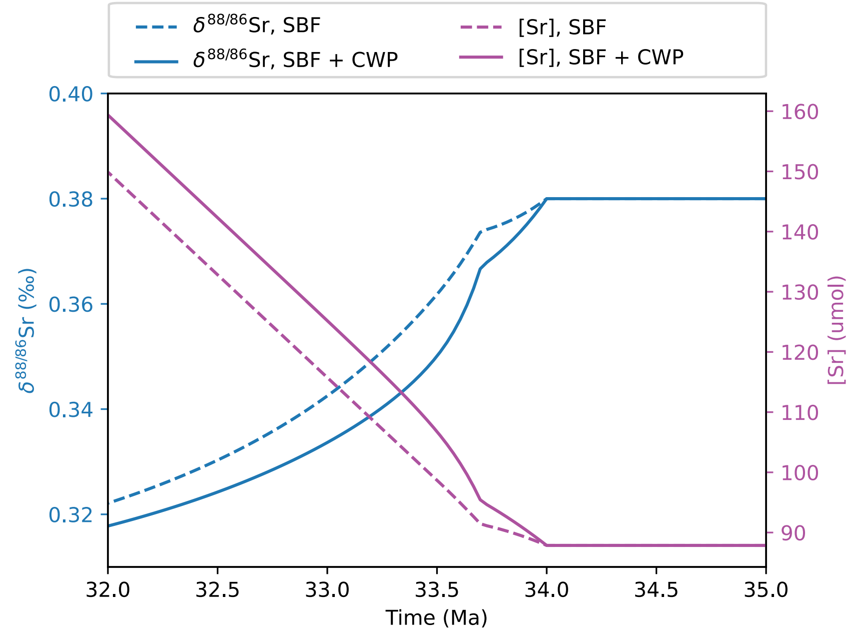

Figure B.2: Results of model scenarios 1 and 2 assuming 2/3 aragonite, 1/3 calcite shelf carbonate mineralogy. Abbreviations: SBF = shelf-basin fractionation, CWP = carbonate weathering pulse.

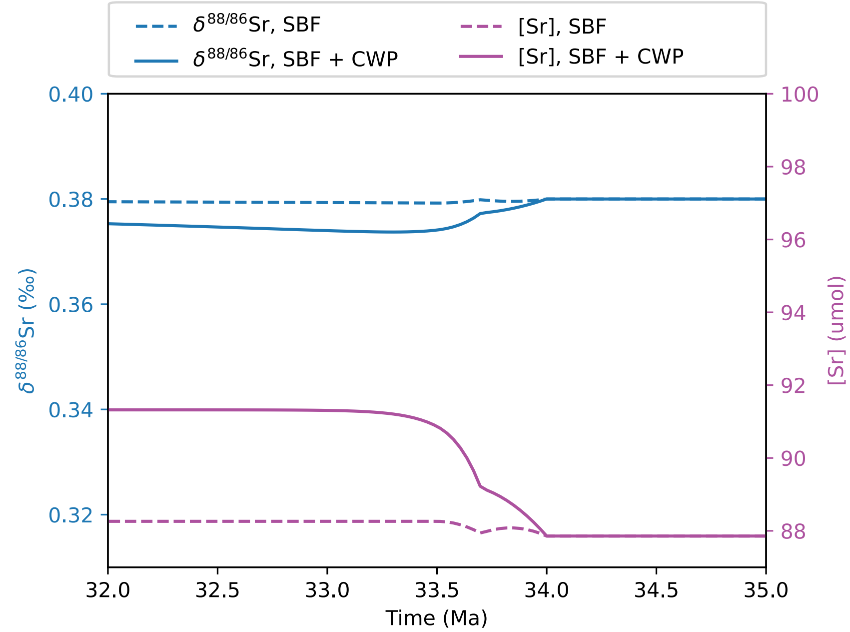

Figure B.3: Results of model scenarios 3, 4, and 5 assuming calcite-only shelf mineralogy. Abbreviations: SBF = shelf-basin fractionation, CWP = carbonate weathering pulse.

Bibliography

Anderson, R., Fleisher, M., Lao, Y., & Winckler, G. (2008). Modern CaCO3 preservation in equatorial Pacific sediments in the context of late-Pleistocene glacial cycles. *Marine Chemistry*, *111*(1-2), 30–46.

Andersson, A. J. (2014, January). 8.19 - The Oceanic CaCO3 Cycle. In H. D. Holland & K. K. Turekian (Eds.), *Treatise on Geochemistry (Second Edition)* (pp. 519–542). Elsevier.

Ando, A., Nakano, T., Kawahata, H., Yokoyama, Y., & Khim, B. (2010). Testing seawater Sr isotopic variability on a glacial-interglacial timescale: An application of latest high-precision thermal ionization mass spectrometry. *Geochemical Journal*, *44*, 347–357.

Archer, D. E. (1991). Equatorial Pacific Calcite Preservation Cycles: Production or Dissolution? *Paleoceanography*, *6*(5), 561–571.

Archer, D. E., & Maier-Reimer, E. (1994). Effect of deep-sea sedimentary calcite preservation on atmospheric CO2 concentration. *Nature*, *367*, 260–263.

Archer, D. E. (2010, November). *The Global Carbon Cycle*. Princeton University Press.

Armstrong McKay, D. I. (2015). *Investigating the drivers of perturbations to the Cenozoic carbon-climate system* [PhD Thesis]. University of Southampton, Faculty of Natural & Environmental Sciences.

Armstrong McKay, D. I., Tyrrell, T., & Wilson, P. A. (2016). Global carbon cycle perturbation across the Eocene-Oligocene climate transition. *Paleoceanography*, *31*(2), 311–329.

Arrhenius, G. (1952). Sediment cores from the East Pacific. *Reports of the Swedish deep-sea expedition, 1947-1948*, *5*(1), 201.

Averyt, K. B., & Paytan, A. (2003). Empirical partition coefficients for Sr and Ca in marine barite: Implications for reconstructing seawater Sr and Ca concentrations. *Geochemistry, Geophysics, Geosystems*, *4*(5).

Averyt, K. B. (2004). *Strontium and calcium in marine barite* [Doctoral dissertation, Stanford University].

Bailey, T. R., McArthur, J. M., Prince, H., & Thirlwall, M. F. (2000). Dissolution methods for strontium isotope stratigraphy: Whole rock analysis. *Chemical Geology*, *167*(3), 313–319.

Balsam, W. L. (1983). Carbonate dissolution on the Muir Seamount (western North Atlantic); interglacial/glacial changes. *Journal of Sedimentary Research*, *53*(3), 719–731.

Balsam, W. L., & McCoy, F. W. (1987). Atlantic sediments: Glacial/interglacial comparisons. *Paleoceanography*, *2*(5), 531–542.

Balter, V., Lécuyer, C., & Barrat, J.-A. (2011). Reconstructing seawater Sr/Ca during the last 70My using fossil fish tooth enamel. *Palaeogeography, Palaeoclimatology, Palaeoecology*, *310*(1-2), 133–138.

Bassinot, F. C., Beaufort, L., Vincent, E., Labeyrie, L. D., Rostek, F., Müller, P. J., Quidelleur, X., & Lancelot, Y. (1994). Coarse fraction fluctuations in pelagic carbonate sediments from the tropical Indian Ocean: A 1500-kyr record of carbonate dissolution. *Paleoceanography*, *9*(4), 579–600.

Battaglia, G., Steinacher, M., & Joos, F. (2016). A probabilistic assessment of calcium carbonate export and dissolution in the modern ocean. *Biogeosciences*, *13*(9), 2823–2848.

Berger, W. H. (1982). Increase of carbon dioxide in the atmosphere during deglaciation: The coral reef hypothesis. *Naturwissenschaften*, *69*(2), 87–88.

Berner, R. A. (2003). The long-term carbon cycle, fossil fuels and atmospheric composition. *Nature*, *426*(6964), 323–326.

Berner, R. A. (2004). *The Phanerozoic Carbon Cycle: CO2 and O2*. Oxford University Press, Incorporated.

Betzler, C., Eberli, G. P., Lüdmann, T., Reolid, J., Kroon, D., Reijmer, J. J. G., Swart, P. K., Wright, J., Young, J. R., Alvarez-Zarikian, C., Alonso-García, M., Bialik, O. M., Blättler, C. L., Guo, J. A., Haffen, S., Horozal, S., Inoue, M., Jovane, L., Lanci, L., … Yao, Z. (2018). Refinement of Miocene sea level and monsoon events from the sedimentary archive of the Maldives (Indian Ocean). *Progress in Earth and Planetary Science*, *5*(1), 5.

Betzler, C., Eberli, G., Alvarez Zarikian, C., & Expedition 359 Scientists. (2017). Expedition 359 summary. *Proceedings of the International Ocean Discovery Program*, *359*.

Biscaye, P. E., Kolla, V., & Turekian, K. K. (1976). Distribution of calcium carbonate in surface sediments of the Atlantic Ocean. *Journal of Geophysical Research (1896-1977)*, *81*(15), 2595–2603.

Blättler, C. L., Higgins, J. A., & Swart, P. K. (2019). Advected glacial seawater preserved in the subsurface of the Maldives carbonate edifice. *Geochimica et Cosmochimica Acta*, *257*, 80–95.

Böhm, F., Eisenhauer, A., Tang, J., Dietzel, M., Krabbenhöft, A., Kisakürek, B., & Horn, C. (2012). Strontium isotope fractionation of planktic foraminifera and inorganic calcite. *Geochimica et Cosmochimica Acta*, *93*, 300–314.

Boudreau, B. P., & Luo, Y. (2017). Retrodiction of secular variations in deep-sea CaCO3 burial during the Cenozoic. *Earth and Planetary Science Letters*, *474*, 1–12.

Broecker, W. S. (2003, January). 6.19 - The Oceanic CaCO3 Cycle. In H. D. Holland & K. K. Turekian (Eds.), *Treatise on Geochemistry* (pp. 529–549). Pergamon.

Broecker, W. S. (2009). Wally's Quest to Understand the Ocean's CaCO3 Cycle. *Annual Review of Marine Science*, *1*(1), 1–18.

Broecker, W. S., & Peng, T.-H. (1982). *Tracers in the Sea*. Eldigio Press.

Broecker, W. S., & Peng, T.-H. (1987). The role of CaCO3 compensation in the glacial to interglacial atmospheric CO2 change. *Global Biogeochemical Cycles*, *1*(1), 15–29.

Brovkin, V., Ganopolski, A., Archer, D., & Rahmstorf, S. (2007). Lowering of glacial atmospheric CO2 in response to changes in oceanic circulation and marine biogeochemistry. *Paleoceanography*, *22*, PA4202.

Cabioch, G., Montaggioni, L., Thouveny, N., Frank, N., Sato, T., Chazottes, V., Dalamasso, H., Payri, C., Pichon, M., & Sémah, A.-M. (2008). The chronology and structure of the western New Caledonian barrier reef tracts. *Palaeogeography, Palaeoclimatology, Palaeoecology*, *268*(1), 91–105.

Camoin, G. F., Ebren, P., Eisenhauer, A., Bard, E., & Faure, G. (2001). A 300000-yr coral reef record of sea level changes, Mururoa atoll (Tuamotu archipelago, French Polynesia). *Palaeogeography, Palaeoclimatology, Palaeoecology*, *175*(1), 325–341.

Camoin, G. F., Seard, C., Deschamps, P., Webster, J. M., Abbey, E., Braga, J. C., Iryu, Y., Durand, N., Bard, E., Hamelin, B., Yokoyama, Y., Thomas, A. L., Henderson, G. M., & Dussouillez, P. (2012). Reef response to sea-level and environmental changes during the last deglaciation: Integrated Ocean Drilling Program Expedition 310, Tahiti Sea Level. *Geology*, *40*(7), 643–646.

Camoin, G. F., & Webster, J. M. (2015). Coral reef response to Quaternary sea-level and environmental changes: State of the science. *Sedimentology*, *62*(2), 401–428.

Campbell, S. M., Moucha, R., Derry, L. A., & Raymo, M. E. (2018). Effects of dynamic topography on the cenozoic carbonate compensation depth. *Geochemistry, Geophysics, Geosystems*, *19*(4), 1025–1034.

Cartapanis, O., Galbraith, E. D., Bianchi, D., & Jaccard, S. L. (2018). Carbon burial in deep-sea sediment and implications for oceanic inventories of carbon and alkalinity over the last glacial cycle. *Climate of the Past*, *14*(11), 1819–1850.

Castro-Sanguino, C., Bozec, Y.-M., & Mumby, P. J. (2020). Dynamics of carbonate sediment production by Halimeda: Implications for reef carbonate budgets. *Marine Ecology Progress Series*, *639*, 91–106.

Catubig, N. R., Archer, D. E., Francois, R., deMenocal, P., Howard, W., & Yu, E.-F. (1998). Global deep-sea burial rate of calcium carbonate during the Last Glacial Maximum. *Paleoceanography*, *13*(3), 298–310.

Choudhury, D., Timmermann, A., Schloesser, F., Heinemann, M., & Pollard, D. (2020). Simulating Marine Isotope Stage 7 with a coupled climate–ice sheet model. *Climate of the Past*, *16*(6), 2183–2201.

Clark, P. U., Archer, D., Pollard, D., Blum, J. D., Rial, J. A., Brovkin, V., Mix, A. C., Pisias, N. G., & Roy, M. (2006). The middle Pleistocene transition: Characteristics, mechanisms, and implications for long-term changes in atmospheric pCO2. *Quaternary Science Reviews*, *25*(23-24), 3150–3184.

Clark, P. U., McCabe, A. M., Mix, A. C., & Weaver, A. J. (2004). Rapid Rise of Sea Level 19,000 Years Ago and Its Global Implications. *Science*, *304*(5674), 1141–1144.

Coggon, R. M., Teagle, D. A. H., Smith-Duque, C. E., Alt, J. C., & Cooper, M. J. (2010). Reconstructing Past Seawater Mg/Ca and Sr/Ca from Mid-Ocean Ridge Flank Calcium Carbonate Veins. *Science*, *327*(5969), 1114–1117.

Coletti, G., Commissario, L., Mariani, L., Bosio, G., Desbiolles, F., Soldi, M., & Bialik, O. M. (2022). Palaeocene to Miocene southern Tethyan carbonate factories: A meta-analysis of the successions of South-western and Western Central Asia. *The Depositional Record*, *8*(3), 1031–1054.

Costa, K. M., Hayes, C. T., Anderson, R. F., Pavia, F. J., Bausch, A., Deng, F., Dutay, J.-C., Geibert, W., Heinze, C., Henderson, G., Hillaire-Marcel, C., Hoffmann, S., Jaccard, S. L., Jacobel, A. W., Kienast, S. S., Kipp, L., Lerner, P., Lippold, J., Lund, D., … Zhou, Y. (2020). 230Th Normalization: New Insights on an Essential Tool for Quantifying Sedimentary Fluxes in the Modern and Quaternary Ocean. *Paleoceanography and Paleoclimatology*, *35*(2), e2019PA003820.

Coxall, H. K., & Wilson, P. A. (2011). Early Oligocene glaciation and productivity in the eastern equatorial Pacific: Insights into global carbon cycling. *Paleoceanography*, *26*(2), PA2221.

Coxall, H. K., Wilson, P. A., Palike, H., Lear, C. H., & Backman, J. (2005). Rapid stepwise onset of Antarctic glaciation and deeper calcite compensation in the Pacific Ocean. *Nature*, *433*, 53–57.

Crowley, T. J. (1985). Late Quaternary Carbonate Changes in the North Atlantic and Atlantic/Pacific Comparisons. In W. S. Broecker & E. T. Sundquist (Eds.), *The Carbon Cycle and Atmospheric CO2: Natural Variations Archean to Present* (pp. 271–284). American Geophysical Union (AGU).

Davies, P. J. (2011). Halimeda Bioherms. In D. Hopley (Ed.), *Encyclopedia of Modern Coral Reefs: Structure, Form and Process* (pp. 535–549). Springer Netherlands.

Davis, A. C., Bickle, M. J., & Teagle, D. a. H. (2003). Imbalance in the oceanic strontium budget. *Earth and Planetary Science Letters*, *211*(1-2), 173–187.

De La Rocha, C. L., & DePaolo, D. J. (2000). Isotopic Evidence for Variations in the Marine Calcium Cycle Over the Cenozoic. *Science*, *289*(5482), 1176–1178.

de Gelder, G., Husson, L., Pastier, A.-M., Fernández-Blanco, D., Pico, T., Chauveau, D., Authemayou, C., & Pedoja, K. (2022). High interstadial sea levels over the past 420ka from the Huon Peninsula, Papua New Guinea. *Communications Earth & Environment*, *3*(1), 1–12.

de Gelder, G., Jara-Muñoz, J., Melnick, D., Fernández-Blanco, D., Rouby, H., Pedoja, K., Husson, L., Armijo, R., & Lacassin, R. (2020). How do sea-level curves influence modeled marine terrace sequences? *Quaternary Science Reviews*, *229*, 106132.

de Macêdo Carneiro, P. B., & de Morais, J. O. (2016). Carbonate sediment production in the equatorial continental shelf of South America: Quantifying Halimeda incrassata (Chlorophyta) contributions. *Journal of South American Earth Sciences*, *72*, 1–6.

de Macêdo Carneiro, P. B., Pereira, J. U., & Matthews-Cascon, H. (2018). Standing stock variations, growth and CaCO3 production by the calcareous green alga Halimeda opuntia. *Marine Biological Association of the United Kingdom. Journal of the Marine Biological Association of the United Kingdom*, *98*(2), 401–409.

deMenocal, P., Archer, D., & Leth, P. (1997). Pleistocene variations in deep Atlantic circulation and calcite burial between 1.2 and 0.6 Ma: A combined data-model approach. *Proc. ODP, Sci. Results*, *154*, 285–298.

Drew, E. A. (1983). Halimeda biomass, growth rates and sediment generation on reefs in the central great barrier reef province. *Coral Reefs*, *2*(2), 101–110.

Dullo, W.-C. (2005). Coral growth and reef growth: A brief review. *Facies*, *51*(1), 33–48.

Dunne, J. P., Hales, B., & Toggweiler, J. R. (2012). Global calcite cycling constrained by sediment preservation controls. *Global Biogeochemical Cycles*, *26*, GB3023.

Dutton, A., & Lambeck, K. (2012). Ice Volume and Sea Level During the Last Interglacial. *Science*, *337*(6091), 216–219.

Eagle, M., Paytan, A., Arrigo, K. R., van Dijken, G., & Murray, R. W. (2003). A comparison between excess barium and barite as indicators of carbon export. *Paleoceanography*, *18*(1), 1021.

Elderfield, H., Cooper, M., & Ganssen, G. (2000). Sr/Ca in multiple species of planktonic foraminifera: Implications for reconstructions of seawater Sr/Ca. *Geochemistry, Geophysics, Geosystems*, *1*(1017).

Erhardt, A. M., Pälike, H., & Paytan, A. (2013). High-resolution record of export production in the eastern equatorial Pacific across the Eocene-Oligocene transition and relationships to global climatic records. *Paleoceanography*, *28*(1), 130–142.

ETOPO 2022 15 Arc-Second Global Relief Model. (2022).

Fairbanks, R. G. (1989). A 17,000-year glacio-eustatic sea level record: Influence of glacial melting rates on the Younger Dryas event and deep-ocean circulation. *Nature*, *342*, 637–642.

Fantle, M. S. (2010). Evaluating the Ca isotope proxy. *American Journal of Science*, *310*(3), 194–230.

Fantle, M. S., Maher, K. M., & DePaolo, D. J. (2010). Isotopic approaches for quantifying the rates of marine burial diagenesis. *Reviews of Geophysics*, *48*(3).

Fantle, M. S., & DePaolo, D. J. (2006). Sr isotopes and pore fluid chemistry in carbonate sediment of the Ontong Java Plateau: Calcite recrystallization rates and evidence for a rapid rise in seawater Mg over the last 10 million years. *Geochimica et Cosmochimica Acta*, *70*(15), 3883–3904.

Fantle, M. S., & DePaolo, D. J. (2007). Ca isotopes in carbonate sediment and pore fluid from ODP Site 807A: The Ca2+(aq)–calcite equilibrium fractionation factor and calcite recrystallization rates in Pleistocene sediments. *Geochimica et Cosmochimica Acta*, *71*(10), 2524–2546.

Fantle, M. S., & Higgins, J. A. (2014). The effects of diagenesis and dolomitization on Ca and Mg isotopes in marine platform carbonates: Implications for the geochemical cycles of Ca and Mg. *Geochimica et Cosmochimica Acta*, *142*, 458–481.

Fantle, M. S., & Tipper, E. T. (2014). Calcium isotopes in the global biogeochemical Ca cycle: Implications for development of a Ca isotope proxy. *Earth-Science Reviews*, *129*, 148–177.

Farrell, J. W., & Prell, W. L. (1989). Climatic change and CaCO3 preservation: An 800,000 year bathymetric Reconstruction from the central equatorial Pacific Ocean. *Paleoceanography*, *4*(4), 447–466.

Fietzke, J., & Eisenhauer, A. (2006). Determination of temperature-dependent stable strontium isotope (88Sr/86Sr) fractionation via bracketing standard MC-ICP-MS. *Geochemistry, Geophysics, Geosystems*, *7*(8).

Francois, R., Frank, M., Rutgers van der Loeff, M. M., & Bacon, M. P. (2004). 230Th normalization: An essential tool for interpreting sedimentary fluxes during the late Quaternary. *Paleoceanography*, *19*, PA1018.

Frank, T. D., James, N. P., Bone, Y., Malcolm, I., & Bobak, L. E. (2014). Late Quaternary carbonate deposition at the bottom of the world. *Sedimentary Geology*, *305*, 1–16.

Fu, H., Jian, X., Zhang, W., & Shang, F. (2020). A comparative study of methods for determining carbonate content in marine and terrestrial sediments. *Marine and Petroleum Geology*, *116*, 104337.

Geske, A., Lokier, S., Dietzel, M., Richter, D., Buhl, D., & Immenhauser, A. (2015). Magnesium isotope composition of sabkha porewater and related (Sub-)Recent stoichiometric dolomites, Abu Dhabi (UAE). *Chemical Geology*, *393-394*, 112–124.

Gothmann, A. M., Stolarski, J., Adkins, J. F., & Higgins, J. A. (2017). A Cenozoic record of seawater Mg isotopes in well-preserved fossil corals. *Geology*, *45*(11), 1039–1042.

Graham, D., Bender, M., Williams, D. F., & Keigwin, L. (1982). Strontium-calcium ratios in Cenozoic planktonic foraminifera. *Geochimica Et Cosmochimica Acta*, *46*, 1281–1292.

Greene, S. E., Ridgwell, A., Kirtland Turner, S., Schmidt, D. N., Pälike, H., Thomas, E., Greene, L. K., & Hoogakker, B. A. A. (2019). Early Cenozoic Decoupling of Climate and Carbonate Compensation Depth Trends. *Paleoceanography and Paleoclimatology*, *34*(6), 930–945.

Griffith, E. M., & Paytan, A. (2012). Barite in the ocean - occurrence, geochemistry and palaeoceanographic applications: Barite in the ocean. *Sedimentology*, *59*(6), 1817–1835.

Griffith, E. M., Calhoun, M., Thomas, E., Averyt, K., Erhardt, A., Bralower, T., Lyle, M., Olivarez-Lyle, A., & Paytan, A. (2010). Export productivity and carbonate accumulation in the Pacific Basin at the transition from a greenhouse to icehouse climate (late Eocene to early Oligocene). *Paleoceanography*, *25*(3), PA3212.

Griffith, E. M., & Fantle, M. S. (2020, December). *Calcium Isotopes* (1st ed.). Cambridge University Press.

Griffith, E. M., Paytan, A., Caldeira, K., Bullen, T. D., & Thomas, E. (2008). A Dynamic Marine Calcium Cycle During the Past 28 Million Years. *Science*, *322*(5908), 1671–1674.

Griffith, E. M., Paytan, A., Eisenhauer, A., Bullen, T. D., & Thomas, E. (2011). Seawater calcium isotope ratios across the Eocene-Oligocene transition. *Geology*, *39*(7), 683–686.

Hain, M., Allen, K. A., & Kirtland Turner, S. (2024). Earth system carbon cycle dynamics through time. In *Reference Module in Earth Systems and Environmental Sciences*. Elsevier.

Hain, M., Sigman, D., & Haug, G. (2014, December). The Biological Pump in the Past. In *Treatise on Geochemistry: Second Edition* (pp. 485–517, Vol. 8).

Hain, M., & Sigman, D. M. (2024). CO2 in Earth's ice age cycles. *Oxford Research Encyclopedia of Climate Science*.

Hayes, C. T., Costa, K. M., Anderson, R. F., Calvo, E., Chase, Z., Demina, L. L., Dutay, J.-C., German, C. R., Heimbürger-Boavida, L.-E., Jaccard, S. L., Jacobel, A., Kohfeld, K. E., Kravchishina, M. D., Lippold, J., Mekik, F., Missiaen, L., Pavia, F. J., Paytan, A., Pedrosa-Pamies, R., . . . Zhang, J. (2021). Global Ocean Sediment Composition and Burial Flux in the Deep Sea. *Global Biogeochemical Cycles*, *35*(4), e2020GB006769.

Hebbeln, D., Bender, M., Gaide, S., Titschack, J., Vandorpe, T., Van Rooij, D., Wintersteller, P., & Wienberg, C. (2019). Thousands of cold-water coral mounds along the Moroccan Atlantic continental margin: Distribution and morphometry. *Marine Geology*, *411*, 51–61.

Henderson, G. M., Martel, D. J., O'Nions, R. K., & Shackleton, N. J. (1994). Evolution of seawater 87Sr/86Sr over the last 400 ka: The absence of glacial/interglacial cycles. *Earth and Planetary Science Letters*, *128*, 643–651.

Higgins, J. A., Blättler, C., Lundstrom, E., Santiago-Ramos, D., Akhtar, A., Crüger Ahm, A.-S., Bialik, O., Holmden, C., Bradbury, H., Murray, S., & Swart, P. (2018). Mineralogy, early marine diagenesis, and the chemistry of shallow-water carbonate sediments. *Geochimica et Cosmochimica Acta*, *220*, 512–534.

Higgins, J. A., & Schrag, D. (2012). Records of Neogene seawater chemistry and diagenesis in deep-sea carbonate sediments and pore fluids. *Earth and Planetary Science Letters*, *357-358*, 386–396.

Higgins, J. A., & Schrag, D. P. (2015). The Mg isotopic composition of Cenozoic seawater - evidence for a link between Mg-clays, seawater Mg/Ca, and climate. *Earth and Planetary Science Letters*, *416*, 73–81.

Hinestrosa, G., Webster, J. M., & Beaman, R. J. (2019). Spatio-temporal patterns in the postglacial flooding of the Great Barrier Reef shelf, Australia. *Continental Shelf Research*, *173*, 13–26.

Hinestrosa, G., Webster, J. M., & Beaman, R. J. (2022). New constraints on the postglacial shallow-water carbonate accumulation in the Great Barrier Reef. *Scientific Reports*, *12*(1), 924.

Hinestrosa, G., Webster, J. M., Beaman, R. J., & Anderson, L. M. (2014). Seismic stratigraphy and development of the shelf-edge reefs of the Great Barrier Reef, Australia. *Marine Geology*, *353*, 1–20.

Hoareau, G., Monnin, C., & Odonne, F. (2010). A study of celestine equilibrium in marine sediments using the entire ODP/IODP porewater data base. *Geochimica et Cosmochimica Acta*, *74*(14), 3925–3937.

Husson, L., Pastier, A.-M., Pedoja, K., Elliot, M., Paillard, D., Authemayou, C., Sarr, A.-C., Schmitt, A., & Cahyarini, S. Y. (2018). Reef Carbonate Productivity During Quaternary Sea Level Oscillations. *Geochemistry Geophysics Geosystems*, *19*(4), 1148–1164.

Hutchinson, D. K., Coxall, H. K., Lunt, D. J., Steinthorsdottir, M., de Boer, A. M., Baatsen, M., von der Heydt, A., Huber, M., Kennedy-Asser, A. T., Kunzmann, L., Ladant, J.-B., Lear, C. H., Moraweck, K., Pearson, P. N., Piga, E., Pound, M. J., Salzmann, U., Scher, H. D., Sijp, W. P., … Zhang, Z. (2021). The Eocene–Oligocene transition: A review of marine and terrestrial proxy data, models and model–data comparisons. *Climate of the Past*, *17*(1), 269–315.

Iglesias-Rodriguez, M. D., Armstrong, R., Feely, R., Hood, R., Kleypas, J., Milliman, J. D., Sabine, C., & Sarmiento, J. (2002). Progress made in study of ocean's calcium carbonate budget. *Eos, Transactions American Geophysical Union*, *83*(34), 365–375.

Isson, T. T., Planavsky, N. J., Coogan, L. A., Stewart, E. M., Ague, J. J., Bolton, E. W., Zhang, S., McKenzie, N. R., & Kump, L. R. (2020). Evolution of the Global Carbon Cycle and Climate Regulation on Earth. *Global Biogeochemical Cycles*, *34*(2), e2018GB006061.

Ivany, L. C., Peters, S. C., Wilkinson, B. H., Lohmann, K. C., & Reimer, B. A. (2004). Composition of the early Oligocene ocean from coral stable isotope and elemental chemistry. *Geobiology*, *2*(2), 97–106.

Jaccard, S., Galbraith, E., Sigman, D., Haug, G., Francois, R., Pedersen, T., Dulski, P., & Thierstein, H. (2009). Subarctic Pacific evidence for a glacial deepening of the oceanic respired carbon pool. *Earth and Planetary Science Letters*, *277*(1-2), 156–165.

Jacobson, A. D., & Holmden, C. (2008). 44Ca evolution in a carbonate aquifer and its bearing on the equilibrium isotope fractionation factor for calcite. *Earth and Planetary Science Letters*, *270*(3-4), 349–353.

Jones, N. S., Ridgwell, A., & Hendy, E. J. (2015). Evaluation of coral reef carbonate production models at a global scale. *Biogeosciences*, *12*(5), 1339–1356.

Jorry, S., Jouet, G., Edinger, E. N., Toucanne, S., Counts, J. W., Miramontes, E., Courgeon, S. F., Vazquez Riveiros, N., Le Roy, P., & Camoin, G. (2020). From platform top to adjacent deep sea: New source-to-sink insights into carbonate sediment production and transfer in the SW Indian Ocean 2 (Glorieuses archipelago). *Marine Geology*, *423*, 106144.

Kastens, K., Mascle, J., Auroux, C., et al. (1987). 107: College Station, TX (Ocean Drilling Program). *Proc. Init. Repts. ODP 107*.

Kerr, J., Rickaby, R., Yu, J., Elderfield, H., & Sadekov, A. Y. (2017). The effect of ocean alkalinity and carbon transfer on deep-sea carbonate ion concentration during the past five glacial cycles. *Earth and Planetary Science Letters*, *471*, 42–53.

Kleypas, J. A. (1997). Modeled estimates of global reef habitat and carbonate production since the Last Glacial Maximum. *Paleoceanography*, *12*(4), 533–545.

Kleypas, J. A., Anthony, K. R. N., & Gattuso, J.-P. (2011). Coral reefs modify their seawater carbon chemistry – case study from a barrier reef (Moorea, French Polynesia). *Global Change Biology*, *17*(12), 3667–3678.

Kohfeld, K. E., & Ridgwell, A. (2009). Glacial-interglacial variability in atmospheric CO2. In C. Le Quéré & E. S. Saltzman (Eds.), *Geophysical Monograph Series* (pp. 251–286, Vol. 187). American Geophysical Union.

Krabbenhöft, A., Eisenhauer, A., Böhm, F., Vollstädt, H., Fietzke, J., Liebetrau, V., Augustin, N., Peucker-Ehrenbrink, B., Müller, M. N., Horn, C., Hansen, B. T., Nolte, N., & Wallmann, K. (2010). Constraining the marine strontium budget with natural strontium isotope fractionations (87Sr/86Sr, 88/86Sr) of carbonates, hydrothermal solutions and river waters. *Geochimica et Cosmochimica Acta*, *74*(14), 4097–4109.

Krabbenhöft, A., Fietzke, J., Eisenhauer, A., Liebetrau, V., Böhm, F., & Vollstädt, H. (2009). Determination of radiogenic and stable strontium isotope ratios ((87)Sr/(86)Sr; delta(88/86)Sr) by thermal ionization mass spectrometry applying an (87)Sr/(84)Sr double spike. *Journal of Analytical Atomic Spectrometry*, *24*(9), 1267–1271.

Laugié, M., Michel, J., Pohl, A., Poli, E., & Borgomano, J. (2019). Global distribution of modern shallow-water marine carbonate factories: A spatial model based on environmental parameters. *Scientific Reports*, *9*(1), 16432.

Lear, C. H., Elderfield, H., & Wilson, P. A. (2003). A Cenozoic seawater Sr/Ca record from benthic foraminiferal calcite and its application in determining global weathering fluxes. *Earth and Planetary Science Letters*, *208*(1), 69–84.

Lebrato, M., Garbe-Schönberg, D., Müller, M. N., Blanco-Ameijeiras, S., Feely, R. A., Lorenzoni, L., Molinero, J.-C., Bremer, K., Jones, D. O. B., Iglesias-Rodriguez, D., Greeley, D., Lamare, M. D., Paulmier, A., Graco, M., Cartes, J., Ramos, J. B. e., Lara, A. d., Sanchez-Leal, R., Jimenez, P., … Oschlies, A. (2020). Global variability in seawater Mg:Ca and Sr:Ca ratios in the modern ocean. *Proceedings of the National Academy of Sciences*, *117*(36), 22281–22292.

Lebrato, M., Iglesias-Rodríguez, D., Feely, R. A., Greeley, D., Jones, D. O. B., Suarez-Bosche, N., Lampitt, R. S., Cartes, J. E., Green, D. R. H., & Alker, B. (2010). Global contribution of echinoderms to the marine carbon cycle: CaCO 3 budget and benthic compartments. *Ecological Monographs*, *80*(3), 441–467.

Lindberg, B., & Mienert, J. (2005). Postglacial carbonate production by cold-water corals on the Norwegian Shelf and their role in the global carbonate budget. *Geology*, *33*(7), 537–540.

Lisiecki, L. E., & Raymo, M. E. (2005). A Pliocene-Pleistocene stack of 57 globally distributed benthic 18O records. *Paleoceanography*, *20*(1).

Lough, J. M. (2008). Coral calcification from skeletal records revisited. *Marine Ecology Progress Series*, *373*, 257–264.

Lyle, M. (2003). Neogene carbonate burial in the Pacific Ocean. *Paleoceanography*, *18*(3), 1059.

Lyle, M., Barron, J., Bralower, T. J., Huber, M., Lyle, A. O., Ravelo, A. C., Rea, D. K., & Wilson, P. A. (2008). Pacific Ocean and Cenozoic evolution of climate. *Reviews of Geophysics*, *46*, RG2002.

Lyle, M., Drury, A. J., Tian, J., Wilkens, R., & Westerhold, T. (2019). Late Miocene to Holocene high-resolution eastern equatorial Pacific carbonate records: Stratigraphy linked by dissolution and paleoproductivity. *Climate of the Past*, *15*(5), 1715–1739.

Lyle, M., Olivarez, A., Backman, J., & Tripati, A. (2005). Biogenic Sedimentation in the Eocene Equatorial Pacific-The Stuttering Greenhouse and Eocene Carbonate Compensation Depth. *Ocean Drill. Prog. Sci. Results*, *199*.

Martin, P. A., Lea, D. W., Mashiotta, T. A., Papenfuss, T., & Sarnthein, M. (1999). Variation of foraminiferal Sr/Ca over Quaternary glacial-interglacial cycles: Evidence for changes in mean ocean Sr/Ca? *Geochemistry Geophysics Geosystems*, *1*, 1004.

Martinson, D. G., Pisias, N. G., Hays, J. D., Imbrie, J., Moore, T. C., & Shackleton, N. J. (1987). Age dating and the orbital theory of the ice ages: Development of a high-resolution 0 to 300,000-year chronostratigraphy. *Quaternary Research*, *27*(1), 1–29.

Mazarrasa, I., Marbà, N., Lovelock, C. E., Serrano, O., Lavery, P. S., Fourqurean, J. W., Kennedy, H., Mateo, M. A., Krause-Jensen, D., Steven, A. D. L., & Duarte, C. M. (2015). Seagrass meadows as a globally significant carbonate reservoir. *Biogeosciences*, *12*(16), 4993–5003.

McArthur, J. M., Howarth, R. J., & Shields, G. A. (2012). *Strontium Isotope Stratigraphy* (F. M. Gradstein, J. G. Ogg, M. D. Schmitz, & G. M. Ogg, Eds.). Elsevier Science Bv.

McArthur, J. M., & Howarth, R. (2020, October). LOESS 6 : Look-up table for converting marine-87Sr/86Sr to numerical age and vice versa. The main table accompanying Chapter 7 (Sr-isotope stratigraphy) of 'The Geologic Time Scale 2020'.

McGee, D., Marcantonio, F., McManus, J. F., & Winckler, G. (2010). The response of excess 230Th and extraterrestrial 3He to sediment redistribution at the Blake Ridge, western North Atlantic. *Earth and Planetary Science Letters*, *299*(1-2), 138–149.

McNeil, M. A., Nothdurft, L. D., Dyriw, N. J., Webster, J. M., & Beaman, R. J. (2020). Morphotype differentiation in the Great Barrier Reef Halimeda bioherm carbonate factory: Internal architecture and surface geomorphometrics. *The Depositional Record*, *00*, 1–24.

McNeil, M. A., Webster, J. M., Beaman, R. J., & Graham, T. L. (2016). New constraints on the spatial distribution and morphology of the Halimeda bioherms of the Great Barrier Reef, Australia. *Coral Reefs*, *35*(4), 1343–1355.

Merico, A., Tyrrell, T., & Wilson, P. A. (2008). Eocene/Oligocene ocean de-acidification linked to Antarctic glaciation by sea-level fall. *Nature*, *452*(7190), 979–982.

Miller, K. G., Browning, J. V., Schmelz, W. J., Kopp, R. E., Mountain, G. S., & Wright, J. D. (2020). Cenozoic sea-level and cryospheric evolution from deep-sea geochemical and continental margin records. *Science Advances*, *6*(20).

Milliman, J. D., & Droxler, A. W. (1996). Neritic and pelagic carbonate sedimentation in the marine environment: Ignorance is not bliss. *Geologische Rundschau*, *85*(3), 496–504.

Milliman, J. D. (1993). Production and accumulation of calcium carbonate in the ocean: Budget of a nonsteady state. *Global Biogeochemical Cycles*, *7*(4), 927–957.

Misra, S., & Froelich, P. N. (2012). Lithium isotope history of Cenozoic seawater: Changes in silicate weathering and reverse weathering. *Science (New York, N.Y.)*, *335*(6070), 818–823.

Mokadem, F., Parkinson, I. J., Hathorne, E. C., Anand, P., Allen, J. T., & Burton, K. W. (2015). High-precision radiogenic strontium isotope measurements of the modern and glacial ocean: Limits on glacial-interglacial variations in continental weathering. *Earth and Planetary Science Letters*, *415*, 111–120.

Montaggioni, L. F. (2005). History of Indo-Pacific coral reef systems since the last glaciation: Development patterns and controlling factors. *Earth-Science Reviews*, *71*(1), 1–75.

Montaggioni, L. F., Cabioch, G., Thouveny, N., Frank, N., Sato, T., & Sémah, A.-M. (2011). Revisiting the Quaternary development history of the western New Caledonian shelf system: From ramp to barrier reef. *Marine Geology*, *280*(1), 57–75.

Mörth, C.-M., & Backman, J. (2011). Practical steps for improved estimates of calcium carbonate concentrations in deep sea sediments using coulometry. *Limnology and Oceanography: Methods*, *9*(12), 565–570.

Murray, R. W., Knowlton, C., Leinen, M., Mix, A. C., & Polsky, C. H. (2000). Export production and carbonate dissolution in the central equatorial Pacific Ocean over the past 1 Myr. *Paleoceanography*, *15*(6), 570–592.

O'Mara, N. A., & Dunne, J. P. (2019). Hot Spots of Carbon and Alkalinity Cycling in the Coastal Oceans. *Scientific Reports*, *9*(1), 4434.

Opdyke, B. N., & Walker, J. C. G. (1992). Return of the coral reef hypothesis: Basin to shelf partitioning of CaCO3 and its effect on atmospheric CO2. *Geology*, *20*(8), 733–736.

Opdyke, B. N., & Wilkinson, B. H. (1988). Surface area control of shallow cratonic to deep marine carbonate accumulation. *Paleoceanography*, *3*(6), 685–703.

Pälike, H., Lyle, M., Nishi, H., Raffi, I., Ridgwell, A., Gamage, K., Klaus, A., Acton, G., Anderson, L., Backman, J., Baldauf, J., Beltran, C., Bohaty, S., Bown, P., Busch, W., Channell, J., Chun, C., Delaney, M., Dewangan, P., & Zeebe, R. (2012). A Cenozoic record of the equatorial Pacific carbonate compensation depth. *Nature*, *488*, 609–14.

Paytan, A., Kastner, M., Martin, E. E., Macdougall, J. D., & Herbert, T. (1993). Marine barite as a monitor of seawater strontium isotope composition. *Nature*, *366*(6454), 445–449.

Paytan, A., Griffith, E. M., Eisenhauer, A., Hain, M. P., Wallmann, K., & Ridgwell, A. (2021). A 35-million-year record of seawater stable Sr isotopes reveals a fluctuating global carbon cycle. *Science*, *371*(6536), 1346–1350.

Pearce, C. R., Parkinson, I. J., Gaillardet, J., Charlier, B. L. A., Mokadem, F., & Burton, K. W. (2015). Reassessing the stable (delta Sr-88/86) and radiogenic (Sr-87/Sr-86) strontium isotopic composition of marine inputs. *Geochimica Et Cosmochimica Acta*, *157*, 125–146.

Perry, C. T., Morgan, K. M., & Yarlett, R. T. (2017). Reef Habitat Type and Spatial Extent as Interacting Controls on Platform-Scale Carbonate Budgets. *Frontiers in Marine Science*, *4*(185).

Perry, C. T., Salter, M. A., Morgan, K. M., & Harborne, A. R. (2019). Census Estimates of Algal and Epiphytic Carbonate Production Highlight Tropical Seagrass Meadows as Sediment Production Hotspots. *Frontiers in Marine Science*, *6*(120).

Pico, T., Creveling, J. R., & Mitrovica, J. X. (2017). Sea-level records from the U.S. mid-Atlantic constrain Laurentide Ice Sheet extent during Marine Isotope Stage 3. *Nature Communications*, *8*, 15612.

Pisias, N. G., & Mix, A. C. (1997). Spatial and temporal oceanographic variability of the eastern equatorial Pacific during the Late Pleistocene: Evidence from radiolaria microfossils. *Paleoceanography*, *12*(3), 381–393.

Pomar, L., & Hallock, P. (2008). Carbonate factories: A conundrum in sedimentary geology. *Earth-Science Reviews*, *87*(3-4), 134–169.

Pomar, L., Baceta, J. I., Hallock, P., Mateu-Vicens, G., & Basso, D. (2017). Reef building and carbonate production modes in the west-central Tethys during the Cenozoic. *Marine and Petroleum Geology*, *83*, 261–304.

Rao, V. P., Mahale, V. P., & Chakraborty, B. (2018). Bathymetry and sediments on the carbonate platform off western India: Significance of Halimeda bioherms in carbonate sedimentation. *Journal of Earth System Science*, *127*(8), 106.

Ravizza, G., & Peucker-Ehrenbrink, B. (2003). The marine 187Os/188Os record of the Eocene–Oligocene transition: The interplay of weathering and glaciation. *Earth and Planetary Science Letters*, *210*(1), 151–165.

Rea, D. K., & Lyle, M. W. (2005). Paleogene calcite compensation depth in the eastern subtropical Pacific: Answers and questions. *Paleoceanography*, *20*(1).

Rees, S. A., Opdyke, B. N., Wilson, P. A., & Henstock, T. J. (2006). Significance of Halimeda bioherms to the global carbonate budget based on a geological sediment budget for the Northern Great Barrier Reef, Australia. *Coral Reefs*, *26*(1), 177–188.

Richter, F. M., & DePaolo, D. J. (1987). Numerical models for diagenesis and the Neogene Sr isotopic evolution of seawater from DSDP Site 590B. *Earth and Planetary Science Letters*, *83*(1), 27–38.

Richter, F. M., & DePaolo, D. J. (1988). Diagenesis and Sr isotopic evolution of seawater using data from DSDP 590B and 575. *Earth and Planetary Science Letters*, *90*(4), 382–394.

Rickaby, R. E. M., Elderfield, H., Roberts, N., Hillenbrand, C.-D., & Mackensen, A. (2010). Evidence for elevated alkalinity in the glacial Southern Ocean. *Paleoceanography*, *25*, PA1209.

Ridgwell, A., Watson, A. J., Maslin, M. A., & Kaplan, J. O. (2003). Implications of coral reef buildup for the controls on atmospheric CO2 since the Last Glacial Maximum. *Paleoceanography*, *18*(4), 1083.

Ridgwell, A., & Zeebe, R. E. (2005). The role of the global carbonate cycle in the regulation and evolution of the Earth system. *Earth and Planetary Science Letters*, *234*(3), 299–315.

Riechelmann, S., Mavromatis, V., Buhl, D., Dietzel, M., Eisenhauer, A., & Immenhauser, A. (2016). Impact of diagenetic alteration on brachiopod shell magnesium isotope (26Mg) signatures: Experimental versus field data. *Chemical Geology*, *440*, 191–206.

Ryan, D. A., Opdyke, B. N., & Jell, J. S. (2001). Holocene sediments of Wistari Reef: Towards a global quantification of coral reef related neritic sedimentation in the Holocene. *Palaeogeography, Palaeoclimatology, Palaeoecology*, *175*(1), 173–184.

Sandberg, P. A. (1983). An oscillating trend in Phanerozoic non-skeletal carbonate mineralogy. *Nature*, *305*(5929), 19–22.

Scheibner, C., & Speijer, R. P. (2007). Decline of coral reefs during late Paleocene to early Eocene global warming. *eEarth Discussions*, *2*(3), 133–150.

Schlager, W., Reijmer, J. J. G., & Droxler, A. (1994). Highstand shedding of carbonate platforms. *Journal of Sedimentary Research*, *64*(3b), 270–281.

Schlanger, S. O. (1988). Strontium Storage and Release During Deposition and Diagenesis of Marine Carbonates Related to Sea-Level Variations. In A. Lerman & M. Meybeck (Eds.), *Physical and Chemical Weathering in Geochemical Cycles* (pp. 323–339). Springer Netherlands.

Sigman, D. M., & Boyle, E. A. (2000). Glacial/interglacial variations in atmospheric carbon dioxide. *Nature*, *407*(6806), 859–869.

Silverman, J., Lazar, B., Cao, L., Caldeira, K., & Erez, J. (2009). Coral reefs may start dissolving when atmospheric CO2 doubles. *Geophysical Research Letters*, *36*, L05606.

Silverman, J., Lazar, B., & Erez, J. (2007). Effect of aragonite saturation, temperature, and nutrients on the community calcification rate of a coral reef. *Journal of Geophysical Research: Oceans*, *112*, C05004.

Smith, S., & Mackenzie, F. (2016). The Role of CaCO3 Reactions in the Contemporary Oceanic CO2 Cycle. *Aquatic Geochemistry*, *22*, 153–175.

Sosdian, S. M., Lear, C. H., Tao, K., Grossman, E. L., O'Dea, A., & Rosenthal, Y. (2012). Cenozoic seawater Sr/Ca evolution. *Geochemistry, Geophysics, Geosystems*, *13*(10), Q10014.

Spratt, R. M., & Lisiecki, L. E. (2016). A Late Pleistocene sea level stack. *Climate of the Past*, *12*(4), 1079–1092.

Stanley, S. M. (2005). *Earth System History*. Macmillan.

Stanley, S. M. (2006). Influence of seawater chemistry on biomineralization throughout phanerozoic time: Paleontological and experimental evidence. *Palaeogeography, Palaeoclimatology, Palaeoecology*, *232*(2), 214–236.

Stanley, S. M., & Hardie, L. A. (1998). Secular oscillations in the carbonate mineralogy of reef-building and sediment-producing organisms driven by tectonically forced shifts in seawater chemistry. *Palaeogeography, Palaeoclimatology, Palaeoecology*, *144*(1), 3–19.

Steuber, T., & Veizer, J. (2002). Phanerozoic record of plate tectonic control of seawater chemistry and carbonate sedimentation. *Geology*, *30*, 1123–1126.

Stevenson, E. I., Hermoso, M., Rickaby, R. E. M., Tyler, J. J., Minoletti, F., Parkinson, I. J., Mokadem, F., & Burton, K. W. (2014). Controls on stable strontium isotope fractionation in coccolithophores with implications for the marine Sr cycle. *Geochimica Et Cosmochimica Acta*, *128*, 225–235.

Stoll, H. M., & Schrag, D. P. (1998). Effects of Quaternary Sea Level Cycles on Strontium in Seawater. *Geochimica et Cosmochimica Acta*, *62*(7), 1107–1118.

Stoll, H. M., Schrag, D. P., & Clemens, S. C. (1999). Are seawater Sr/Ca variations preserved in quaternary foraminifera? *Geochimica et Cosmochimica Acta*, *63*(21), 3535–3547.

Sulpis, O., Agrawal, P., Wolthers, M., Munhoven, G., Walker, M., & Middelburg, J. J. (2022). Aragonite dissolution protects calcite at the seafloor. *Nature Communications*, *13*(1), 1104.

Sulpis, O., Jeansson, E., Dinauer, A., Lauvset, S. K., & Middelburg, J. J. (2021). Calcium carbonate dissolution patterns in the ocean. *Nature Geoscience*, *14*(6), 423–428.

Sundquist, E. T., & Visser, K. (2003, January). 8.09 - The Geologic History of the Carbon Cycle. In H. D. Holland & K. K. Turekian (Eds.), *Treatise on Geochemistry* (pp. 425–472). Pergamon.

Swart, P. K. (2008). Global synchronous changes in the carbon isotopic composition of carbonate sediments unrelated to changes in the global carbon cycle. *Proceedings of the National Academy of Sciences*, *105*(37), 13741–13745.

Swart, P. K., & Eberli, G. (2005). The nature of the 13C of periplatform sediments: Implications for stratigraphy and the global carbon cycle. *Sedimentary Geology*, *175*(1-4), 115–129.

Taylor, V. E., Westerhold, T., Bohaty, S. M., Backman, J., Dunkley Jones, T., Edgar, K. M., Egan, K. E., Lyle, M., Pälike, H., Röhl, U., Zachos, J., & Wilson, P. A. (2023). Transient Shoaling, Over-Deepening and Settling of the Calcite Compensation Depth at the Eocene-Oligocene Transition. *Paleoceanography and Paleoclimatology*, *38*(6), e2022PA004493.

Titschack, J., Baum, D., De Pol-Holz, R., Lopez Correa, M., Forster, N., Floegel, S., Hebbeln, D., & Freiwald, A. (2015). Aggradation and carbonate accumulation of Holocene Norwegian cold-water coral reefs. *Sedimentology*, *62*(7), 1873–1898.

Titschack, J., Fink, H. G., Baum, D., Wienberg, C., Hebbeln, D., & Freiwald, A. (2016). Mediterranean cold-water corals - an important regional carbonate factory? *Depositional Record*, *2*(1), 74–96.

Tosquella, J., Martín-Martín, M., Guerrera, F., Serrano, F., & Tramontana, M. (2022). The Eocene carbonate platform of the central-western Malaguides (Internal Betic Zone, S Spain) and its meaning for the Cenozoic paleogeography of the westermost Tethys. *Palaeogeography, Palaeoclimatology, Palaeoecology*, *589*, 110840.

Tripati, A. K., Allmon, W. D., & Sampson, D. E. (2009). Possible evidence for a large decrease in seawater strontium/calcium ratios and strontium concentrations during the Cenozoic. *Earth and Planetary Science Letters*, *282*(1), 122–130.

Turchyn, A. V., & DePaolo, D. J. (2011). Calcium isotope evidence for suppression of carbonate dissolution in carbonate-bearing organic-rich sediments. *Geochimica et Cosmochimica Acta*, *75*(22), 7081–7098.

Utami, D. A., Reuning, L., & Cahyarini, S. Y. (2018). Satellite- and field-based facies mapping of isolated carbonate platforms from the Kepulauan Seribu Complex, Indonesia. *The Depositional Record*, *4*(2), 255–273.

Van Andel, T. H. (1975). Mesozoic/Cenozoic calcite compensation depth and the global distribution of calcareous sediments. *Earth and Planetary Science Letters*, *26*, 187–194.

Van Andel, T. H., Ross Heath, G., & Moore, T. C. (1975). Cenozoic history and paleoceanography of the central equatorial Pacific Ocean: A regional synthesis of Deep Sea Drilling Project data. Boulder, Colo: Geological Society of America.

van der Ploeg, R., Boudreau, B. P., Middelburg, J. J., & Sluijs, A. (2019). Cenozoic carbonate burial along continental margins. *Geology*, *47*(11), 1025–1028.

Vance, D., Teagle, D. A. H., & Foster, G. L. (2009). Variable Quaternary chemical weathering fluxes and imbalances in marine geochemical budgets. *Nature*, *458*(7237), 493–496.

Vanden Berg, M. D., & Jarrard, R. D. (2002). Determination of Equatorial Pacific mineralogy using light absorption spectroscopy. In *Lyle, M., Wilson, P.A., Janecek, T.R., et al., 2002 Proceedings of the Ocean Drilling Program, Initial Reports Volume 199*.

Vanden Berg, M. D., & Jarrard, R. D. (2004). Cenozoic mass accumulation rates in the equatorial Pacific based on high-resolution mineralogy of Ocean Drilling Program Leg 199. *Paleoceanography*, *19*, A2021.

Vanden Berg, M. D., & Jarrard, R. D. (2006). Data report: High-resolution mineralogy for Leg 199 based on reflectance spectroscopy and physical properties. *In Wilson, P.A., Lyle, M., and Firth, J.V. (Eds.), Proc. ODP, Sci. Results,199: College Station, TX (Ocean Drilling Program)*, 1–23.

Vecsei, A. (2004a). A new estimate of global reefal carbonate production including the fore-reefs. *Global and Planetary Change*, *43*(1), 1–18.

Vecsei, A. (2004b). Carbonate production on isolated banks since 20 k.a. BP: Climatic implications. *Palaeogeography Palaeoclimatology Palaeoecology*, *214*(1-2), 3–10.

Vecsei, A., & Berger, W. H. (2004). Increase of atmospheric CO2 during deglaciation: Constraints on the coral reef hypothesis from patterns of deposition. *Global Biogeochemical Cycles*, *18*, GB1035.

Veizer, J. (1989). Strontium Isotopes in Seawater through Time. *Annual Review of Earth and Planetary Sciences*, *17*(1), 141–167.

Voigt, J., Hathorne, E. C., Frank, M., Vollstaedt, H., & Eisenhauer, A. (2015). Variability of carbonate diagenesis in equatorial Pacific sediments deduced from radiogenic and stable Sr isotopes. *Geochimica et Cosmochimica Acta*, *148*, 360–377.

Vollstädt, H., Eisenhauer, A., Wallmann, K., Böhm, F., Fietzke, J., Liebetrau, V., Krabbenhoeft, A., Farkas, J., Tomasovych, A., Raddatz, J., & Veizer, J. (2014). The Phanerozoic delta Sr-88/86 record of seawater: New constraints on past changes in oceanic carbonate fluxes. *Geochimica Et Cosmochimica Acta*, *128*, 249–265.

Walker, J. C. G., & Opdyke, B. C. (1995). Influence of variable rates of neritic carbonate deposition on atmospheric carbon dioxide and pelagic sediments. *Paleoceanography*, *10*(3), 415–427.

Wallmann, K., & Aloisi, G. (2012). The Global Carbon Cycle: Geological Processes. In *Fundamentals of Geobiology* (pp. 20–35). John Wiley & Sons, Ltd.

Wang, J., Tarhan, L. G., Jacobson, A. D., Oehlert, A. M., & Planavsky, N. J. (2023). The evolution of the marine carbonate factory. *Nature*.

Webster, J. M., Braga, J. C., Humblet, M., Potts, D. C., Iryu, Y., Yokoyama, Y., Fujita, K., Bourillot, R., Esat, T. M., Fallon, S., Thompson, W. G., Thomas, A. L., Kan, H., McGregor, H. V., Hinestrosa, G., Obrochta, S. P., & Lougheed, B. C. (2018). Response of the Great Barrier Reef to sea-level and environmental changes over the past 30,000 years. *Nature Geoscience*, *11*(6), 426–432.

Westerhold, T., Röhl, U., Pälike, H., Wilkens, R., Wilson, P. A., & Acton, G. (2014). Orbitally tuned timescale and astronomical forcing in the middle Eocene to early Oligocene. *Climate of the Past*, *10*(3), 955–973.

Widanagamage, I. H., Schauble, E. A., Scher, H. D., & Griffith, E. M. (2014). Stable strontium isotope fractionation in synthetic barite. *Geochimica et Cosmochimica Acta*, *147*, 58–75.

Winckler, G., Anderson, R. F., Fleisher, M. Q., McGee, D., & Mahowald, N. (2008). Covariant Glacial-Interglacial Dust Fluxes in the Equatorial Pacific and Antarctica. *Science*, *320*(5872), 93–96.

Wood, M., Hayes, C. T., & Paytan, A. (2023). Global Quaternary Carbonate Burial: Proxy- and Model-Based Reconstructions and Persisting Uncertainties. *Annual Review of Marine Science*, *15*(1), 277–302.

Wood, S. N. (2011). Fast stable restricted maximum likelihood and marginal likelihood estimation of semiparametric generalized linear models. *Journal of the Royal Statistical Society: Series B (Statistical Methodology)*, *73*(1), 3–36.

Yao, W., Markovic, S., Paytan, A., Erhardt, A. M., & Wortmann, U. G. (2021). Quantifying pyrite oxidation on continental shelves during the onset of Antarctic glaciation in the Eocene-Oligocene transition. *Earth and Planetary Science Letters*, *568*, 117015.

Yokoyama, Y., Esat, T. M., Thompson, W. G., Thomas, A. L., Webster, J. M., Miyairi, Y., Sawada, C., Aze, T., Matsuzaki, H., Okuno, J., Fallon, S., Braga, J.-C., Humblet, M., Iryu, Y., Potts, D. C., Fujita, K., Suzuki, A., & Kan, H. (2018). Rapid glaciation and a two-step sea level plunge into the Last Glacial Maximum. *Nature*, *559*(7715), 603–607.

Yu, J., Menviel, L., Jin, Z. D., Anderson, R. F., Jian, Z., Piotrowski, A. M., Ma, X., Rohling, E. J., Zhang, F., Marino, G., & McManus, J. F. (2020). Last glacial atmospheric CO2 decline due to widespread Pacific deep-water expansion. *Nature Geoscience*, *13*(9), 628–633.

Yu, J., Anderson, R., & Rohling, E. (2014). Deep Ocean Carbonate Chemistry and Glacial-Interglacial Atmospheric CO2 Change. *Oceanography*, *27*(1), 16–25.

Yu, J., Elderfield, H., Jin, Z., Tomascak, P., & Rohling, E. J. (2014). Controls on Sr/Ca in benthic foraminifera and implications for seawater Sr/Ca during the late Pleistocene. *Quaternary Science Reviews*, *98*, 1–6.

Zachos, J. C., Opdyke, B. N., Quinn, T. M., Jones, C. E., & Halliday, A. N. (1999). Early Cenozoic glaciation, Antarctic weathering, and seawater 87Sr/86Sr: Is there a link? *Chemical Geology*, *161*, 165–180.

Zeebe, R. E. (2012). History of Seawater Carbonate Chemistry, Atmospheric CO2, and Ocean Acidification. *Annual Review of Earth and Planetary Sciences*, *40*(1), 141–165.

Zeebe, R. E., & Marchitto, T. M. (2010). Atmosphere and ocean chemistry. *Nature Geoscience*, *3*(6), 386–387.

Zeebe, R. E., & Westbroek, P. (2003). A simple model for the CaCO3 saturation state of the ocean: The "Strangelove," the "Neritan," and the "Cretan" Ocean. *Geochemistry, Geophysics, Geosystems*, *4*(12), 1104.

Zhang, S., Zhou, R., & DePaolo, D. J. (2020). The seawater Sr/Ca ratio in the past 50 Myr from bulk carbonate sediments corrected for diagenesis. *Earth and Planetary Science Letters*, *530*, 115949.